

## Anelasticity in Al-alloy thin films : an experimental analysis

**Citation for published version (APA):**

Bergers, L. I. J. C. (2013). *Anelasticity in Al-alloy thin films : an experimental analysis*. [Phd Thesis 1 (Research TU/e / Graduation TU/e), Mechanical Engineering]. Technische Universiteit Eindhoven.  
<https://doi.org/10.6100/IR761377>

**DOI:**

[10.6100/IR761377](https://doi.org/10.6100/IR761377)

**Document status and date:**

Published: 01/01/2013

**Document Version:**

Publisher's PDF, also known as Version of Record (includes final page, issue and volume numbers)

**Please check the document version of this publication:**

- A submitted manuscript is the version of the article upon submission and before peer-review. There can be important differences between the submitted version and the official published version of record. People interested in the research are advised to contact the author for the final version of the publication, or visit the DOI to the publisher's website.
- The final author version and the galley proof are versions of the publication after peer review.
- The final published version features the final layout of the paper including the volume, issue and page numbers.

[Link to publication](#)

**General rights**

Copyright and moral rights for the publications made accessible in the public portal are retained by the authors and/or other copyright owners and it is a condition of accessing publications that users recognise and abide by the legal requirements associated with these rights.

- Users may download and print one copy of any publication from the public portal for the purpose of private study or research.
- You may not further distribute the material or use it for any profit-making activity or commercial gain
- You may freely distribute the URL identifying the publication in the public portal.

If the publication is distributed under the terms of Article 25fa of the Dutch Copyright Act, indicated by the "Taverne" license above, please follow below link for the End User Agreement:

[www.tue.nl/taverne](http://www.tue.nl/taverne)

**Take down policy**

If you believe that this document breaches copyright please contact us at:

[openaccess@tue.nl](mailto:openaccess@tue.nl)

providing details and we will investigate your claim.

# **Anelasticity in Al-alloy thin films: an experimental analysis**

Lambert Bergers

Anelasticity in Al-alloy thin films: an experimental analysis/ by Lambert Bergers  
Technische Universiteit Eindhoven, 2013

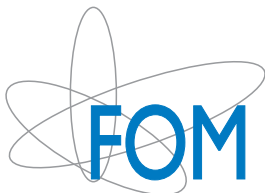
A catalogue record is available from the Eindhoven University of Technology Library ISBN: 978-90-386-3508-8

Printed by: Proefschriftmaken.nl — — Uitgeverij BOXPress

Cover design: L.I.J.C. Bergers.

The cover is a scanning electron micrograph of the surface of an aluminum-copper microelectromechanical system, revealing  $\text{Al}_2\text{Cu}$  precipitates (bright spots) and grain boundaries (dark grooves).

This research was carried out under Project number M62.2.08SDMP12 in the framework of the Industrial Partnership Program on Size Dependent Material Properties of the Materials innovation institute M2i (<http://www.m2i.nl>) and the Foundation of Fundamental Research on Matter (FOM), which is part of the Netherlands Organization for Scientific Research (NWO).



# Anelasticity in Al-alloy thin films: an experimental analysis

PROEFSCHRIFT

ter verkrijging van de graad van doctor aan de  
Technische Universiteit Eindhoven, op gezag van  
de rector magnificus, prof.dr.ir. C.J. van Duijn,  
voor een commissie aangewezen door het College  
van Promoties, in het openbaar te verdedigen op  
donderdag 12 december 2013 om 14.00 uur

door

Lambertus Idris Johannes Catharina Bergers

geboren te Tilburg

Dit proefschrift is goedgekeurd door de promotoren en de samenstelling van de promotiecommissie is als volgt:

voorzitter: prof.dr. L.P.H. de Goey  
promoter: prof.dr.ir. M.G.D. Geers  
copromotor: dr.ir. J.P.M. Hoefnagels  
leden: prof.dr.rer.nat. G. Dehm (Ruhr Universität Bochum)  
prof.dr. J.Th.M. De Hosson (Rijksuniversiteit Groningen)  
prof.dr. T. Pardoën (Université Catholique de Louvain)  
prof.dr.ir. J.M.J. den Toonder  
adviseur: dr.ir. M.A.J. van Gils (EPCOS Netherlands bv.)

# Contents

---

<b>1</b>	<b>Introduction</b>	<b>1</b>
1.1	Motivation . . . . .	1
1.2	Goal and strategy . . . . .	3
1.3	Thesis outline . . . . .	4
<b>2</b>	<b>Measuring time-dependent deformations in metallic MEMS</b>	<b>5</b>
2.1	Introduction. . . . .	6
2.2	Design of experiment . . . . .	6
2.3	Experimental implementation . . . . .	10
2.4	Results and discussion . . . . .	12
2.5	Conclusion . . . . .	16
<b>3</b>	<b>Characterizing time-dependent anelastic microbeam bending mechanics</b>	<b>17</b>
3.1	Introduction. . . . .	18
3.2	Strategy . . . . .	19
3.3	Curvature measurement . . . . .	20
3.4	Mechanical characterization. . . . .	26
3.5	Conclusion . . . . .	31
<b>4</b>	<b>On-wafer time-dependent nano-tensile testing</b>	<b>33</b>
4.1	Introduction. . . . .	34
4.2	Design principle . . . . .	35
4.3	Specimen design and fabrication . . . . .	37
4.4	Nano-tensile stage: design and realization . . . . .	40
4.5	Proof of principle measurements . . . . .	52
4.6	Conclusion . . . . .	53
<b>5</b>	<b>Some observations on <math>\theta</math> precipitation in Al-(1wt%)Cu thin films</b>	<b>55</b>
5.1	Introduction. . . . .	56
5.2	Characterization of as-received Al-(1wt%)Cu . . . . .	57
5.3	Controlling the precipitate microstructure . . . . .	61
5.4	The hardness decrease revisited . . . . .	70
5.5	Conclusions . . . . .	70

<b>6</b>	<b>On the underlying micromechanisms in time-dependent anelasticity in Al-(1wt%)Cu thin films</b>	<b>73</b>
6.1	Introduction . . . . .	74
6.2	Experimental characterization . . . . .	76
6.3	Time dependent anelasticity in microbeam bending . . . . .	79
6.4	Time dependent anelasticity in nano-tensile testing . . . . .	82
6.5	Possible mechanisms . . . . .	85
6.6	Conclusions . . . . .	89
<b>7</b>	<b>Conclusions and recommendations</b>	<b>91</b>
7.1	Methodologies for on-wafer characterization of time-dependent anelasticity . . . . .	91
7.2	Insights into the underlying physical micromechanisms . . . . .	92
7.3	Recommendations . . . . .	93
	<b>References</b>	<b>110</b>
<b>A</b>	<b>Enhanced Global Digital Image Correlation for accurate measurement of microbeam bending</b>	<b>111</b>
A.1	Introduction . . . . .	112
A.2	Principle of global digital image correlation and curvature measurement . . . . .	113
A.3	Evaluation of accuracy . . . . .	115
A.4	Results . . . . .	116
A.5	Conclusion . . . . .	119
<b>B</b>	<b>Multi-mode linear time-dependent anelasticity</b>	<b>121</b>
<b>C</b>	<b>Derivation of misalignment criterium</b>	<b>123</b>
<b>D</b>	<b>Load cell calibration</b>	<b>125</b>
	<b>Samenvatting</b>	<b>129</b>
	<b>Acknowledgements</b>	<b>131</b>
	<b>Curriculum vitae</b>	<b>133</b>
	<b>List of publications</b>	<b>134</b>

# Summary

## Anelasticity in Al-alloy thin films: an experimental analysis

---

Micro-electromechanical systems (MEMS) enable novel high-tech applications in, e.g., aerospace, biomedicine and wireless communications by integrating electrical and mechanical functionalities to address increasing demands: higher performance, more functionality, smaller dimensions. Although aluminum alloy thin films are electrically favorable, the compromised mechanical reliability still forms a fundamental challenge. Miniaturization has revealed detrimental size-dependent behavior in time-dependent elasticity, i.e. anelasticity, for free standing Al-alloy thin films. However, systematic experimental analyses of these mechanics have yet to be performed, partly due to the challenges of microscale testing. This thesis work therefore aimed to develop on-wafer mechanical characterization methods and to acquire insights into the underlying physical micro-mechanisms responsible for anelastic size-effects.

Firstly, two methodologies were developed for reproducible characterization of anelasticity of on-wafer test structures in combination with microscopy. The specimens were 5  $\mu\text{m}$ -thick aluminum and Al-(1wt%)Cu films fabricated in a MEMS fabrication process. A microbeam bending methodology and a nano-tensile test methodology were developed. To measure minute strains involved in anelasticity, both methodologies relied on novel improvements and developments to optical imaging and processing techniques: digital holographic microscopy, confocal optical profilometry, bright field optical microscopy, global digital image correlation. This ensured reproducible deformation measurements of  $< 6 \cdot 10^{-6}$  strain during time spans of days. For the nano-tensile testing drift-compensated force measurements achieved resolution down to 70 nN and maximum forces up to 200 mN. The microbeam bending method relied on a multi-mode anelasticity model to yield key characteristics of the mechanical behavior without an explicit force measurement. Hence, the two micromechanical techniques enabled characterization of anelasticity of these thin metal films.

Subsequently, the microstructure of pure aluminum and Al-(1wt%)Cu thin films were characterized to investigate the influences of grain boundaries and alloy microstructure, i.e. so-



lute concentration, precipitate type, size and distribution. The grain boundaries of various microstructures were characterized with electron backscatter diffraction. The influence of precipitates was investigated by altering their state through heat treatments for homogenization and aging. Backscatter electron contrast imaging, energy dispersive spectroscopy, wide angle X-ray diffraction and high resolution transmission electron microscopy revealed the variations of precipitate type and distribution in the Al-Cu alloy microstructure. Interestingly, the precipitation in the thin films was different compared to precipitation in bulk. The precipitation appeared to occur sooner and did not yield  $\theta'$  precipitates. This difference was hypothesized to be due to preferential nucleation of  $\theta$  at the grain boundary grooves and surface, which could result in a lower free energy of the system with respect to bulk precipitation.

Finally, the two mechanical characterization techniques were applied to measure the time-dependent anelastic response as function of the microstructural variations. The influence of grain boundaries and precipitation state was probed with the microbeam bending methodology on the Al-Cu specimens. However, results strongly suggested a negligible influence of either grain boundaries or precipitate size or state. Nano-tensile tests on Al-Cu and pure Al revealed nearly identical anelastic behavior as compared to the Al-Cu microbeams. These observations strongly suggested that the grain boundaries, precipitates and even Cu-solutes did not influence the time-dependent anelasticity. This led to the hypothesis that the underlying micromechanism responsible for time-dependent anelasticity could be related to dislocation junctions and entanglements and their diffusion-limited formation and relaxation.

# Chapter 1

## Introduction

---

### 1.1 Motivation

Micro-electromechanical systems (MEMS) enable novel high-tech applications in, e.g., aerospace, biomedicine, consumer electronics and wireless communications. By integrating electrical and mechanical functionalities at the micrometer to the millimeter length scale they address increasing demands: higher performance, increased energy efficiency and more functionality, all in smaller dimensions. Whereas certain applications have successfully taken up MEMS, such as tire pressure sensors, accelerometers and gyroscopes for personal navigation, the area of telecommunications has yet to exploit the full potential of radio frequency MEMS (RF-MEMS) [124]. Innovations with RF-MEMS, through a.o. electrical switches or variable capacitors, see Fig.1.1a, could improve the power handling and transmission of RF-signals, while reducing the amount of components [153]. This would for example improve smartphone battery lifetime or reduce the amount of dropped calls due to poor signal quality.

However, the mechanical reliability still forms a fundamental challenge [78, 170, 173, 181, 185]. At first sight, aluminum-copper (Al-Cu) alloy thin films combine favorable electrical, mechanical and processing characteristics compared to other thin metal films, thus enabling the above mentioned innovations with RF-MEMS [129, 130, 167]. Miniaturization, however, has revealed unwanted long-term deformation behavior, leading to unreliable device operation in these free-standing Al-alloy thin films: time-dependent anelasticity [128, 170, 171]. This deformation is reversible, though not instantaneously, which is more common for polymer materials, such as memory foam, see Fig.1.1b. For metals, on the other hand, this is rather unusual, in which reversible deformations generally are instantaneous, e.g. coil springs. Time-dependent deformation usually results in relaxation of stress and permanent deformations, e.g. de-tuning of instrument strings. From a fundamental physical point of view, it is remarkable that a metal deforms, apparently permanently, but then in time recovers some, if not all, of that permanent deformation. Hence, technological development and scientific curiosity both drive the pursuit to further understand this

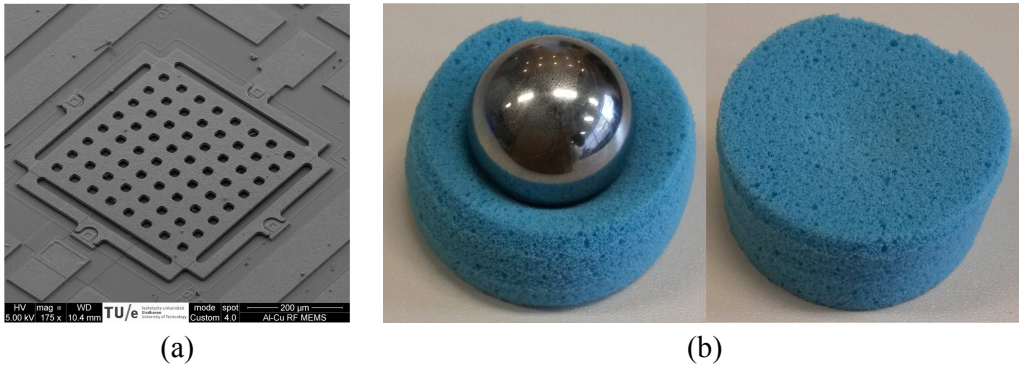


Figure 1.1: (a) A scanning electron microscope image of a radio-frequency microelectromechanical system: a capacitive switch consisting of a perforated square plate suspended at its corners by hinging beams that are fixed to four points on the chip substrate. The plate and beams are made of an aluminum-alloy. It suffers from time-dependent anelasticity, which is commonly known in polymers as visco-elasticity as demonstrated by polymer foams, known as memory foam, (b) that recover their shape slowly after being deformed.

time-dependent anelasticity.

There are some ideas about the origin of this anelastic behavior. It has been well established that miniaturization of components can trigger size-effects in the mechanical response [2, 39]: an interplay appears between microstructural length scales, such as grain size, and specimen structural length scales, such as the ratio of free-surface to material volume. However, whereas size-effects in the elastic response, plastic yield, strength and cyclic fatigue of thin films have received considerable attention [2, 33, 38, 67, 155, 189], how such size-effects could influence the observed time-dependent anelasticity is not well understood [33]. Only a few studies have some relation to size-effects in time-dependent metallic thin film mechanics: nano-indentation size-effects in creep of pure bulk Al [112], thickness effects through grain orientation of Al-alloy foils [190], and grain size, shape and thickness effects on diffusion creep [70, 85]. Other work that does not deal with size-effects, but does deal with time-dependent anelasticity in thin aluminum films, suggests that grain boundary effects play a dominant role [4, 29, 88, 91, 108, 109, 179]. Related work on creep at elevated temperatures in Al thin films indicate that the grain size only affects the behavior [19], while in Al-alloys precipitates [128–130] and dislocation structures [191] explain the time-dependent behavior. With these different possible mechanisms and explanations, a systematic study of size-effects in time-dependent anelasticity in Al-Cu films would greatly aid the understanding of this behavior.

The current shortcoming in understanding time-dependent anelasticity is partly due to the difficulties of experimentally investigating these effects. These difficulties are the handling of specimens smaller than the diameter of a hair, measuring the deformations that result in displacements of a fraction of this diameter, and measuring minute forces that are a fraction of the lift force generated by a fruit fly [187]. The past two decades have provided many different methods for micromechanical characterization of materials, see reviews in [63, 77, 81, 103, 145, 160, 163]. However, the case of time-dependent mechanical characterization additionally poses stringent requirements on the measurement stability and reproducibility.

Mechanical, thermal and electronic drift in measurement setup and instrumentation need to be dealt with to ascertain that the material behavior is measured and not the behavior of the setup or an environmental effect. Furthermore, the fabrication has a significant influence on the final microstructure, which makes it highly preferable to perform these investigations on specimens that are fabricated in the same manner as the actual MEMS. In all, dealing with these challenges requires a thorough in-depth experimental analysis.

## 1.2 Goal and strategy

This research first aims to develop on-wafer mechanical characterization methods suitable for characterizing size-effects in time-dependent anelasticity at the microscale across timescales relevant to MEMS, i.e. from seconds to a day. Second, using these methods this research aims to acquire insights into the underlying physical micro-mechanisms responsible for the time-dependent anelasticity at these length scales.

In order to realize a successful on-wafer characterization methodology, the challenges in micromechanical testing need to be addressed.

1. Proper quantification and understanding of the mechanics can only be achieved by precise loading and control of the boundary conditions of the specimens. On the one hand microbeam bending offers relatively easy deflection control, but it is not straightforward to interpret the effects of the highly heterogeneous stress state, i.e. a stress gradient of tension at one surface to compression at the other. On the other hand, uniaxial tension is more straightforward to interpret, but requires great care in controlling the loading to avoid unwanted bending stemming from misalignment of specimen and loading device.
2. Measurement of ultra-small applied loads and resulting deformations with high reproducibility over time scales of seconds to days requires smart techniques to not only distinguish these, but also to exclude background effects like mechanical drift or thermal expansion. Although optical bright field and optical profilometry yield sub- $\mu\text{m}$  resolution, the use of a novel image processing strategy based on global digital image correlation (GDIC) enables the measurement of nm-scale deformations in in-plane and out-of-plane directions, while at the same time accounting for background signals. Furthermore, the reproducible measurement of minute forces requires high-precision instrumentation combined with smart background measurements.

To obtain more insights in the underlying micro-mechanisms, simple models are employed to describe the mechanical behavior within the experimentally probed range, while two microstructural factors are studied: alloy effects and grain boundary effects.

1. Previous research on Al-alloy thin films optimized for creep has already revealed some influences of the alloy composition, leaving open the question on time-dependent anelasticity and the specific micromechanical influence of each alloy configuration. Simple Al-Cu alloys can already present various micromechanical configurations influenced by various fabrication parameters. Therefore, a known alloy state is created with as little variations as possible to probe its influence. Establishing the various phases and their (inhomogeneous) distribution in the thin films requires a combined characterization approach utilizing scanning and transmission electron microscopy,

X-ray diffraction and energy dispersive spectroscopy.

2. Previous research on the influence of grain boundary, or more general the grain size, has mainly focused on creep in (nano-crystalline) thin films of sub-micron thickness, where a few discussions have shown time-dependent reversible deformation at the nanoscale. Therefore an analysis of the grain boundaries is also of prime interest. For this purpose, electron backscatter diffraction in scanning electron microscopy is employed to yield grain orientation information at the nm-scale and thus precise localization of grain boundaries.

## 1.3 Thesis outline

The outline of the thesis is as follows. First Chapters 2 and 3, supported by appendix A, discuss a microbeam bending methodology: the thermomechanical design of a simple loading mechanism, the strategy to extract the beam curvature evolution from optical profilometry data with the aid of global digital image correlation and the derivation and validation of a linear multi-mode visco-elastic mechanical model to describe the experimental results.

Chapter 4 focuses on the design and development of an on-wafer in-situ nano-tensile test setup capable of characterizing time-dependent anelasticity in uniaxial tension specimens. In this experiment, it is crucial to align the tensile specimen to the loading device, to ensure an overall homogeneous uniaxial tensile state. Innovative quasi-3D image tracking strategies applied to optical profilometry data are combined with features integrated on-wafer to ensure a high degree of alignment. High-reproducibility deformation and force measurements are realized through appropriate correction of the temporally evolving background signals.

Chapters 5 and 6 deal with the experimental investigation of the origin of the time-dependent anelasticity. To this end, the precipitate state is varied through heat treatments, while grain boundary variations are probed through statistical on-wafer variations. Chapter 5 reveals the precipitate state of these thin Al-Cu thin films by using a combination of transmission scanning electron microscopy, electron backscatter diffraction, X-ray diffraction and energy dispersive spectroscopy. Chapter 6 then focuses on the micromechanical characterization of the Al-Cu thin film with respect to precipitate and grain boundary microstructure. The experimental techniques presented in Chapters 2–4 are employed. The micromechanical results are combined with the microstructural information obtained in Chapter 5, and a hypothesis is put forward to explain the time-dependent mechanical behavior. Finally Chapter 7 summarizes the results and conclusions of this research and discusses recommendations for future work.

# Measuring time-dependent deformations in metallic MEMS

---

Reproduced from; L.I.J.C. Bergers, J.P.M. Hoefnagels, N. Delhay, M.G.D. Geers, *Measuring time-dependent deformations in metallic MEMS*, Microelectron. Reliab., 51, 1054–1059, (2011)

### Abstract

The reliability of metallic microelectromechanical systems (MEMS) depends on time-dependent deformation such as creep. Key to this process is the interaction between microstructural length scales and dimensional length scales, so-called size-effects. As a first critical step towards studying these size effects in time-dependent deformation, a purely mechanical experimental methodology has been developed, which is presented here. The methodology entails the application of a constant deflection to a  $\mu\text{m}$ -sized free-standing aluminum-alloy cantilever beam for a prolonged period of time. After this load is removed, the deformation evolution is immediately recorded by acquiring surface topographies through confocal optical profilometry. Image correlation and an algorithm based on elastic beam theory are applied to the full-field beam profiles to correct drift and improve limited optical profilometry precision, yielding the tip deflection as function of time with a precision of 7% of the surface roughness. A proof of principle measurement reveals a remarkable time-dependent deflection recovery. Assumptions and errors of the methodology are analyzed. Finally, it is concluded that the methodology is most suitable for the investigation of creep due to the simplicity of specimen handling, preparation and setup design, whilst maximizing long term stability and deformation precision.

## 2.1 Introduction

Metals as structural components in MEMS find increasing applications, e.g., in radio-frequency MEMS (RF-MEMS) intended for mobile communications applications due to their favorable electrical characteristics. Figure 2.1 shows an example of an RF-MEMS switch. The reliability of these devices has been shown to critically depend on their time-dependent mechanics, such as fatigue and creep, which are affected by temperature [126, 128, 170, 171]. Fatigue affects the device life time through its limitation on the number of device operation cycles, e.g., the number of open/closed cycles of an RF-MEMS switch. Creep can directly affect the operational characteristic, e.g. through a shift in pull-in voltage of an RF-MEMS switch which results in reduced power handling [170]. Fatigue effects may pose less of a problem than expected at small geometrical length scales, whereas creep effects seem to impose more limitations upon miniaturization [44].

The difference between micro- and macroscale creep is generally attributed to so-called size-effects: the interaction between microstructural length scales and dimensional length scales [2, 39]. Although for bulk materials the physical micro-mechanisms of creep are well understood, for thin films this is not the case. Specifically for free-standing metallic thin films, not much research has focused on characterizing size- and temperature-effects in time-dependent material behavior [33], although some research has been conducted on the influence of alloy content and structure on creep in thin metallic films [129, 130]. Therefore, there is a clear need for detailed studies into the physical micro-mechanisms underlying temperature dependent size-effects in creep in metallic MEMS.

As a first step in this direction, the goal of the current work is to construct and validate an experimental *mechanical* methodology to quantify time-dependent deformation of  $\mu\text{m}$ -sized free-standing cantilever beams, which can also be used at elevated temperatures up to 200 °C. To this end, first the experimental methodology is discussed in terms of design choices and data analysis steps. Next, the details of the experimental setup and implementation of the methodology are presented. Subsequently, results of proof-of-principle measurements are presented followed by a critical discussion on the precision of the methodology. To this end, the influence of various errors on the precision is evaluated, where possible quantitatively. Finally, conclusions are drawn with respect to the results of this work.

## 2.2 Design of experiment

Performing mechanical tests on specimens that are free-standing with dimensions in the order of  $\mu\text{m}$ 's is not trivial. Aspects of specimen preparation, handling, loading, load and deformation measurement and control have to be carefully addressed [81] and will be considered in the following.

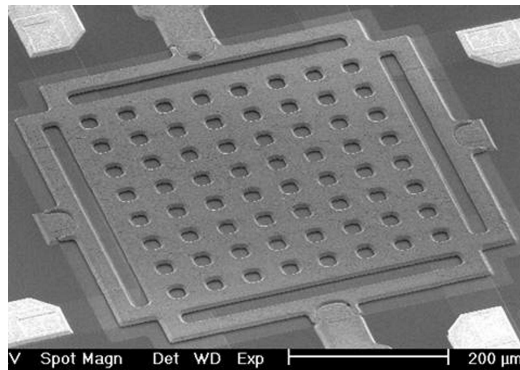


Figure 2.1: Scanning electron microscopy image of an RF-MEMS switch (courtesy of EPCOS Netherlands BV).

## Specimen handling and preparation

The prolonged out-of-plane bending of the hinges in the actual MEMS device raises reliability concerns. Therefore, bending is the deformation mode of interest. Suitable test structures for bending under well defined conditions are free-standing, micron scale cantilever beams, see Fig. 2.2. Considering specimen handling and preparation, it is highly preferred to test on-wafer structures instead of separate  $\mu\text{m}$ -sized structures. Moreover, applying the same micro-fabrication procedure as done for the actual device guarantees the relevance of obtained results.

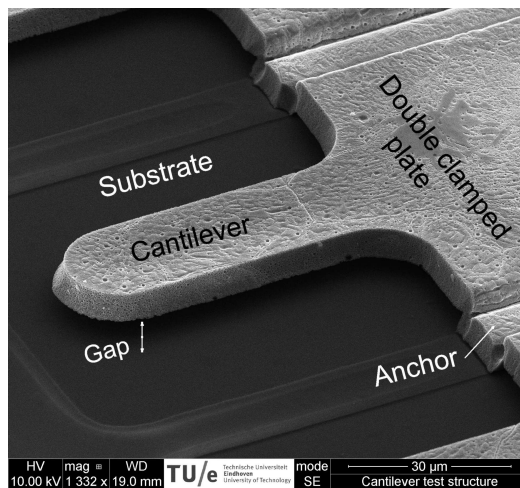


Figure 2.2: A SEM-image of a test cantilever beam that is attached to a free-standing plate clamped on three sides by an anchor.



## Loading method

To characterize parameters in microbeam bending, such as Young's modulus or flow/fracture behavior, several methodologies exist using external/instrumented actuation [76, 122, 180] or even on-chip integrated actuation [23, 24, 34]. However, a critical aspect of the load and displacement control and measurement is long term stability, especially for prolonged time-dependent deformation measurements (at elevated temperature). Therefore, a small, simple fully-mechanical, deflection-controlled mechanism is most suitable. To this end, a so-called micro-clamp is designed, being a simple horizontal knife edge attached to an elastic mechanism, see figure 2.3. A chip with cantilevers is placed under the knife edge, which can be lowered by rotating the thumbscrew, thus pressing and deflecting a cantilever. By using a mono-material, near-monolithic, elastic mechanism the knife edge's vertical position can be controlled to  $< 100$  nm, whilst adjustment screws set the chip's in-plane position. The micro-clamp is placed under a confocal optical proliometer to capture the deformation in time. To complete the design for long term stability, in-plane and out-of-plane thermal expansion are minimized respectively by (i) thermally centering the chip below the knife edge-to-beam contact through placement on a line and point contact and (ii) mounting the knife edge via a piece of the same chip with same thickness and CTE on the elastic hinge.

This micro-clamp has several benefits. First, multiple specimens can be deflected in parallel simply by aligning the specimens on the chip and using a broad knife edge. Second, thermal effects are minimized by effective thermal compensation features. Third, the mechanism can be fabricated using standard milling, polishing and electric discharge machining. Last, but not least, this fully mechanical design avoids uncertainties due to electrical and other drift effects encountered in e.g. electro-static loading [170] or nano-indentation, the latter being practically unfeasible at room temperature, let alone at elevated temperatures, given its temperature sensitivity [158].

## Deformation measurement

To measure the out-of-plane deformation, surface topographies are acquired using optical profilometry. Interferometric profilometry would be ideally suited in terms of height resolution. However, it cannot deal with the large local surface angles associated with the relatively high surface roughness of the metallic MEMS considered here. Confocal profilometry is able to handle a high surface roughness yielding a height resolution in the order of nm's for ideally flat surfaces and high numerical aperture (N.A.) objectives, although for rough surfaces it is less precise. Another factor that limits the resolution is that objectives with sufficient working distance and thus lower N.A. need to be used. It will be shown in the next section how this can be improved.

## Data analysis

Statistical and systematic errors need to be reduced to obtain the cantilever tip deflection as function of time from the surface topographies with sufficient precision. The statistical errors stem from the limitations in optical profiling height resolution and the specimen's

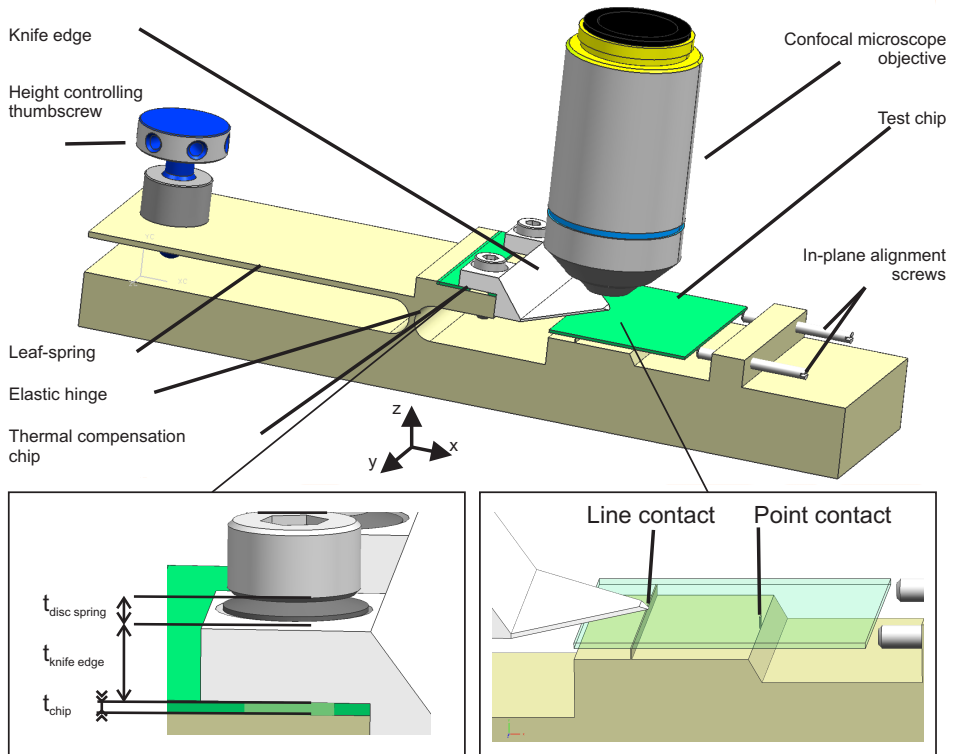


Figure 2.3: Schematic of the micro-clamp beam deflection setup (top) and the features that minimize thermal effects in z-direction (bottom left) and in-plane (bottom right).

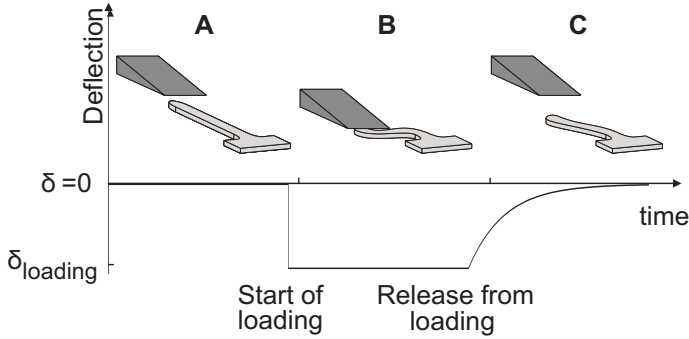


Figure 2.4: Sequence of a micro-beam deflection recovery experiment. (A) The knife edge controlled by the micro-clamp approaches the beam. (B) The knife edge deflects the beam to a depth of  $\delta_{\text{loading}}$  and holds it for a certain period of time. (C) The knife edge is raised, releasing the beam, after which the deflection recovery is measured over time using an optical surface profilometer.

surface roughness. The systematic errors arise due to drift in the optical profilometry set-up causing in-plane and out-of-plane translations as well as rotations about the in-plane axes. To minimize systematic errors a simple image correlation and leveling algorithm will be applied. Finally, statistical errors will be reduced by averaging the full-field data based on elastic beam theory.

## Summary

Based on these considerations, the following experimental methodology is proposed. After prolonged constant deflection controlled by the micro-clamp, see figure 2.4, the time-dependent deflection recovery of micron-sized cantilevers is measured from a sequence of full-field deformation profiles, employing a commercial optical surface profilometer. Data processing is applied to deal with drift in the profilometry set-up and to reduce statistical errors, yielding an overall improvement of the measurement precision. The methodology's benefits are its simplicity, long term stability and deflection precision, without involving highly specialized parts or instruments. The latter two benefits allow for easy and inexpensive parallelization, which is particularly useful for prolonged creep experiments. The only remaining limitation is the lack of a direct measurement of the applied force. Though it is not the focus of this paper, experimental material parameters can be extracted in a straightforward manner for the simple geometry of the cantilevers by an analytical inversion procedure.

## 2.3 Experimental implementation

### Specimen preparation and handling

The cantilevers in this work are produced from Al-(1 wt%)Cu on a test-wafer processed in the same manner as the actual RF-MEMS switches. The Young's modulus is 66.8 GPa, de-

terminated by eigenfrequency measurements and finite element analysis of electro-statically actuated cantilevers [14, 22]. The engineering yield stress  $\sigma_y = 1.8 \cdot 10^2$  MPa is obtained by measuring hardness  $H$  using nano-indentation and applying the Oliver & Pharr methodology in combination with Tabor's relation  $\sigma_y \sim H/3$  [141, 166]. The film thickness is  $4.8 \pm 0.2$   $\mu\text{m}$ . The surface roughness, measured with atomic force microscopy, is  $R_a = 45 \pm 10$  nm. The film consists of columnar, through-thickness grains with  $\{111\}$  surface orientation and an average grain diameter of 20  $\mu\text{m}$ , assuming cylindrical grain shapes, as determined with electron backscatter diffraction. Although several cantilevers with nominal width of 25  $\mu\text{m}$  and various lengths are on the test-chip, here cantilevers of 65  $\mu\text{m}$  length are tested, being a trade-off between practical imaging, deflection depth and induced stress levels.

## Loading method

The precise control of the cantilever deflection is facilitated through near-monolithic fabrication of the micro-clamp from CrNiMo-steel, see figure 2.3. The knife edge height is set through a fine-pitch, play-free, tip-polished thumb-screw that deflects a leaf spring attached to an elastic hinge. This motion is reduced by the leaf spring to elastic-hinge stiffness-ratio and the leaf spring to knife edge length-ratio, yielding a height control of  $< 100$  nm/ $^\circ$  thumbscrew rotation. In-plane adjustment screws allow for planar placement with  $\sim 5$   $\mu\text{m}$  resolution. Furthermore, a so-called thermal compensation chip, a piece of the test-wafer onto which the knife edge is mounted, is crucial for out-of-plane thermal mismatch compensation, resulting in equal z-motion of knife edge and cantilever upon homogeneous temperature changes of the setup. Key for in-plane compensation is the minimized mismatch distance ( $\Delta x = 200$   $\mu\text{m}$ ) between knife edge and line contact in x-direction, whilst in y-direction thermal effects can be neglected assuming no friction between knife edge and cantilever. This design is essential for precise control, of which the performance will be discussed in 2.4.

The micro-clamp is utilized in the loading procedure as follows. The chip is placed and the beam is aligned in-plane to the knife edge under the optical profilometer, whilst leveling the optically flat chip-substrate to within  $0.01$   $^\circ$  is achieved using the manual 2-axis tilt stage of the profilometer. A surface topography of the unaltered beam (reference height position) is then acquired in the confocal profilometer mode. Then, whilst lowering the knife edge with minimal steps ( $< 100$  nm) and simultaneously measuring the beam deflection with profilometry, the beam is deflected to and held for 48 hours at a depth of  $\sim 850$  nm, which is considerably less than the microbeam-substrate gap and corresponds to a maximum stress of  $\sigma_{\text{bend,max}} = 1.0 \cdot 10^2$  MPa  $\sim 0.6\sigma_y$  for this cantilever length. Finally, the unloading procedure is started by lifting the knife edge and immediately capturing surface topographies during  $\sim 6$  hours.

## Deformation measurement

For the deformation measurement, a commercial optical profilometer (Sensofar Plu2300) operated in confocal microscopy mode is employed: 470 nm LED light, 100x long working distance objective with N.A. of 0.7, scan height of 20  $\mu\text{m}$ , data acquisition time of

$\sim 85$  s, motorized XY-translation-stage with  $1 \mu\text{m}$  precision, stabilized on an active vibration isolation table in a temperature controlled room ( $T_{\text{ambient}} = 21.0 \pm 0.5 \text{ }^\circ\text{C}$ ). In this configuration, the RMS repeatability<sup>1</sup> is specified and verified to be  $< 10$  nm on a calibration mirror. However, the RMS repeatability measured on the actual surface of several test structures and chips is not as good:  $80 \pm 25$  nm, clearly showing that the surface roughness of  $R_a = 45$  nm with locally high surface slopes, negatively affects the measurement precision.

## Data analysis

Errors due to drift of the translation and tilt stage of the profilometer will worsen the precision beyond the 80 nm RMS repeatability and deteriorate the overall accuracy due to their systematic nature. Therefore, first a straightforward image correlation algorithm is used that aligns the test structure edges, to compensate for x and y translations with pixel resolution. Rotations around the axis perpendicular to the surface have been validated to be negligible. Second, tilt around x and y-axis and drift in z-direction are corrected by applying a linear leveling algorithm, using the double clamped plate as reference, see figure 2.5. The out-of-plane deformation at the areas of the plate used as a reference for leveling will be shown to be negligible with respect to the measurement precision, see section 2.4. Third, after correcting systematic errors leaving the statistical error due to the RMS repeatability for high surface roughness, the precision of determining the tip deflection  $u_{\text{tip}}$  is crucially improved by fitting standard beam bending theory to the full-field deformation data of the beam. This key step uses the intrinsic assumptions, verified in section 2.4, that the bending is elastic and the double clamped plate rigidly fixes the cantilever.  $u_{\text{tip}}$  is obtained by first subtracting the profile of measurement  $i$  from the reference profile, yielding the deformed profile. Then area bins ( $16 \times 1 \mu\text{m}^2$ ), over which the surface height is averaged, are created along the length of the beam and plate giving the deflection profile, see figure 2.5. Finally, the equation for a single clamped beam is fit to the profile yielding  $u_{\text{tip}}$ .

## 2.4 Results and discussion

### Proof of principle measurements

The result of the measured deflection recovery is a sequence of profiles, shown in figure 2.6, from which  $u_{\text{tip}}$  as function of time is determined, as shown in figure 2.7. After an instantaneous initial spring back of more than 95% of the loading depth, the beam shows a relatively small, though clear monotonous increase in height of  $\sim 25$  nm over a time period of about 5 hours. This reveals a time-dependent recovery of the cantilever. Next to this, no permanent deflection is observed. Repetition of these measurements for several similar beams shows consistent results.

To assess the precision of the measurement, the standard deviation is determined of the tail

---

<sup>1</sup>RMS repeatability is defined as the root-mean-square value of the height difference profile calculated from two subsequent height measurements of the same surface.

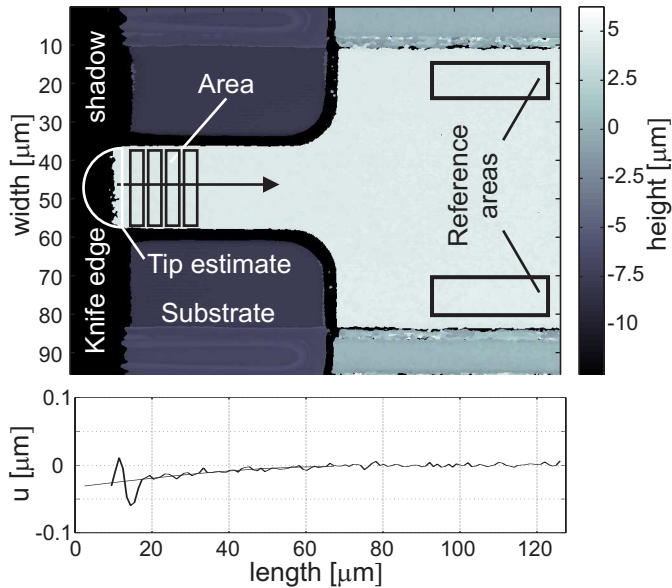


Figure 2.5: Surface topography illustrating data processing steps to obtain the tip deflection from surface height maps: 1) image correlation to align the profiles in XY-direction, 2) linear plane fitting based on reference areas to correct for tilt around x and y axis and drift in z-direction, 3) subtraction of the measured profile  $i$  from the undeformed profile to deduce the deformed profile, 4) averaging the heights of boxed areas along the beam to deduce the deflection profile, 5) fitting a standard beam bending equation to the deflection profile to extract  $u_{tip}$  (thin line in lower graph).

of the measurement ( $t > 2.5 \cdot 10^4$  s, not shown in figure 2.7), where the deflection has fully saturated. This yields a precision of ( $1\sigma$ ) of  $\sim 3$  nm. The resulting precision is remarkably good considering the surface roughness of 45 nm or the achieved 80-nm RMS repeatability of the confocal profilometry. This shows that the proposed methodology yields a precision of  $< 7\%$  of  $R_a$  or  $< 4\%$  of the obtained RMS repeatability.

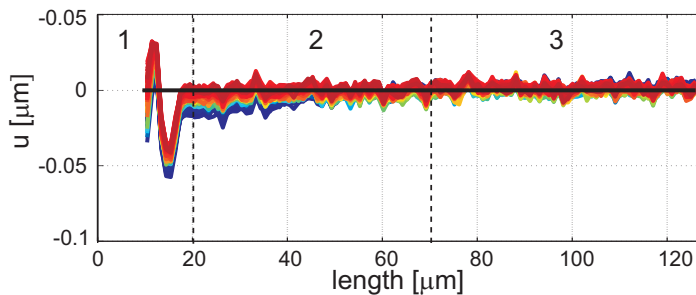


Figure 2.6: Cantilever deflection profiles after data processing of the deflection recovery experiment. The initial profile acquired before any deflection is plotted in black. The first profile acquired after unloading is plotted in blue and subsequent profiles are plotted with a gradient from blue to red. Three sections are distinguished: (1) unreliable data due to partial blocking of reflected light by the knife edge, (2) the cantilever deflection profile, and (3) the plate profile.

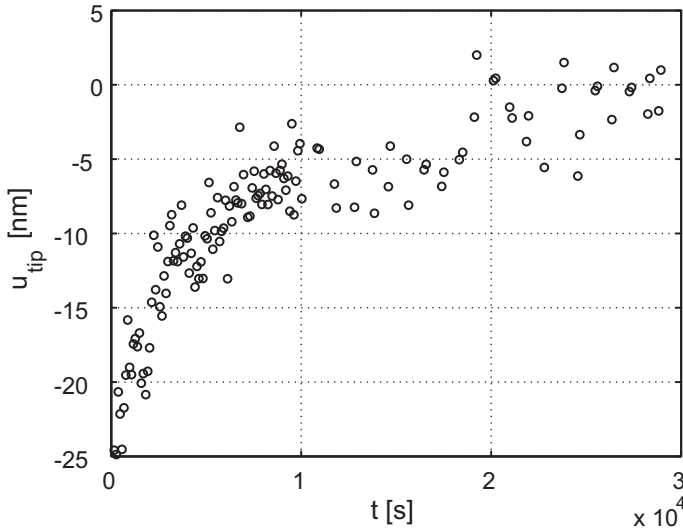


Figure 2.7: The measured time-dependent deflection recovery showing the tip deflection  $u_{\text{tip}}$ , obtained from the data in figure 2.6, as function of time.

## Error assessment

As discussed in section 2.2, there are statistical and systematic errors that affect the measurement precision. Here, we assess the correction of the systematic errors. First, the tilt correction assumes that the deformation of the double clamped plate is negligible, i.e. the plate is rigid and the cantilever is rigidly clamped. This needs validation. Second, the in-plane drift correction with an image correlation algorithm that correlates to pixel and not sub-pixel precision, is evaluated. Lastly, systematic errors stemming from (ever-present) temperature influences are discussed.

The assumption of the negligible deformation of the double clamped plate is analyzed by finite element analysis (FEA). A linear elastic model can be employed as the loading is below the (engineering) elastic limit. The model consists of 3D, 20-node, second order, iso-parametric elements (commercial FEA-package, Marc Mentat), see figure 2.8. Only half of the structure is modelled due to symmetry. To carefully simulate the experimental geometry (figure 2.2), the clamped plate ( $\sim 130 \mu\text{m}$  long) is completely modeled together with the anchors, where the boundary conditions (fixed displacements) are applied. A deflection of 100 nm is applied at the tip, corresponding to an upper limit on the deflection immediately after unloading. The resulting deformation of the plate, shown in figure 2.8, reveals that the plate deflects downwards at the attachment of the beam, whilst it rises at the center. This rise is limited though to  $< 0.5 \text{ nm}$ , whereas it is  $< 0.2 \text{ nm}$  in the regions selected for leveling and height reference, i.e.  $< 0.1\%$  of the tip deflection. Thus, it is concluded that the deflection of the reference areas negligibly affects the overall precision.

To investigate the remaining systematic error after the image correlation step, a random topography is investigated where this topography is shifted with one pixel in every direction with respect to its original position. Then the profiles are processed the same way as described in section 2.3, which yields an upper limit of  $\sim 3 \text{ nm}$  in the error of the tip

deflection due to limitations of the in-plane image correlation, see figure 2.9.

Finally, the errors due to temperature fluctuations are discussed, except those inducing stage drift, of which the effect pertains to the previously discussed error. These fluctuations affect the microclamp, possibly changing the cantilever position with respect to the micro-clamp. They do not affect the tip deflection *recovery* measurement, because the free-standing thin film expands/contracts freely. During *loading*, however, the knife edge and cantilever are in contact. The thermal loop then consists of the micro-clamp, the knife edge, its disc spring fixation, the silicon substrate and the aluminum cantilever. In z-direction, the difference in thermal expansion stems from the difference in thickness ( $< 20$  nm) between test chip and thermal compensation chip, because the latter is compressed by the disc spring fixation ( $\sim 50$  N). This thickness difference results in an expansion difference of  $\Delta z/\Delta T < 5 \cdot 10^{-4}$  nm/ $^{\circ}\text{C}$ , i.e. the knife edge lowers  $< 0.1$  nm for  $\Delta T = 200$   $^{\circ}\text{C}$ . Without this compensation chip  $\Delta z/\Delta T \sim 10$  nm/ $^{\circ}\text{C}$  would hold, i.e. the knife edge would rise by 200% at 1  $\mu\text{m}$  initial deflection for  $\Delta T = 200$   $^{\circ}\text{C}$ ! In x-direction, a thermal mismatch exists between micro-clamp and chip over the mismatch distance (200  $\mu\text{m}$ ), resulting in  $\Delta x/\Delta T < 3$  nm/ $^{\circ}\text{C}$  or  $\Delta x < 600$  nm for  $\Delta T = 200$   $^{\circ}\text{C}$ , changing the tip deflection relatively by  $< 3\%$ . Without this design, the far edge of the inherently non-flat chip may stick to the clamp resulting in  $\Delta x/\Delta T \sim 100$  nm/ $^{\circ}\text{C}$ ! In conclusion, this analysis shows that the setup is rather insensitive not only to small changes at room temperature, but also up to  $\Delta T = 200$   $^{\circ}\text{C}$ , making it ideally suited for prolonged testing at elevated temperatures.

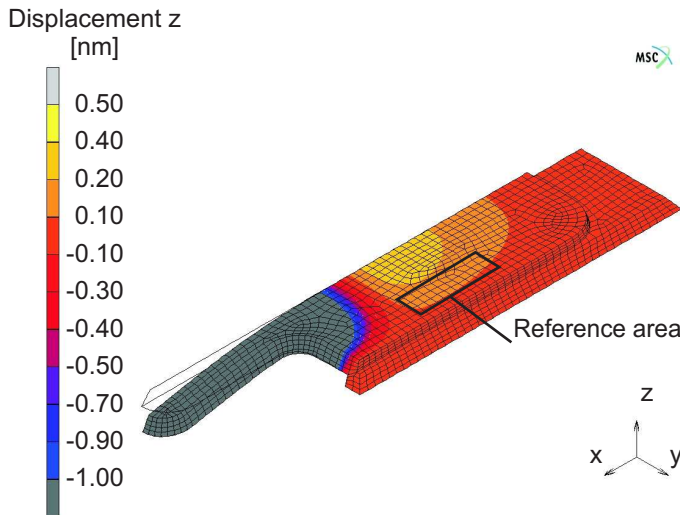


Figure 2.8: Finite element simulation of the height deformation of the beam and the double clamped plate at 100 nm deflection of tip. The deformation is magnified and the scale range is adjusted to visualize the small variations of the deformation of the plate. Black indicates deflection below a depth of 1 nm. The model shows the plate is raised in the center by  $< 0.5$  nm. The height of the areas selected for reference height and leveling remains within 0 – 0.2 nm.



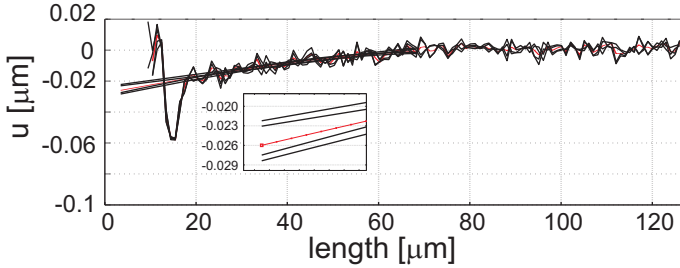


Figure 2.9: The influence of an erroneous xy-correlation on the overall profile fit. The topography is shifted 1 pixel in the horizontal and vertical direction to imitate the possible deviation introduced by the image correlation procedure. The inset shows a zoom around the original profile (dashed red line) indicating a maximum error of  $\sim 3$  nm.

## 2.5 Conclusion

An experimental methodology has been presented to measure time-dependent deformation in  $\mu\text{m}$ -sized free-standing cantilevers. As a first result, the deformation recovery after initial spring back of a cantilever is measured over a period of  $\sim 6$  hours, showing a recovery of 25 nm during this period thereby eliminating permanent deflection. The precision is 3 nm, corresponding to  $< 7\%$  of the surface roughness or  $< 4\%$  of the 80-nm RMS repeatability of the surface profilometry of these specimens. This is remarkably good considering the relatively high surface roughness and experimental limitations.

The measurement is made possible due to the well-considered design of experiment: measurement of time-dependent recovery with confocal profilometry in a simple mechanical setup with minimal specimen handling. A micro-clamp deflects on-chip micro-cantilevers to a depth controlled with  $< 100$  nm resolution. Simple image correlation and leveling algorithms are applied to the measured surface profiles to correct for profilometer stage drift, whilst standard beam bending equations applied to the full-field deformation data of the beam further improve the measurement precision. Error sources due to thermal mismatch and drift correction in tilt and translations are analyzed to verify the relative insensitivity of the micro-clamp design to thermal effects and the assumptions made in the image processing. This analysis shows that the obtained tip deflection precision is reliable and that the setup is suitable for elevated temperature testing. The observed time-dependent deflection recovery is an interesting manifestation of creep. The next step, therefore, is to apply time-dependent material models to extract physically meaningful parameters, the procedure of which will be discussed in the following chapter.

## Acknowledgements

Dr.ir. M.A.J. van Gils and ir. J.A. Bielen at EPCOS Netherlands B.V. are greatly acknowledged for their cooperation, support and fruitful discussions in this work.

# Chapter 3

## Characterizing time-dependent anelastic microbeam bending mechanics

---

Reproduced from; L.I.J.C. Bergers, J.P.M. Hoefnagels and M.G.D. Geers, *Characterizing time-dependent anelastic microbeam bending mechanics*, J. Micromech. Microeng., in preparation

### Abstract

This chapter presents an accurate yet straightforward methodology for characterizing time-dependent anelastic mechanics of thin metal films employed in MEMS. The deflection of microbeams is controlled with a mechanical micro-clamp, measured with digital holographic microscopy (DHM) and processed with global digital image correlation (GDIC). The GDIC processing directly incorporates kinematics into the 3D correlation problem, describing drift-induced rigid body motion and the beam deflection. This yields beam curvature measurements with a resolution of  $< 1.5 \cdot 10^{-6} \mu\text{m}^{-1}$ , or for films thinner than  $5 \mu\text{m}$ , a strain resolution of  $< 4 \mu\epsilon$ . Using a simple experimental sequence, these curvature measurements are then combined with a linear multi-mode time-dependent anelastic model and a priori knowledge of the Young's modulus. This allows the characterization of the material behavior in the absence of an additional explicit force measurement, which simplifies the experimental setup. Using this methodology we characterize the anelasticity of  $5 \mu\text{m}$ -thick Al(1wt%)-Cu microbeams of varying microstructures over relevant timescales of 1 to  $1 \cdot 10^5$  s and adequately predict the time and amplitude response of experiments performed for various loading conditions. This demonstrates the validity of the methodology and the suitability for thin film mechanics research for MEMS development.

### 3.1 Introduction

The reliability of metallic microelectromechanical systems (MEMS) has been shown to critically depend on time-dependent mechanics such as creep, with an increasing detrimental influence upon miniaturization [44, 171, 173]. For example, in a radio frequency MEMS switch (Fig.3.1), creep appears as both a viscoelastic and plastic effect over timescales of seconds to days. This directly affects the operational characteristics, e.g. through a shift in pull-in voltage resulting in reduced power handling [99, 170]. Reliable operation of metallic MEMS requires accurate modeling of the electrical and mechanical behavior. Traditional mechanical models do not properly account for the interplay between the reduced device structural and microstructural length scales, so called size-effects [2, 39] and thus fail to accurately describe the mechanics. Furthermore, statistical effects also play a significant role [62], because of microstructural variations from specimen to specimen, which are inherent to the microfabrication of such small structures. Predictive capabilities for device development and systematic investigations into the underlying micromechanics, however, require characterization of (long-term) time-dependent mechanics at the microscale. To this purpose a suitable methodology is developed in this paper.

In the following we discuss the methodology to highly precisely measure on-wafer deformations and effectively combine this with a simple model. The procedure for on-wafer deformation measurement relies on state-of-the-art digital holographic microscopy (DHM) and a novel global digital image correlation (GDIC) algorithm. Next the mechanical behavior is characterized based on an anelastic model to obtain model parameters from the experiments. Finally the reliability of the methodology is assessed by predicting the deformation evolution in subsequent measurements under different loading conditions.

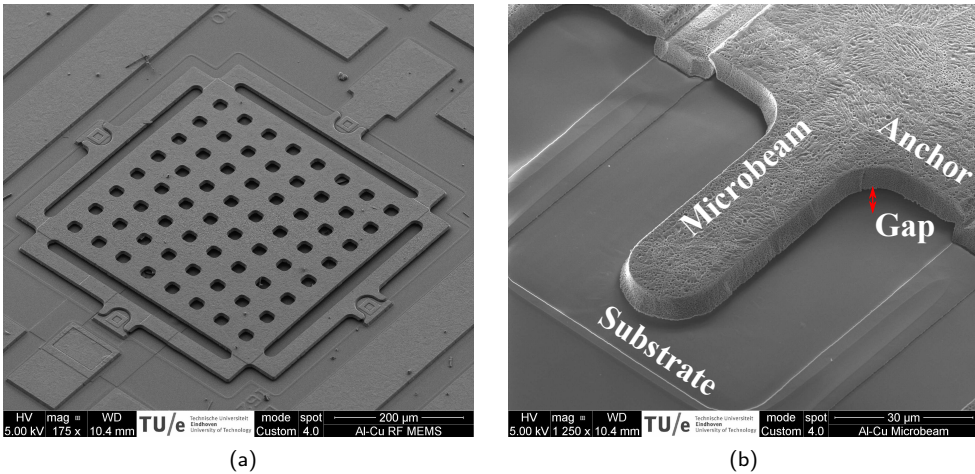


Figure 3.1: SEM images of (a) a metallic RF-MEMS switch, which consists of a plate attached to anchored hinging beams, and (b) test cantilevers easily co-fabricated on the same die as the RF-MEMS switch.

## 3.2 Strategy

A reliable methodology for characterizing time-dependent mechanical behavior should meet the following requirements. First it uses easily reproducible specimens that can be integrated into actual (test-)MEMS designs. This facilitates testing multiple specimens to probe statistical effects, yielding data directly applicable to the device. Second, highly stable loading and measuring methods are necessary, because the behavior of interest typically spans time scales from  $10^{-1}$  to  $10^5$  s. Preferably a simple mechanical device is employed, assuring high stability with a minimal amount of components to provide a simple, reproducible, hysteresis-free loading. Optical profilometric techniques are most ideal for high-speed, long-term deformation measurements as these provide full-field height data [16]. Third, as drift is inevitably present at these length and time scales due to the separate loading and measuring devices, the full-field data can be used to measure the drift from non-deforming parts of the wafer. Sensitive drift correction, however, requires an accurate algorithm to extract the deformation from the full field drift-affected data. Finally, a simple and sufficiently accurate mechanical model should be in place to characterize the time-dependent mechanical behavior for design purposes.

A few methods exist for mechanical characterization of time dependent mechanics at the microscale. With timescales of interest between  $10^{-1}$  to  $10^5$  s, the low frequency anelastic behavior is of particular interest in this study. Anelasticity has been characterized with high frequency microbeam vibration [29, 32], bulge testing [88, 91, 92, 185] and tensile testing [108, 109, 115], whilst creep has been characterized with bulge testing [93] and wafer curvature measurements [129, 130]. These methods directly or indirectly measure forces and scalar displacements, yielding stress and strain data for model characterization. However, they require dedicated specimens and processing methods, limiting specimen variation, handling and integration with actual device wafers. On-wafer microbeams, see Fig.3.1 are well suited due to their simple geometry allowing for easy variation and co-fabrication with the device wafer. Moreover, they enable simple mechanical loading by deflection, resembling the critical deformation states in RF-MEMS.

Microbeam bending experiments have been performed with instrumented indentation [53, 159], or on-chip test structures [34]. Although instrumented indentation allows for both force and deflection measurements, the uncertainties in loading position, local deformations and long-term instrument stability entail poor reproducibility. The on-chip test structures elegantly integrate the entire test, which simultaneously poses limitations: the required actuation and acquisition electronics for long-term highly sensitive measurements are non-standard, while additionally the chip is optimized for a limited range of specimen geometries. Previously, we developed a fully mechanical, hysteresis-free microbeam loading mechanism [9], employing confocal profilometry for deflection measurement. Although the loading device provides excellent stability, the confocal profilometer shows significant irregularities over long periods, due to limited long-term closed-loop positioning accuracy resulting from its vertical scanning principle [1]. Therefore a non-scanning optical technique is required for reproducible microbeam bending measurements.

Deformation measurements using non-scanning optical techniques are laser beam deflection [127], wafer curvature [56] or multiple wavelength DHM [105]. Although the former two have high sensitivity, they are not preferred, because they either require a relatively

large surface or yield a single point measure that necessitates a sophisticated setup design to eliminate drift effects. However, dual wavelength DHM [59, 105], is well suited, because it acquires holograms that contain the object’s full-field height information with nm-resolution over depths equal to the synthetic wavelength generated by low-frequency beating of the two wavelengths. Another benefit is the imaging speed that is only limited by the camera’s acquisition rate. Additionally, the full-field profilometric data can contain deformation-free areas for the required drift correction. In order to minimize systematic error, we here develop a novel algorithm based on GDIC [83], that has recently been extended to quasi-3D [140]. The algorithm uses the specific kinematics involved in this experiment to optimally extract a limited set of kinematical degrees of freedom yielding maximum accuracy. The complete 3D displacement field is differentially measured between a static reference profile and a drifted and deformed profile. This yields the beam curvature, from which the strain results for known beam thickness. Thus, the combination of DHM with quasi-3D GDIC enables high-reproducibility deformation measurements.

The anelasticity can be analyzed and characterized by exploiting the measured kinematics. Often stress relaxation or vibration experiments are performed [28, 88, 91, 107, 157, 185] to characterize (multi-mode) linear viscoelastic models. The simplicity of the adopted loading device precludes explicit force measurements. However, we overcome this by performing an experiment at constant applied deformation followed by a fully unloaded state, i.e. no applied external forces. Combining this with a simple model, parameters can be extracted from these particular loading conditions. It assumes that forces are implicitly known in case of a known Young’s modulus,  $E$ , which can be obtained from literature or a different experimental technique. This approach allows the characterization of the mechanical behavior for time scales relevant to MEMS devices in a simple setup without explicit force measurement.

### 3.3 Curvature measurement

To measure anelastic microbeam curvatures, a micro-clamp loading device[9] is placed under a DHM, see Fig.3.2. The micro-clamp has a polished horizontal knife edge attached to a simple leafspring mechanism controlled by a thumbscrew. The mechanism reduces the ingoing thumbscrew motion to a z-displacement of the knife edge with a resolution of  $\sim 50$  nm. Thermal expansion effects in the loading mechanism are minimized by fabricating the mechanism and knife edge from the same material, placing a dummy wafer in the loading loop, and constructing a thermal center near the loading point. The resulting thermal sensitivity of the applied deflection is  $\leq 0.1$  nm for  $\Delta T = 200$  °C. A Lyncée tec DHM R2100 dual wavelength holographic microscope ( $\lambda_1 = 682.5$  nm,  $\lambda_2 = 758.5$  nm) is employed, utilizing a 20x objective with N.A= 0.4, placed in an environmentally controlled room with  $T = 20.5 \pm 0.2$  °C.

DHM is an upcoming profilometric technique [100]. The working principle is the digital acquisition of a hologram obtained by interfering a reference monochromatic wave of wavelength  $\lambda$  with a wave split from this reference and scattered from an object [36, 37, 100]. This is realized in a single snapshot without any scanning parts, providing this DHM an acquisition rate  $f_{\text{acq.}} < 10$  Hz. Higher rates have been demonstrated, e.g., for dynamic MEMS characterization [132]. From this hologram an intensity image and phase image

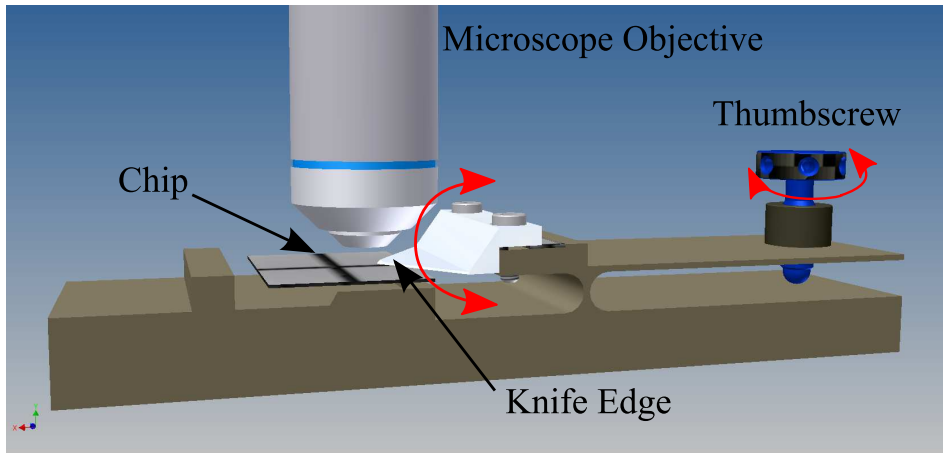


Figure 3.2: Schematic side view of the micro-clamp used to deflect on-chip cantilevers with high resolution under a profilometer. Thermal and mechanical drift effects in the load are minimized through a dedicated thermomechanical design.

are reconstructed digitally, where in a reflection configuration the latter is a direct representation of the object's topography. The employed DHM yields a height resolution of  $\sim 10$  nm, at a typical noise level of 1-2%, over a range of 341 nm, ( $0.5\lambda_1$ ), for the reflection configuration used in profilometry. This technique therefore enables high speed acquisition of full-field height profiles of the microbeams with 10 nm resolution.

A limitation of phase measuring profilometer techniques is the occurrence of phase discontinuities for path length differences  $> 0.5\lambda$ , caused by step heights, (microfabrication induced) surface roughness, or large deflections, as used in this work. This problem is normally addressed by phase shift strategies or sophisticated unwrapping algorithms [100]. In addition to unwrapping algorithms, the DHM can operate simultaneously with two wavelengths  $\lambda_1, \lambda_2$ , that create a synthetic long beat wavelength  $\Lambda_s$  and remove the phase ambiguity [59, 105]. This operation is illustrated in Figs.3.3a-f in 1D for a deflected beam, of which the true height profile is shown in Fig.3.3a. Each individual wavelength  $\Lambda_i$  produces phase  $\Phi_i$  c.q. height profiles  $h_i$  as depicted in Fig.3.3b-c, where measurement noise of  $\epsilon = 0.02\Phi_i$  is introduced. The algorithm used in this approach subtracts the measured phases from each other resulting in the phase difference  $\Phi_2 - \Phi_1$ , see Fig.3.3d. This reveals jumps where  $\Phi_2 > \Phi_1$ , which are simply removed by adding  $\pm 2\pi$  to yield the phase  $\Phi_s$  and height profile  $h_s$  of the synthetic wavelength  $\Lambda_s$ , see Figs.3.3e,f. These do not contain the phase jumps along the deflecting part present in Figs.3.3b-c.

The resulting height profile in Fig. 3.3f, however, reveals an absolute noise level along most of the profile that is significantly larger than the noise in  $h_i$ , as well as large phase jumps where  $\Phi_s \sim \text{modulo}2\pi \pm \epsilon$ . The former can be improved by the so-called mapping of the data from a short wavelength onto the synthetic wavelength [59, 105], whilst the latter can be improved by algorithms detecting phase jumps. The mapping procedure segments the height profile  $h_s$  in Fig.3.3f in integer multiples of  $\lambda_1$ , or  $\lambda_2$ , see  $h_{s,\text{seg}}$  in Fig.3.3g, and adds the corresponding segments of  $h_1$  to the corresponding segment in  $h_{s,\text{seg}}$ , hence

creating the mapped height profile  $h_m$ , see Fig.3.3h. This extends the measurement range to  $0.5\Lambda_s = 3406$  nm, while reducing the noise level along most of the profile to the single wavelength noise level.

However, the mapping procedure is still sensitive to noise where either  $\Phi_i$  is  $\sim 2\pi$  modulo, see the phase jumps and spikes in Figs.3.3b,c,h, prohibiting nm-precise microbeam bending measurements. For noise  $\epsilon_1 < \lambda_1/(4\Lambda_s)$  a simple correction procedure exists [59]. Noise exceeds this level for optically non-smooth surfaces, as is the case for the employed metallic microbeams and many other microstructures, introducing significant spikes in the mapped surface profile, see Fig.3.3i. This problem is resolved by correcting spikes in  $h_m$  with a 2D areal phase-jump detection algorithm. The algorithm removes the  $2\pi$  modulo in the phase difference  $\Delta\Phi$  between an uncorrected pixel in  $\Phi_m$ , and the average phase  $\bar{\Phi}_{m,\text{corrected}}$  in an  $m \times n$  facet of already corrected pixels surrounding that pixel. The very first pixel is assumed to be free of phase jumps. The values of  $m$  and  $n$  are optimized to contain enough pixels for a representative average, whilst still being able to follow the deflecting profile of the beam, i.e. large  $n$  and small  $m$ . This effectively removes the spikes in the continuous areas on the surface of the microbeam, see Fig.3.3j. Another benefit is that it removes the phase jumps occurring for  $\Delta h_s > 0,5\Lambda_s$ , thus extending the height range to the light source's coherency length.

Elastic beam deformations result in nm-level deflection changes, requiring precise data processing in order to deal with drift and noise induced by thermal effects, optics, humidity, vibrations and surface roughness. Global digital image correlation (GDIC) [83] is used to obtain the displacement field between an undeformed reference profile and a deformed and displaced profile, see Fig.3.4a,b. It is based on the principle of brightness conservation, where surface patterns are matched between images. This has recently been extended to quasi 3D, i.e. obtaining a 3D displacement field as function of the 2D position field while matching (natural) surface features [140], i.e. in this work the surface roughness of the micromachined microbeams. A minimization problem is formulated from the conservation with the displacement field parameterized by global degrees of freedom (dofs). For the case of interest here, the global kinematical dofs are the microbeam deflection and the drift-induced rigid body translations and rotations. A novel aspect is that the dofs for deflection are based on Euler-Bernoulli kinematics and limited to a sub-region, the deflecting beam, in stead of the entire profile, being the beam and its anchor. Solving this GDIC problem yields the deflection directly. By taking the double derivative of the deflection along the beam's longitudinal direction the curvature is obtained.

The quasi-3D GDIC principles are detailed next. A more detailed description can be found in App.A. The brightness conservation, here representing height profiles, states that the reference image, represented by the height field  $f(\vec{x})$  on position field  $\vec{x}$ , Fig.3.4a, is related to the deformed image,  $g(\vec{x})$ , Fig.3.4b, through the in-plane displacement field  $\vec{u}_{xy}(\vec{x})$  and the out-of-plane displacement field  $\vec{u}_z(\vec{x})$  and measurement noise  $n_0(\vec{x})$ :

$$g(\vec{x} + \vec{u}_{xy}(\vec{x})) = f(\vec{x}) + u_z(\vec{x}) + n_0(\vec{x}). \quad (3.1)$$

The unknown 3D displacement field  $\vec{u}(\vec{x})$  is obtained by minimizing the global residual  $\eta$  of Eq.(3.1) integrated over the considered region of interest (ROI)

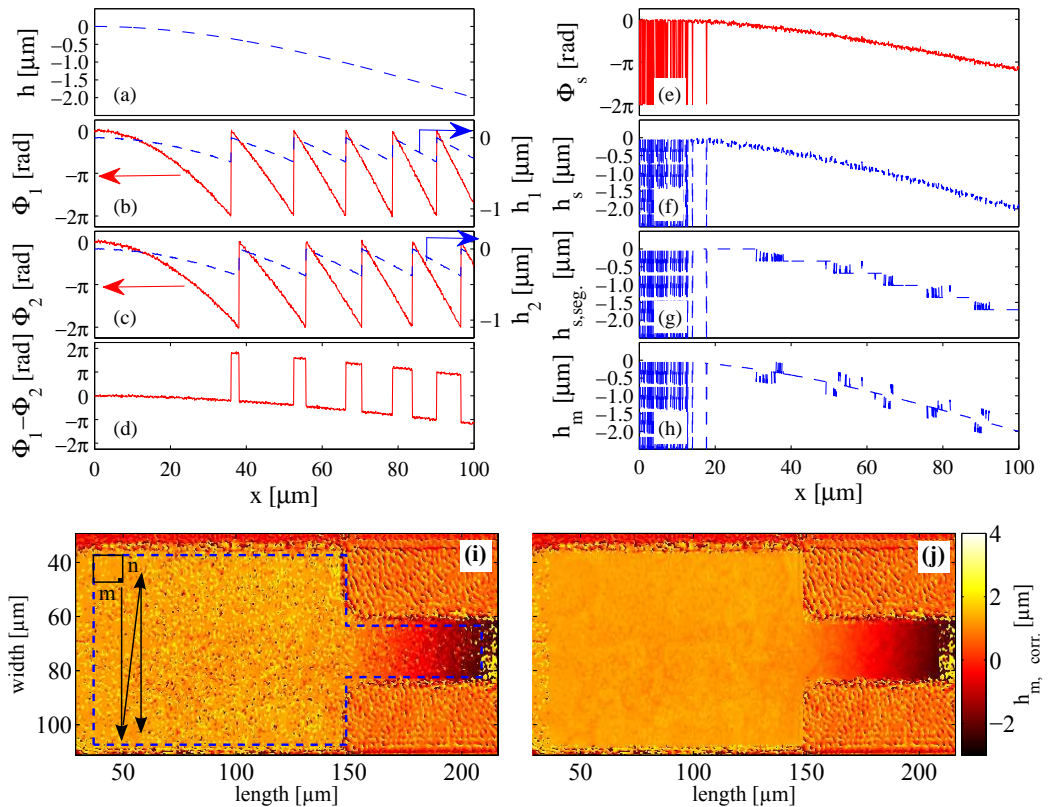


Figure 3.3: (a-h) Sequence illustrating the dual wavelength height profile measurement and mapping principle for a simulated deflected microbeam: (a) height profile  $h$ , (b) phase  $\Phi_1$  (red solid line) and height  $h_1$  (blue dashed line) measured by wavelength 1, (c) phase  $\Phi_2$  (red solid line) and height  $h_2$  (blue dashed line) measured by wavelength 2, (d) phase difference  $\Phi_2 - \Phi_1$ , (e) phase of synthetic wavelength  $\Phi_s$ , (f) height profile  $h_s$  calculated from  $\Phi_s$ , (g) segmented height  $h_{s,seg.}$ , (h) mapped height  $h_m$  (i) Mapped height image shows many spikes that remain after mapping. A pixel-wise correction algorithm is applied in a facet (solid box) that is shifted in a region of interest (dashed box). (j) Corrected mapped height image revealing the microbeam surface topography.

$$\eta^2 = \int_{\text{ROI}} [(f(\vec{x}) - g(\vec{x} + \vec{u}_{xy}(\vec{x})) + u_z(\vec{x}))^2] d\vec{x} = \int_{\text{ROI}} r(\vec{x})^2 d\vec{x}, \quad (3.2)$$

where  $r(\vec{x})$  is the residual field. The displacement field is parameterized and interpolated using a set of basis functions  $\phi_n(\vec{x})$  defined globally over the region of interest and involving a discrete set of dofs  $\psi_n$  according to

$$\vec{u}(\vec{x}) = u_x(\vec{x})\vec{e}_x + u_y(\vec{x})\vec{e}_y + u_z(\vec{x})\vec{e}_z = \sum_n \psi_n \phi_n(\vec{x})\vec{e}_i, \quad (3.3)$$



Table 3.1: Kinematic degrees of freedom describing the displacement field.

Displacement field component	Description	Active area
Drift translation x-direction	$u_x(\vec{x})\vec{e}_x = \psi_x\vec{e}_x$	ROI
Drift translation y-direction	$u_y(\vec{x})\vec{e}_y = \psi_y\vec{e}_y$	ROI
Drift translation z-direction	$u_z(\vec{x})\vec{e}_z = \psi_z\vec{e}_z$	ROI
Drift rotation about x-axis	$u_z(\vec{x})\vec{e}_z = \psi_{z,x}y\vec{e}_z$	ROI
Drift rotation about y-axis	$u_z(\vec{x})\vec{e}_z = \psi_{z,y}x\vec{e}_z$	ROI
Microbeam deflection	$u_z(\vec{x})\vec{e}_z = \psi_{zEB}(-(x - x_{\text{root}})^3/(6l) + (1/2)(x - x_{\text{root}})^2)\vec{e}_z$	Only $\mu$ -beam

where  $i = [x, y, z]$ . The drift here results in a translation in  $x, y$  and  $z$ -direction as well as a tilt around  $x$ - and  $y$ -axis, while the deflection results in an additional displacement in  $z$ -direction. Table 3.1 lists the kinematical dofs. Fig.3.4a illustrates the ROI for the drift components, whereas Fig.3.4c-e emphasize the linear combination in  $u_z$  of the drift, acting within the entire ROI, and the deflection component, acting only on the beam.

For the deflection component  $w$  simple Euler-Bernoulli kinematics are assumed [52]. The deflection of a cantilever that is clamped at  $x_{\text{root}}$  and loaded by a point load at  $x = l$ , is:

$$w(x) = \kappa_{x_{\text{root}}} \left( \frac{-(x - x_{\text{root}})^3}{6l} + \frac{1}{2}(x - x_{\text{root}})^2 \right) \quad (3.4)$$

in which the constant  $\kappa_{x_{\text{root}}}$  is the curvature at the root. The second derivative of Eq.3.4 with respect to  $x$  is taken to obtain the curvature profile  $\kappa(x)$ . To ensure that both the deflection *and* curvature profiles match the Euler-Bernoulli kinematics, the dofs directly involve the constant  $\kappa_{x_{\text{root}}}$ , i.e.  $\psi_{zEB} = \kappa_{x_{\text{root}}}$ , see Table 3.1, whereas  $x_{\text{root}}$  and  $l$  are fixed parameters directly measured from the profilometric data. This reduces the set of dofs, which benefits the minimization routine. More importantly, it also reduces the noise in the curvature, especially at the edges of the sub-region. This is of concern, because strain changes are largest at the beam's root  $x_{\text{root}}$ . Note that  $x_{\text{root}}$  is not at the edge of the anchor, but effectively 10 – 15  $\mu\text{m}$  on top of the anchor, because of finite anchor stiffness. Although in principle this location depends on the geometry and load, it is adequate to identify it for one geometry at maximum load, because for smaller loads, and thus deflections, its influence is smaller. In practice  $x_{\text{root}}$  is identified by observing the deformation zone around the root. Finally, to best compare beams of different length, the curvature at the edge of the anchor  $x_{\text{edge}}$  is used for further analysis:

$$\kappa(x_{\text{edge}}) = \psi_{zEB} \left( \frac{-(x_{\text{edge}} - x_{\text{root}})}{l} + 1 \right) \quad (3.5)$$

A set of experiments is performed on two different chips fabricated at an industrial wafer fab. On each chip three cantilevers are deflected in parallel at  $x \sim 125 \mu\text{m}$  up to  $w \sim 2 \mu\text{m}$  for  $1 \cdot 10^5$  s (chip 1) and  $1.5 \cdot 10^5$  s (chip 2), after which the load is removed and the subsequent recovery evolution is recorded for  $1 \cdot 10^5$  s. For chip 2 the unloading was

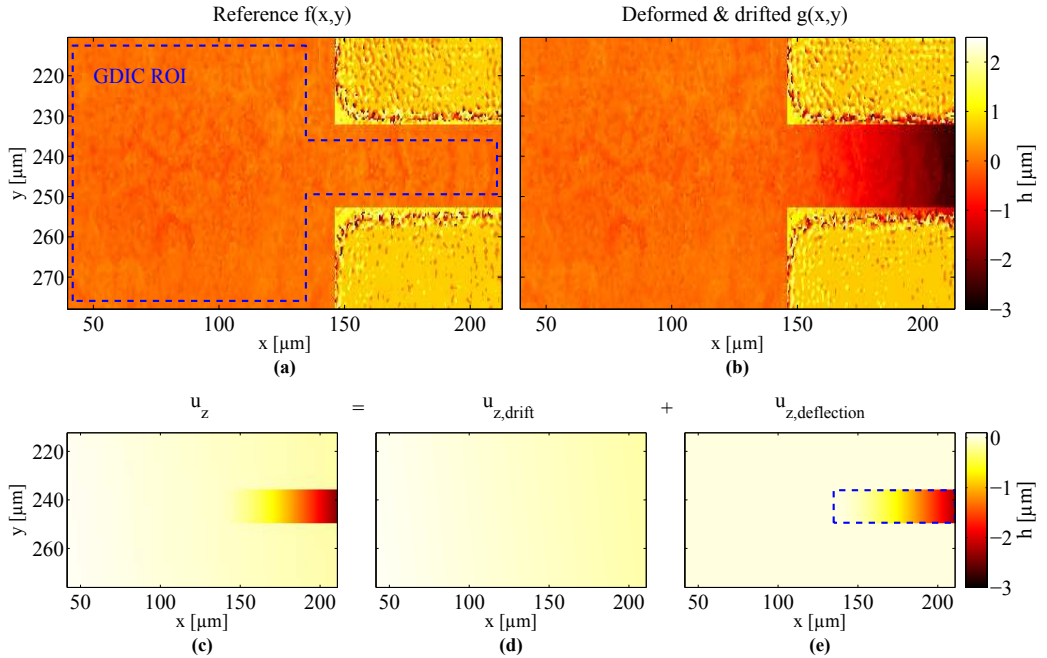


Figure 3.4: GDIC for measuring a drift-corrected deflection profile. (a) Reference profile  $f$ . (b) Deflected and drifted profile  $g$  (c)  $u_z(\vec{x})$  displacement field composed of a (minor) drift component over the entire ROI (d) and a major deflection component of the beam. (e) The region outside the ROI is masked during correlation due to the inconsistent reconstruction by the DHM.

performed a few seconds slower, causing a longer delay in measuring profiles after release. The complete sequence is illustrated for one beam in the inset of Fig.3.5. The DHM measures continuously, where the acquisition period is adjusted between 0.1 s and 20 s to match a logarithmically spaced temporal sampling after release.

The results show that after releasing the cantilevers, first, a large instantaneous change in curvature occurs, see inset Fig.3.5, followed by a slow but significant recovery of the curvature, and in some cases ending with a permanent curvature, see Fig.3.5. The amount of recovery and the final curvature vary from beam to beam as a result of the hold state and the variations in microstructure. The absolute values cannot be observed directly, because a steady curvature is not reached even after  $10^5$  s. Furthermore, the plot reveals a decay over multiple decades, indicating multiple time constants and/or non-linear material behavior. An improved insight into the amount of recovered and permanent deformation, as well as the material parameters is obtained by modeling, see sec.3.4.

The precision of the curvature measurement is estimated from a set of 11 profiles taken before the deformation is applied. This is a difficult case for the GDIC algorithm enhanced with deflection kinematics, because of the near-zero curvature. The standard deviation obtained is  $s_\kappa \leq 1.5 \cdot 10^{-6} \mu\text{m}^{-1}$ . This value is also obtained in a numerical study on the performance of curvature measurements from GDIC, see App.A. This precision is more than sufficient for strain measurements on  $t_{\text{film}} \leq 5 \mu\text{m}$  as it yields  $s_\varepsilon \leq 4 \cdot 10^{-6}$ .

Although other traditional optical full-field curvature techniques used in thin film studies yield precision down to  $s_\kappa = 10^{-9} \mu\text{m}^{-1}$  [56], they prohibit extracting the curvature at such a local and small scale. Furthermore, when comparing to pure 2D DIC surface strain measurements employed in planar test structures, obtaining such a high strain precision would be a true challenge. In 2D DIC a strain precision of  $\sim 1 \cdot 10^{-5}$  is currently the limit, which is only obtained for facets of  $100^2$  pixels in images of  $1024^2$  [83]. At these length scales such 2D DIC precision would require high resolution microscopy and a suitable planar testing setup, e.g. micro tensile tester. Lastly, the high precision in the strain measurement is not only a benefit for analyzing time-dependent mechanics, it is also useful for residual stress measurements or dynamic deformation measurements.

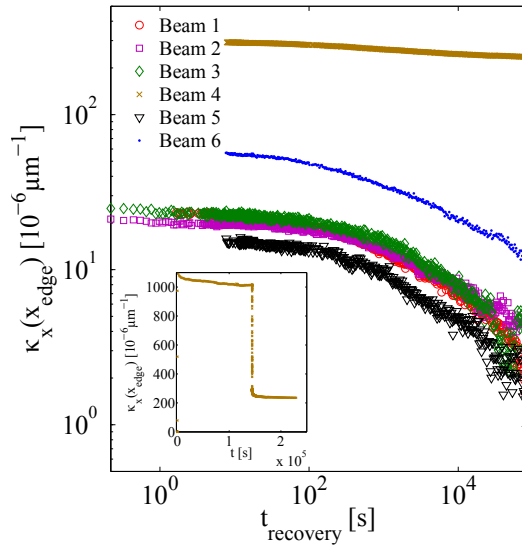


Figure 3.5: Measured curvature evolution after releasing the constant deflection during the hold-down period. The inset shows the curvature evolution as an example for beam 4 during the entire load, hold and release sequence.

### 3.4 Mechanical characterization

The measured curvature evolution can be a combination of instantaneous elastic and plastic deformation and of time-dependent elastic and plastic deformation. This can be described by a simple mechanical model that combines visco-elastic elements with (visco)plastic elements, see Fig. 3.6a. The focus is on time-dependent anelasticity and, therefore, it suffices to assume simple instantaneous plasticity for the characterization of the permanent deformation. Furthermore, as the curvature measurements reveal an exponential decay over multiple decades in time, a multi-mode Maxwell model is employed to extend the number of time-constants. A rule of thumb for such multi-mode models is to use 1 to 2 modes per decade in time resulting in an adequate approximation of the relaxation behavior within experimental error [6]. The moduli  $E_i$  represent the energy storage per mode, the sum of

which gives the instantaneous modulus, i.e. the a-priori known Young's modulus  $E$ . The viscosities  $\eta_i$  represent the dissipative deformation mechanisms. Per mode they yield a time constant  $\tau_i = \eta_i/E_i$ , recognizable from the Prony-series description of visco-elasticity.

In order to obtain model parameters, an identification on the basis of stress-strain data is usually performed. The lack of a force measurement is here circumvented through a stress-free formulation for the anelastic strain,  $\varepsilon_{\text{anel.}}$ , obtained by solving the ordinary differential equations (ODE) for selected boundary conditions imposed in the experimental sequence: first stress relaxation with  $\varepsilon_{\text{anel.}}(t_0 = 0 \leq t \leq t_{\text{hold}}) = \varepsilon_{\text{hold,anel.}}$  followed by reversed creep with  $\sigma_{\text{ext.}}(t > t_{\text{hold}}) = 0$ , see Fig.3.6b. During  $t \leq t_{\text{hold}}$  the ODE is solved to yield the system state upon release. This serves as initial condition for the solution of the ODE for  $t > t_{\text{hold}}$ . The formulation, however, requires the Young's modulus to be a known parameter, which is why an explicit force measurement is not required. A better estimate of  $\varepsilon_{\text{hold,anel.}}$ , the anelastic part of the model during hold period, and the permanent strain  $\varepsilon_{\text{perm.}}$  are obtained by adding the latter as an unknown parameter to be identified. The details of the derivation are given in App.B. From this we obtain the relaxation evolution per damper for the hold period ( $\varepsilon_{\text{hold,anel.}}(t \leq t_{\text{hold}})$ ), which determines the initial state upon release:

$$\varepsilon_{\eta_i} = \varepsilon_{\text{hold,anel.}}(1 - e^{-t_{\text{hold}}/\tau_i}). \quad (3.6)$$

The evolution of the strain after release is then:

$$\varepsilon_{\text{total.}}(t) = \varepsilon_{\text{hold,anel.}} \sum_{i=1}^n \frac{E_i}{E} \left( \sum_{j=1}^n b'_j p_j(i) e^{\lambda_j(t-t_{\text{hold}})} \right) + \varepsilon_{\text{perm.}} \quad (3.7)$$

The parameters  $\lambda_j$  and  $\underline{p}_j = \sum_{i=1}^n p_j(i)$  are the eigenvalues and eigenvectors of the coupled ODE problem and are a function of the material parameters  $E_i, \tau_i$ . Solving for the initial values given by Eq.3.6 yields the parameters  $b'_j$  which are a function of the material parameters  $E_i, \tau_i$  and the applied load duration  $t_{\text{hold}}$ .

The model parameters to be obtained are  $E_i, \eta_i$  and  $\varepsilon_{\text{perm.}}$ . The Young's modulus  $E$  is measured with a different technique, i.e. an eigenfrequency measurement combined with finite element analysis of electrostatically actuated beams [14, 22]. The time constants are fixed per measured decade using logarithmic spacing, so  $\tau_1 = 1.7 \cdot 10^1$ ,  $\tau_2 = 1.5 \cdot 10^2$ ,  $\tau_3 = 1.3 \cdot 10^3$ ,  $\tau_4 = 1.1 \cdot 10^4$ ,  $\tau_5 = 10^5$  s. This implies that either  $E_i$  or  $\eta_i$  are fixed. Here we choose the storage modulus as unknown, thus giving 6 parameters: five  $E_i$  and  $\varepsilon_{\text{perm.}}$ . Using a standard nonlinear minimization procedure the parameters in Eq.3.7 are then identified from the experimental data, which has logarithmic sampling of 100 per decade.

Fig.3.7a shows that a 6-dof approximation is able to correctly follow the anelastic recovery over 5 decades of time. The standard deviation of the difference between the model and measurement is,  $s_{\varepsilon, \text{model}} < 3 \mu\varepsilon$ , which is within experimental precision.

In order to evaluate the material behavior independently of the amplitude of the applied hold level and the permanent deformation, the anelastic part of the recovery is normalized by the total amount of recovered strain  $\varepsilon_{\text{recovered}}$ :

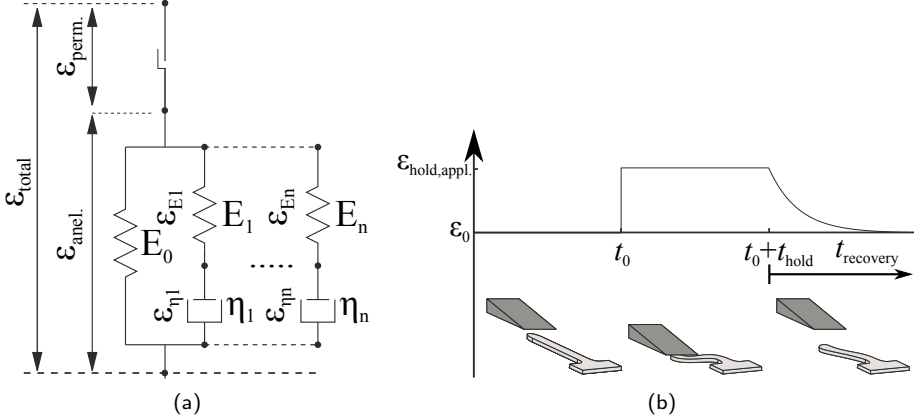


Figure 3.6: (a) Time-dependent behavior described by a standard solid multi-mode viscoelastic model with plastic dissipation resulting in permanent deformation. (b) Deformation controlled loading sequence for microbeam bending experiment without force measurement.

$$\varepsilon_{\text{norm.anel.}}(t) = \frac{\varepsilon_{\text{total}}(t) - \varepsilon_{\text{perm.}}}{\varepsilon_{\text{recovered}}} = \frac{\varepsilon_{\text{total}}(t) - \varepsilon_{\text{perm.}}}{\varepsilon_{\text{total}}(t = t_{\text{hold}}) - \varepsilon_{\text{perm.}}}, \quad (3.8)$$

which is independent of the load level. Indeed, after normalizing the six experiments by their respective values for  $\varepsilon_{\text{recovered}}$ , a master-curve like time-dependent behavior is observed, see Fig.3.7b. When averaging the identified moduli per mode, i.e.  $\bar{E}_i = (\sum_{k=1}^N E_{i,k})/N$

for the  $N$  beams, and applying these to Eq.3.8 to obtain a calibrated master model, the resulting normalized anelastic behavior falls within the experimental error, as indicated by the solid line in Fig.3.7b. This experimental spread is not only due to the measurement precision, but mainly due to the statistical microstructural variations from beam to beam.

The validity of the master model is tested by reloading the measured specimens with different loads and predicting the recovery behavior with the model. To this end, extra experiments are performed on the same beams, but with different hold times, i.e.  $t_{\text{hold}} = 10^2, 10^3, 10^4$  s at hold period load levels similar as discussed earlier. The experimental results for beam 4 during  $t_{\text{hold}} = 10^3$  s have been omitted, because of a failed experiment. The master model predicts  $\varepsilon_{\text{anel.}}(t)$  by optimizing  $\varepsilon_{\text{hold, appl.}}$  and  $\varepsilon_{\text{perm.}}$  to the data at  $t < t_{\text{hold}}$  and  $t \rightarrow \infty$ .

The predictive capability of the time-dependent behavior is evaluated through the resulting normalized behavior, see Fig.3.8. For  $t_{\text{hold}} = 10^2$  s the noise appears large, because the absolute  $\varepsilon_{\text{recovered}}$  is relatively small. The trends are significantly different between the four different hold durations: for increasing hold period  $\varepsilon_{\text{anel.}}$  drops off later, which is also predicted by the model to within experimental error. Furthermore, when plotting the experimental observations for  $\varepsilon_{\text{recovered}}$  as function of the loading conditions, i.e.  $\varepsilon_{\text{hold, anel.}}$  and  $t_{\text{hold}}$ , see Fig. 3.9a, results are within the prediction interval bound by the predictions calculated using  $E_{\text{pred.int.}} = \bar{E}_i \pm s_{\bar{E}_i}$  with  $s_{\bar{E}_i}$  the standard deviation of the mode-averaged modulus. This illustrates the predictive capability for  $\varepsilon_{\text{recovered}}$  as a function of

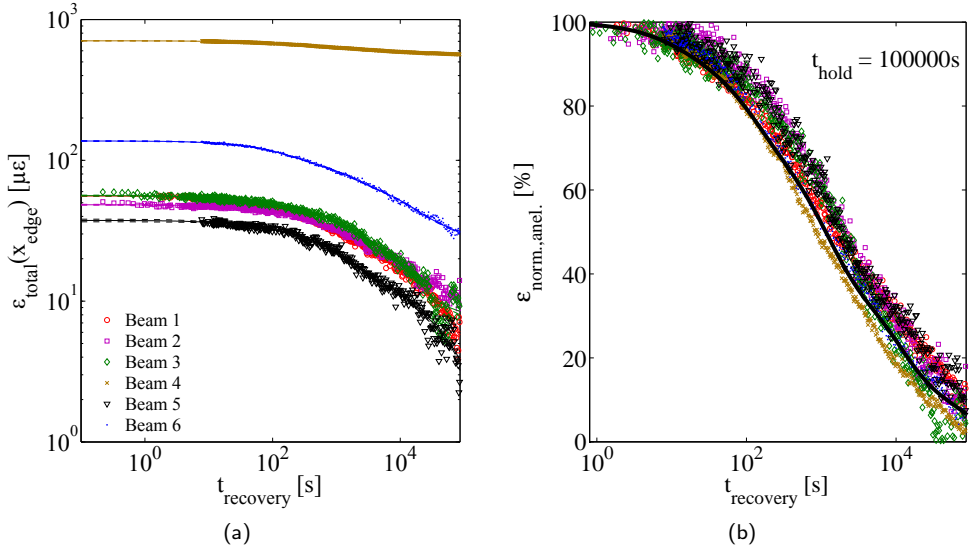


**Figure 3.7:** (a) Strain recovery evolution for the curvature measurements presented in Fig. 3.5 with individual model responses. (b) Normalization of the anelastic part of the recovery evolution shows a master-like curve for the time-dependent behavior for all beams to within experimental error.

the loading conditions. The model not only captures the time-dependent effect, but also the effect on the amount of recovered deformation.

Careful inspection of Fig.3.9a reveals a systematic relation between the individual beams and the prediction: beams 1,2,3 and 5 show lower than average response, whilst 4 and 6 show above average response. This further substantiates the assumption that the beam-to-beam microstructural variations cause the differences in response. It also suggests this methodology is more accurate than expected from the figures.

In addition, the proposed methodology allows characterizing the plasticity in these experiments. When plotting  $\varepsilon_{\text{perm.}}$  as a function of the total strain during hold,  $\varepsilon_{\text{hold,appl.}} = \varepsilon_{\text{hold,anel.}} + \varepsilon_{\text{perm.}}$ , a transition is observed around  $\varepsilon_{\text{hold}} = 1.5 \cdot 10^3 \mu\text{E}$  from complete deformation recovery to plasticity depending on  $\varepsilon_{\text{hold}}$ , see Fig.3.9b. Moreover, the  $t_{\text{hold}}$  does not seem to correlate with  $\varepsilon_{\text{perm.}}$ . This supports the modeling assumption of instantaneous plasticity. Additionally, Fig.3.9b suggests this methodology might be useful for engineering design purposes to gather statistically relevant data to determine the critical strain below which the structure deforms elastically. Further research on the effect of load level, duration, microstructural influences and stress-dependent plasticity modeling might yield a more precise characterization of the plasticity.

Considering the model's capability of predicting the behavior within experimental error for the various microstructures, it appears sufficiently accurate for characterization of materials employed in microdevices. As there is no geometrical factor in the derivation of this model, the obtained parameters can be regarded as material model parameters. However, ultimately the heterogeneity of the microstructure and the role of length scales, possibly involving various interplaying micromechanisms, e.g., dislocation-grain bound-

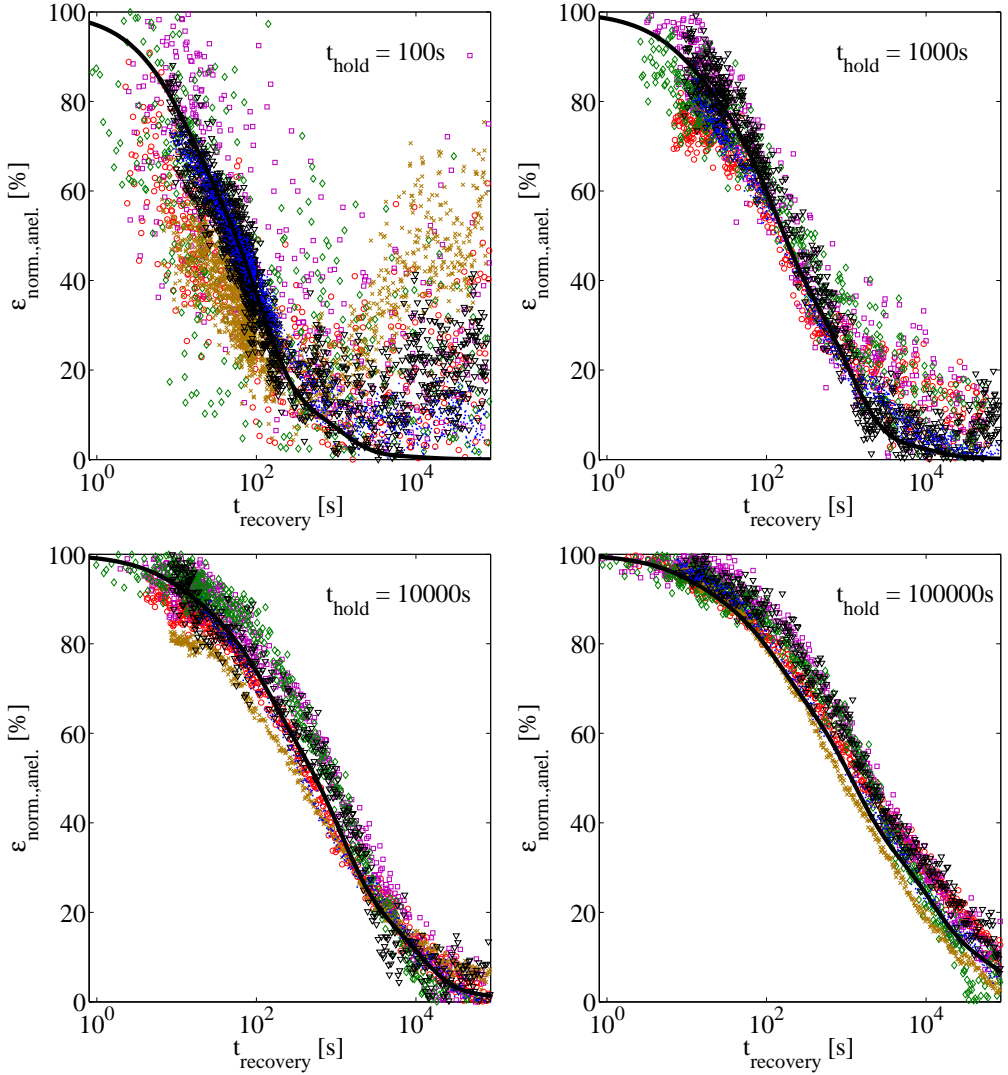


Figure 3.8: Measured (symbols) and master model predictions (line) of the normalized strain recovery evolution for the same cantilevers loaded for various durations show the increase in recovery duration for increasing  $t_{\text{hold}}$ .

ary, dislocation-precipitate interactions, strain-gradients, diffusion effects, require a modeling approach with more resolved details than a simple continuum mechanics approach. Nonetheless, the methodology shows good reproducibility and ease of testing on-wafer structures. It could therefore serve for further studying the microstructural influence on the anelastic and plastic behavior of these materials.

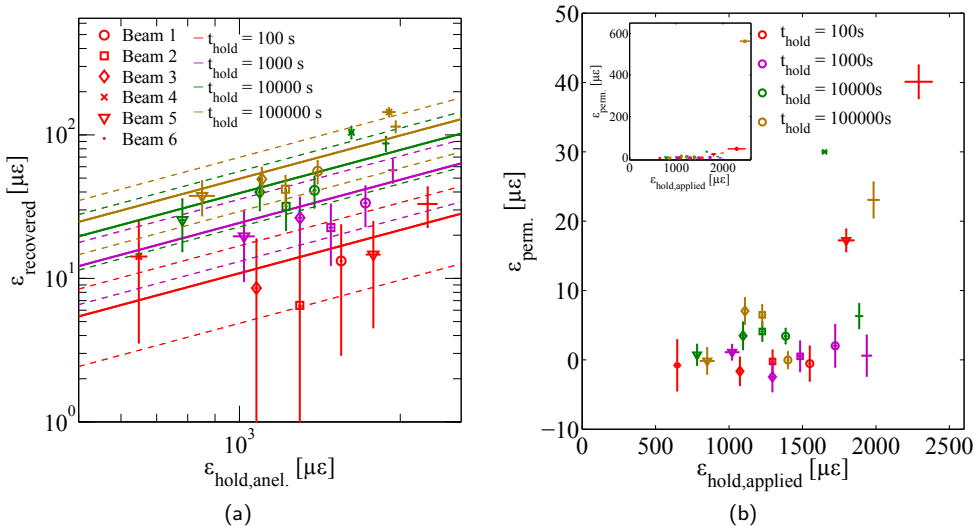


Figure 3.9: (a) Measured (symbols) and predicted (lines) strain recovery amplitudes for the cantilevers loaded for various durations. (b) The permanent deformation  $\epsilon_{\text{perm.}}$  as function of  $\epsilon_{\text{hold,applied}}$  reveals a plasticity threshold.

## 3.5 Conclusion

This methodology utilizes a micro-clamp as a simple mechanical loading device to deflect on-wafer microbeams during several hours with high stability. A dual wavelength digital holographic microscope allows the acquisition of the specimen's height profile during and after loading. In order to successfully extract the height profile from the phase information, an algorithm has been used to remove phase jumps induced by measurement noise related to the relatively large surface roughness common in MEMS. The beam curvature has been extracted from the drift-affected profilometric data by using a novel quasi-3D implementation of GDIC. Experiments of deflected microbeams showed anelastic recovery of the deformation during more than 24 h after complete removal of the applied deflection. The obtained precision in curvature is  $\leq 1.5 \cdot 10^{-6} \mu\text{m}^{-1}$  and in strain  $\leq 4 \mu\epsilon$ . For such a simple setup this performance is notably good.

In order to characterize the anelastic mechanical behavior, a simple model was derived based on multimode linear viscoelasticity and instantaneous plasticity. The experimental sequence combined with the model and the Young's modulus obtained from a different experiment, obviate an explicit force measurement and thus allow for the characterization of the geometry-independent material model parameters. A master model for the anelasticity was successfully calibrated using experiments of long deflection duration. The predictive capability was evaluated by performing experiments on the same beams at three shorter deflection durations and various deflection levels. The normalized anelastic strain evolution of these experiments is adequately described by the master model, illustrating the predictive capability of the time-dependent part. The experimentally measured amplitudes of the recoverable strain also fall within the prediction interval of the master model. Marked experimentally observed differences are related to microstructural differences be-



tween beams. The differences are still within the prediction intervals, further emphasizing the added value of this methodology. In addition to characterization of the anelasticity, the onset of plasticity as a function of loading state was also characterized, which is particularly useful for the design of devices.

In short the proposed simple and precise methodology is useful for MEMS-design and -development, in particular for characterizing the time-dependent anelastic and plastic behavior of thin metallic films.

## **Acknowledgment**

The authors acknowledge dr. Y. Bellouard for discussions about DHM. EPCOS Netherlands B.V. is acknowledged for supplying the specimens.

# Chapter 4

## On-wafer time-dependent nano-tensile testing

---

Reproduced from; L.I.J.C. Bergers, J.P.M. Hoefnagels and M.G.D. Geers, *On-wafer time-dependent nano-tensile testing*, J. Micromech. Microeng., in preparation

### Abstract

Time-dependent mechanical size effect investigations of on-wafer specimens are of interest for improving the reliability of thin metal film microdevices. This chapter presents a novel methodology addressing key challenges in long-duration investigations through on-wafer tensile test achieving highly reproducible force and specimen deformation measurements and loading states. The methodology consists of a novel approach for precise loading using a pin-in-hole gripper and a high-precision specimen alignment system based on 3D image tracking and optical profilometry resulting in near-perfect co-linearity and angular alignment of  $< 0.1$  mrad. A compact test system enables in-situ tensile tests of on-wafer specimens under light and electron microscopy. Precision force measurement over a range of  $0.07 \mu\text{N}$  to  $250 \text{ mN}$  is realized through exchangeable load cells based on a simple drift-compensated elastically hinged load cell with high precision deflection measurement. Three load cells are realized with maximum forces of respectively  $0.25$ ,  $2.5$ ,  $250 \text{ mN}$ , resolutions of  $< 0.005\%$  and reproducibility of  $< 0.04\%$  of the respective maximum force. Specimen deformation measurement, compensated for drift through image tracking of the gauge end with respect to the specimen substrate, yields displacement reproducibility of  $< 6 \text{ nm}$ . Proof of principle tensile experiments are performed on  $5 \mu\text{m}$ -thick aluminum-alloy thin film specimens, demonstrating reproducible Young's modulus measurement of  $72.6 \pm 3.7 \text{ GPa}$ . Room temperature creep experiments show excellent stability of the force measurement and underline the methodology's high reproducibility and suitability for time-dependent nano-tensile testing of on-wafer specimens.

## 4.1 Introduction

There is great interest in the mechanics of thin films, because of their application in a.o. M(O)EMS, N(O)EMS and flexible and stretchable electronics [56, 82, 89, 119, 160]. Considerable research conducted on the characterization of the mechanical properties of various materials has enabled the design and development of new devices and structures. It also increased the understanding of why the mechanics at the micro- and nanoscale differs from that at the macroscale. Size-effects in the elastic response, plastic yield, strength and cyclic fatigue of thin films have received considerable attention [2, 33, 38, 67, 155, 189]. Small scale time-dependent mechanics, such as thin film creep, did not attract much research efforts, perhaps due to its complexity. However, its understanding is a key challenge in material mechanics modeling, which is required for designing reliable micro-devices that are mechanically loaded over long periods of time, e.g. metallic RF-MEMS [78, 170, 173, 181, 185]. Reports on creep [35, 71, 87, 92, 130], time-dependent anelasticity [4, 29, 88, 185] and plastic deformation recovery [149] in thin metal films exist, though systematic studies into accompanying size-effects are rare [33, 70, 85, 112]. From an experimental point of view these studies are highly challenging: not only are high-precision small scale mechanical tests required on a relevant fraction of material, but these tests also require high reproducibility spanning long periods. A highly reproducible experimental methodology designed to enabling in-depth studies of size-effects in time-dependent mechanics, such as plastic creep and anelasticity of thin films, is therefore called for.

A number of review papers have been published summarizing the various micromechanical experimental methodologies developed in the past, their advantages and limitations [63, 77, 81, 103, 145, 160, 163]. Challenges in micromechanical testing include (I) precise loading of the specimens and controlling boundary conditions to ensure a proper quantification of the mechanics, (II) the fabrication and handling of miniature specimens, and (III) measuring the ultra-small applied loads and resulting deformations. With respect to (I), the most frequently adopted loading state, both in the elastic and plastic regime, is the uniaxial stress test. Uniaxial tension or compression testing has comparatively simple loading and boundary conditions, at least at the macroscale, and therefore seem preferable if possible. Regarding challenge (II), IC-fabrication techniques enable easy specimen variations facilitating the processing of the desired microstructure and geometry. A single chip, wafer or other substrate can carry a wide variation of free-standing specimens with geometries spanning the mm to sub- $\mu\text{m}$  range [20, 50, 58, 68, 131, 133, 146, 161]. Additional benefits are the simplified handling of a rigid substrate and the direct applicability of results to actual devices that have been processed in the same way. Finally, concerning challenge (III), the range of dimensions require custom solutions for measuring the involved forces. In this respect, in-situ microscopy not only enables high-resolution deformation measurements, but also enhanced micromechanical analyses.

For this purpose a nano-tensile stage is designed, handling on-wafer specimens for precise small scale uniaxial tensile testing of time-dependent mechanics. The key feature is the highly reproducible control of the loading state for a large variety of specimen geometries. This is realized by a novel pin-in-hole gripping and high-precision alignment system that exploits precision mechanics and innovative 3D image processing of in-situ confocal optical profilometry measurements. Another feature is the reliable force measurement through exchangeable load cells based on elastic hinges, precision electronics and load cell drift

correction. Finally, highly-reproducible deformation measurements are performed using advanced 3D image tracking on in-situ microscopy images of the specimen and its underlying substrate.

Section 4.2 elaborates the core design principles and requirements. Next, the design, realization and performance are discussed for the specimens, the complete tensile stage, alignment control, force and deformation measurement subsystems. Following these sections, proof of principle measurements of the Young's moduli and time-dependent anelastic behavior of Al-Cu thin films are presented to substantiate the methodology's reproducibility.

## 4.2 Design principle

A well controlled loading state is essential for proper testing and analysis. To achieve this, the principle of the design is based on the analysis of the resulting stress state as a function of a possible misalignment of the applied load.

When specimens are fabricated on a substrate, the gripping applies to the free end of the specimen only. To ensure an adequate fixture, grippers combined with (photocurable) adhesives [25], have been proposed, while at the nanoscale electron/ion beam lithography concepts were used [192]. Alternatives are electro-static clamping [169] and mechanical locking via pin-in-hole [152] or gauge-end-conforming geometries [98]. However, in all cases careful provisions for specimen alignment are necessary [95, 96, 101, 104, 110, 113]. Transverse and rotational misalignment between the specimen's longitudinal axis and the setup's loading axis can cause significant bending stresses invalidating the assumed stress and strain state [17, 30, 96, 113, 182], which can lead to premature failure.

The problem of misalignment is illustrated in Fig.4.1, showing a gripper applying a displacement to a tensile specimen (Fig.4.1(a)), which is the case for most tensile test setups (as opposed to applying a force, e.g. in deadweight loading). Misalignment cases are: (i) parallel loading with eccentricity  $\delta$  (Fig.4.1(b)); (ii) in-plane non-parallel loading with rotation angle  $\theta_z$  (Fig.4.1(c)); (iii) out-of-plane non-parallel loading with tilt angle  $\theta_y$  (Fig.4.1(d)). In the ideal case of co-linear loading, see Fig.4.1(e), the applied gripper displacement results in a co-linear reaction force and thus only a uniaxial tensile stress,  $\sigma_{xx,tens.} = F_{axial}/(wt)$  with  $w$  the specimen width and  $t$  the thickness. However, in case of misalignment, see Figs.4.1(f-h), reaction moments and/or transverse forces induce additional bending stresses,  $\sigma_{xx,bend}$ .

To achieve a highly reproducible alignment a simple analysis of the bending to nominal axial stress ratio during misaligned tensile testing is performed similar to Kang and Saif [96]. Here, we define this ratio as a criterium for the misalignment accuracy, see App.C for an analysis of each case. The case of eccentric loading is typically the most critical at this length scale:

$$\frac{\sigma_{xx,bend}}{\sigma_{xx,nom}} = \frac{6\delta}{t_{beam}}. \quad (4.1)$$

This shows for miniature specimens with a typical minimal width and thickness in the

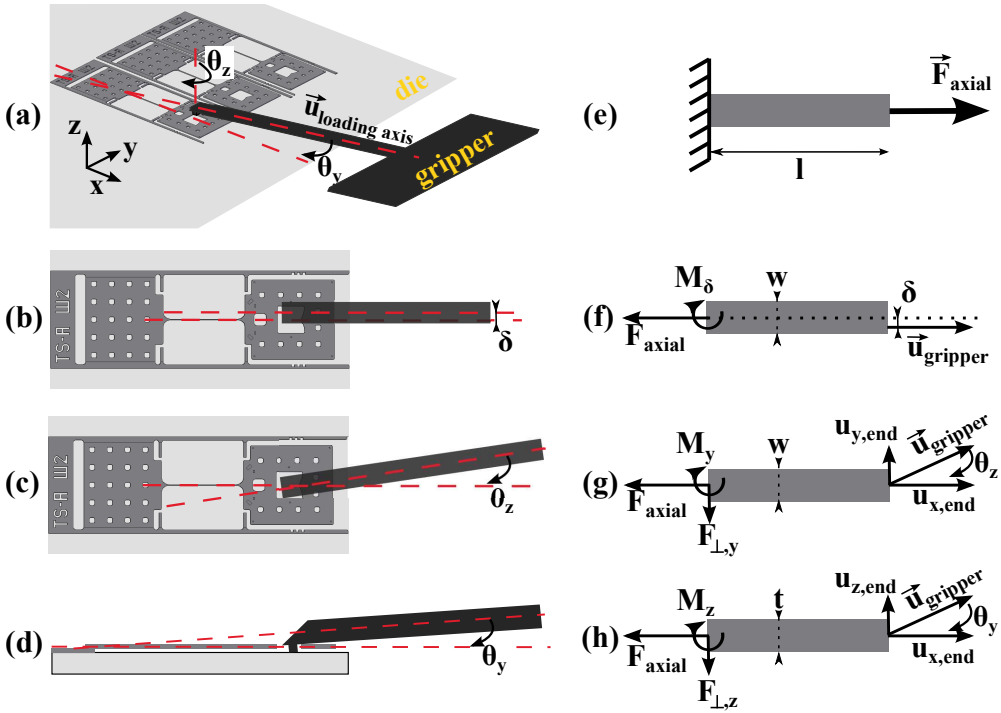


Figure 4.1: (a) Gripper transferring a load at the free-end of an on-wafer tensile specimen that is fixed to the substrate at the other end. (b) Top view of specimen and gripper illustrates parallel axial loading, but with eccentricity  $\delta$ . (c) Top view of specimen and gripper illustrates in-plane misalignment  $\theta_z$ . (d) Cross-sectional view illustrates out-of-plane misalignment  $\theta_y$ . (e) In the ideal case the tensile specimen is loaded axially. (f-h) Free-body diagrams illustrating the case of (f) in-plane eccentric misalignment, (g) in-plane rotation misalignment and (h) the out-of-plane misalignment.

order of  $\sim 1$  resp.  $(0.1) \mu\text{m}$ , that nm-precise positioning (!) of the load is necessary in order to minimize unwanted bending stresses below, e.g., 1% of the axial stress. At the same time, high-precision rotation alignment is necessary.

Various solutions can be considered. In most cases, precision translation and rotation manipulators are employed, whereby it is implicitly assumed that through visualization with SEM / optical microscopy, the alignment can be made adequate. However, reported results typically do not state what precision of alignment is needed and actually attained, with some notable exceptions. In ref.[95] image processing has been employed to measure the rotational misalignment. Adequate alignment can also be established through repeated elastic loading and alignment adjustment until a maximum of the measured modulus is obtained [101]. Alternatives to ameliorate misalignment effects are: the elimination of unwanted kinematic degrees of freedom of the specimen, e.g. through the load frame [75]; addition of compliance at certain locations in the specimen, e.g. see [94]; and the cofabrication of specimen and tester [50, 193].

Here, we introduce an effective solution to the problem of eccentric loading. To ensure that

the load is transferred along the specimen's axis, a square-pinned gripper is inserted into a hole at the specimen's free end, matching a triangle centered on the specimen's axis. This improves the original pin-in-hole gripper proposed in [152] or any other mechanical locking, because only a force and no moment can be transferred at a single point that is well aligned with the specimen axis. Therefore, misalignment effects are reduced to rotational effects only. Rotational misalignment around the specimen's axial direction is further assumed to be negligible due to the pin-in-hole concept and the centered gripping point. However, two rotational misalignments remain: the in-plane rotation  $\theta_z$  and the out-of-plane rotation  $\theta_y$  between specimen's axis and loading axis, i.e. the actuator's axis. For these rotational alignments, novel yet simple image correlation strategies are employed that are based on optical profilometry measurements of the orientation of the loading axis and the specimens longitudinal axis in 3D with sub-mrad precision as discussed below.

### 4.3 Specimen design and fabrication

The tensile specimen geometry is optimized to reduce misalignment and to facilitate deformation measurements, as illustrated by Fig.4.2. One key feature is the load transfer point that ensures precise alignment between the point of load application and the specimen's longitudinal axis even for small positioning errors of the gripper. For this purpose, a hole of 100  $\mu\text{m}$  by 100  $\mu\text{m}$  with a central point on the far edge, aligned to the specimen's loading axis is processed in the plate at the free gauge end. When inserting a square pin into this hole, the surface of the pin transfers the load through this point in line with the specimen's loading axis. Another important design aspect is the placement of rectangular markers at regular intervals on the substrate near conjugate markers on the specimen. They have dimensions of several microns to facilitate observation with optical microscopy. The substrate markers serve to determine the in-plane rotation of the die, which is explained below. Moreover, the conjugate pairs of markers allow for relative displacement tracking in two dimensions of the gauge, from which the global specimen elongation is obtained, corrected for any drift that may occur during long-term testing.

Taking full advantage of lithographic microfabrication techniques, specimens and their geometrical features are processed with lateral precision  $< 150$  nm and variations between 2  $\mu\text{m}$  and 1 mm, see table 4.1. The width variations allow structural size-effect investigations, while long specimens enable high-resolution strain measurements. The specimen thickness depends on the thin film deposition technique and for this work is taken to be nominally 5  $\mu\text{m}$ . The patterning of this specimen layer requires one mask. Intermediate steps are introduced to aid the sequential microfabrication process. To create the free-standing specimens, a sacrificial layer is deposited before the deposition of the final specimen layer and removed by dry etching. This requires 20  $\mu\text{m}$  by 20  $\mu\text{m}$  etch-holes for large areas of the specimen, like the free-ends of the tensile specimens, see Fig.4.2. Furthermore, preventing stiction of such large free-standing areas is necessary to improve specimen yield. Stiction might occur electrostatically during electron imaging, or mechanically due to shape distortions from processing conditions, e.g. through residual stresses. The design prevents electrostatic forces by placing a grounded electrode on the substrate and connecting it to the specimen's layer, see Fig.4.2. To connect the top metal layer to this bottom electrode, part of the sacrificial layer needs to be removed before depositing the top metal layer,

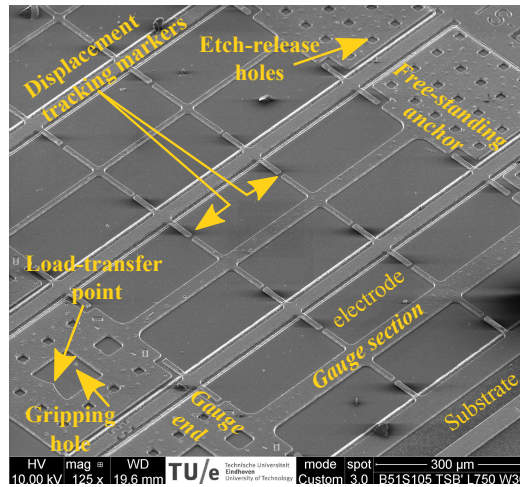


Figure 4.2: Scanning electron micrograph of a free-standing tensile specimen that is fixed at one end along the perimeter of the anchor. At the free-standing gauge-end a gripping hole is made with load-centering feature. Along the substrate and the length of the beam several displacement tracking markers are fabricated to measure the substrate displacement and the gauge deformation.

thus requiring a second mask. Finally, small bumps are incorporated on the bottom of the free-end in order to prevent the sticking of the free-end to the surface. This is achieved by another partial patterning step of the sacrificial layer requiring a third mask. Although in principle other approaches to free-standing structures only require a single specimen-layer mask, this three-mask design offers a robust approach for high-yield mass-fabrication of specimens with considerable geometrical variations.

The specimen wafer is realized in a microfabrication process, see Fig.4.3, that is performed at the processing facilities of Philips Innovation Services, Netherlands. First, an amorphous layer of  $\text{SiO}_2$  is processed by TEOS-deposition on a single crystal Si-wafer, see Fig.4.3(1-2). Then, a blanket layer of aluminum is deposited, which forms a local conducting substrate preventing electrostatic forces between the free-standing specimen structure and the substrate, see (3) in Fig.4.3. The next step is a  $3 \mu\text{m}$  layer of amorphous hydrogenated Si (a-Si:H), which acts as a sacrificial layer, see (4) in Fig.4.3. Next, shallow dimples are patterned in this layer by partially etching away the a-Si:H at the dimple locations, see Fig.4.3(5). Subsequently a thin layer of tungsten (W) is deposited which acts as a diffusion barrier during the Al-alloy deposition, Fig.4.3(6). The sacrificial and W-layer are then patterned and dry etched in one step to yield raised islands, see Fig.4.3(7). The next step, Fig.4.3(8), is the deposition of the top metal layer, being pure Al (99.999%) or Al-1wt%Cu in this study, followed by patterning through dry etching, see Fig.4.3(9). The free-standing structures are thus processed on top of the raised islands, whilst attached to the substrate elsewhere. This top Al-alloy layer also contacts the bottom Al-layer. Furthermore, the dimples are filled by the top Al-alloy layer, thus creating the required bumps underneath the extremities of the free-standing structures. Next, Fig.4.3(10), the sacrificial a-Si:H/W layer is removed with a final dry etch step. Releasing a single die from the wafer is finally done after laser-scribing the wafer-backside, Fig.4.3(11).

Table 4.1: Variations in tensile specimen dimensions.

Dimension	Value [ $\mu\text{m}$ ]
$w_{\text{gauge}}$	2, 3, 4, 5, 7, 10, 30, 50
$l_{\text{gauge}}$	300, 550, 800, 1050

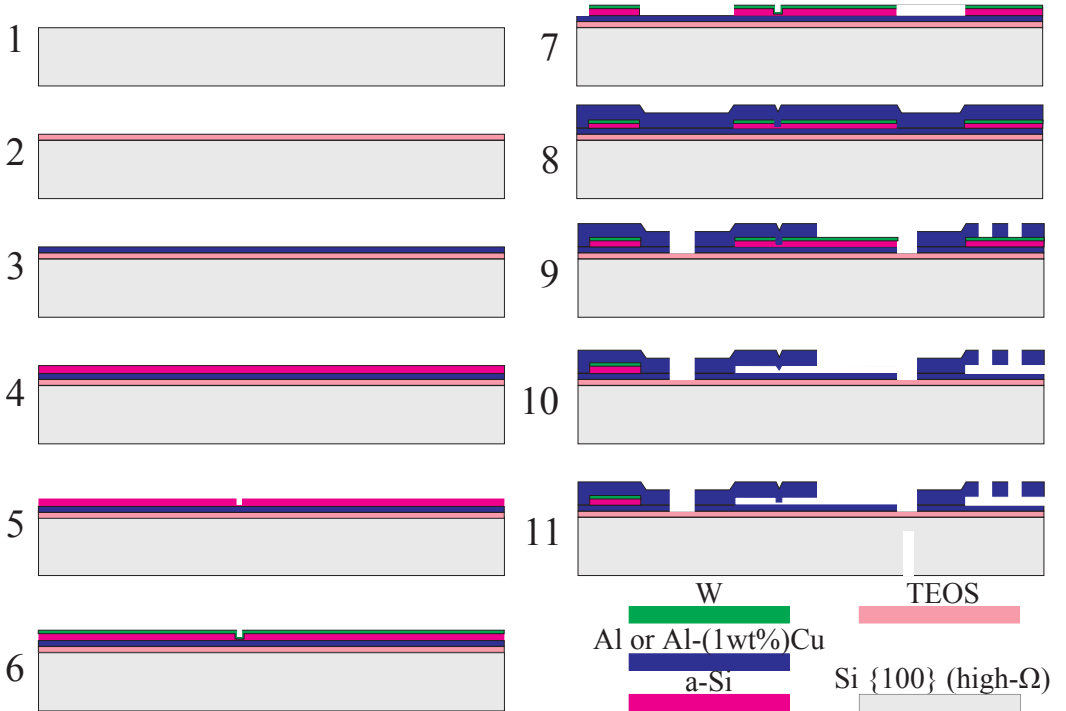


Figure 4.3: Schematic process flow of the specimen wafer microfabrication process. 1) Bare Si wafer. 2)  $\sim 0.5 \mu\text{m}$  TEOS deposition. 3)  $\sim 0.5 \mu\text{m}$  Al deposition (at RT). 4)  $\sim 3 \mu\text{m}$  a-Si deposition (in 3 steps to relax stress build up). 5) Si patterning with timed  $2 \mu\text{m}$  dry-etching. 6)  $\sim 50 \text{ nm}$  W-diffusion barrier deposition. 7) Si+diff. barrier patterning with through-layer dry-etching. 8)  $5 \mu\text{m}$  Al or Al-Cu sputtering ( $350 - 450 \text{ }^\circ\text{C}$ ). 9) Al/Al-Cu patterning by dry-etching, incl. through-etching of bottom Al-layer. 10) Buried a-Si and W-diffusion barrier dry-etching / etch-release. 11) Backside laser scribing followed by cleavage-on-foil.



## 4.4 Nano-tensile stage: design and realization

The design of the tensile stage requires highly reproducible force measurements, displacement measurements and specimen-to-actuator alignment. However, first an overview of the setup design is presented.

### Overall setup design

The tensile tester integrates one module that takes care of the specimen mounting and alignment and one module that takes care of the loading and gripper positioning, which is illustrated conceptually in Fig.4.4 and in detail in Fig.4.5. The basic elements in the first module are the chip mount and two angular manipulators. The second module consists of: coarse manual xyz positioners with mm range and sub-mm precision; an xyz-piezo stage for nm positioning of the gripper that is fixed to the load cell; and a manual rotation manipulator to align the load cell. Specimen loading is performed by the piezo actuator. These two modules are assembled on an electrically actuated tilt mechanism to position both the load cell and chip horizontally with respect to the gravitational field. This is necessary for positioning the load cell horizontally in order to optimize the deflection range for the low-stiffness load cells, see Sec.4.4. The electrical tilt stage enables tilt adjustment in the electron microscope. All electronics are operated and controlled at 50 Hz with a dedicated software application (Labview).

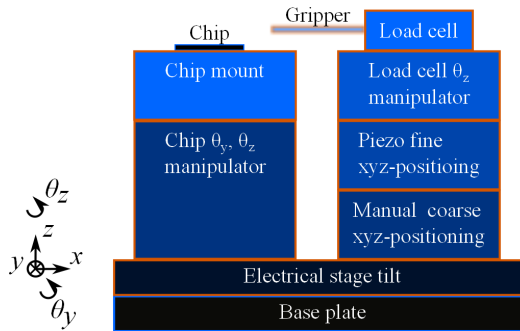
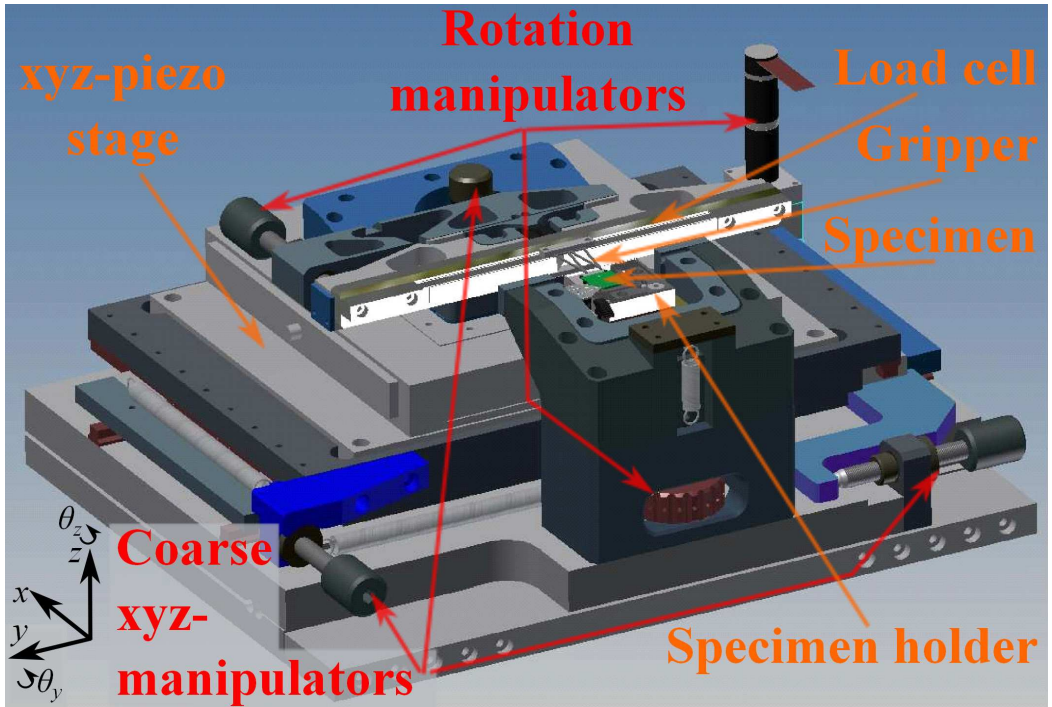
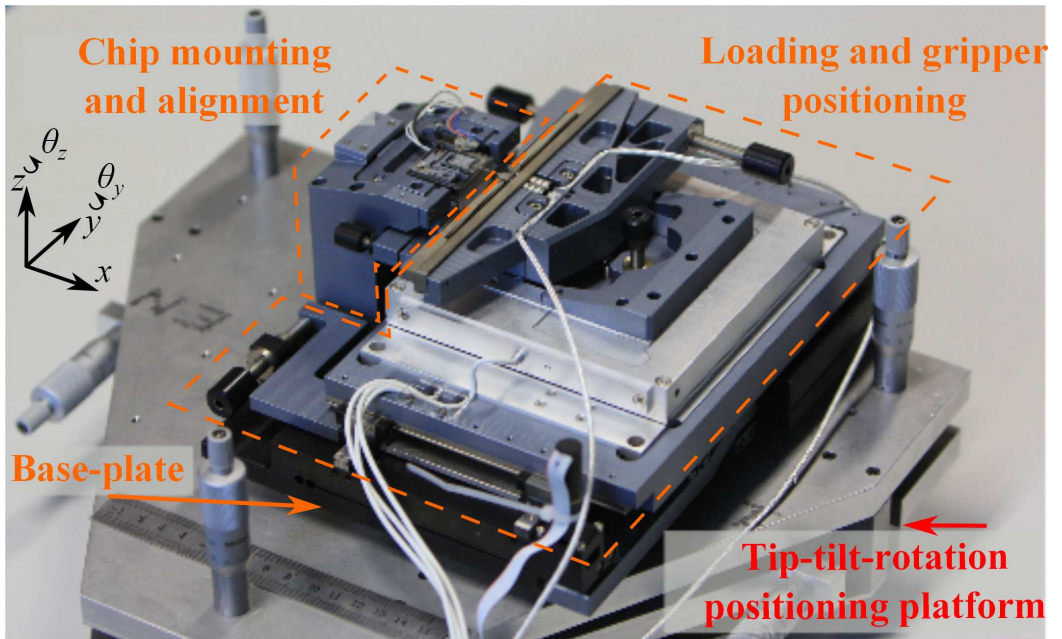


Figure 4.4: Sketch illustrating the main components of the nano-tensile stage.

On the first module, specimens are mounted using an elastic clamping mechanism, see Fig.4.6a. The mount sits on a chip-alignment mechanism containing two elastically hinged mechanisms driven by precision thumbscrews to adjust  $\theta_{y,\text{chip}}$  and  $\theta_{z,\text{chip}}$ . A 3-point probe enables electrical contacting of the chip and grounding of the test specimens. The second module integrates a MadCityLabs T225 xyz-piezo stage for nm-precise positioning of the gripper with respect to the specimen, see Fig.4.6b. For positioning at the mm-scale fine-pitch thumbscrews drive an xy-carriage on precision guides. A separate carriage supporting the load cell and its alignment manipulator is mounted on an elastic parallelogram driven by a third precision thumbscrew for coarse z-positioning. The two modules are placed on a base plate that tilts both modules around the y-axis. An elastic hinge driven by a DC-motor allows tilting with 0.01 mrad steps. The compact design allows the setup to be

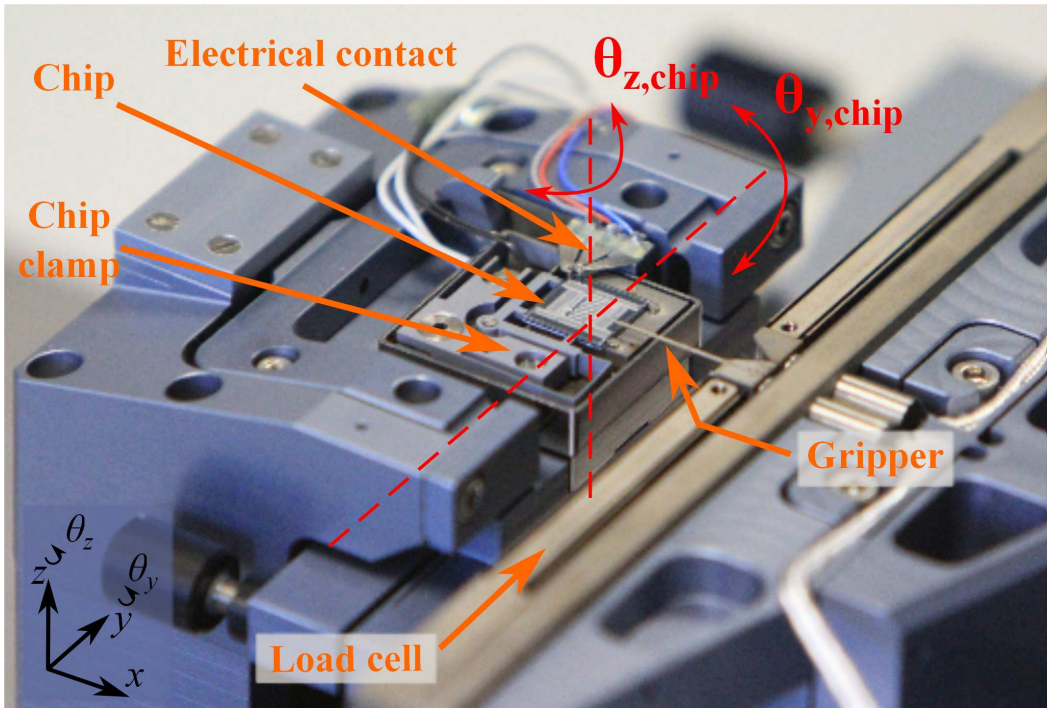


(a)

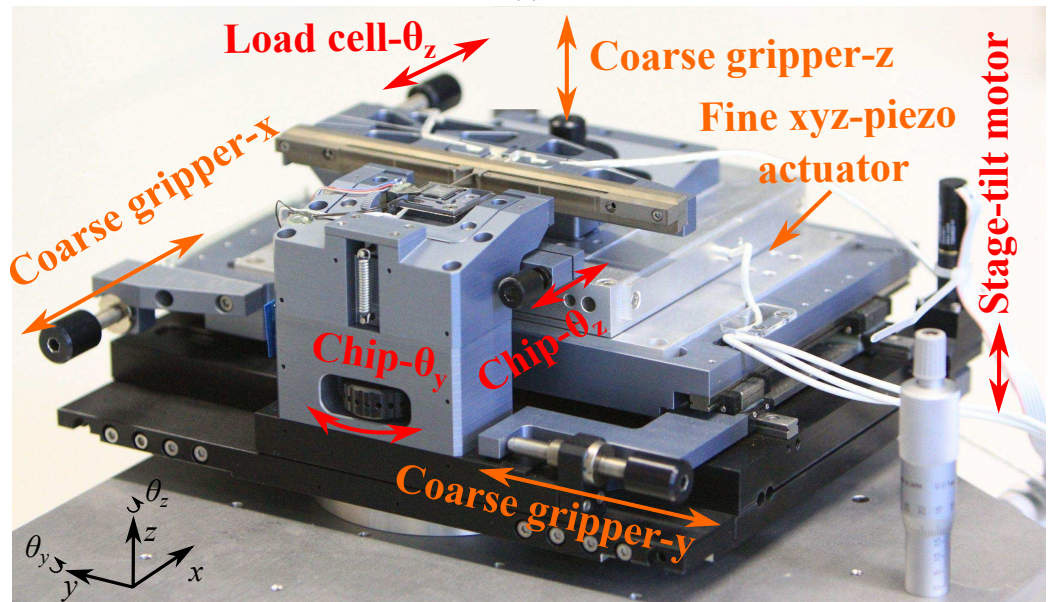


(b)

Figure 4.5: (a) CAD design and (b) photo of the realized nano-tensile stage highlighting the chip mount module, the gripper positioning module, the base plate onto which the modules are built, and a separate tip-tilt-rotation-positioning stage.



(a)



(b)

Figure 4.6: (a) Close-up of the chip mount reflecting the chip, its clamping mechanism, a 3-point electrical probe, the gripper and load cell as well as the tilt and rotation axes of the chip. (b) Overview highlighting manual precision manipulators for angular alignment, coarse xyz-positioning and a xyz-piezo actuator for nm-positioning.

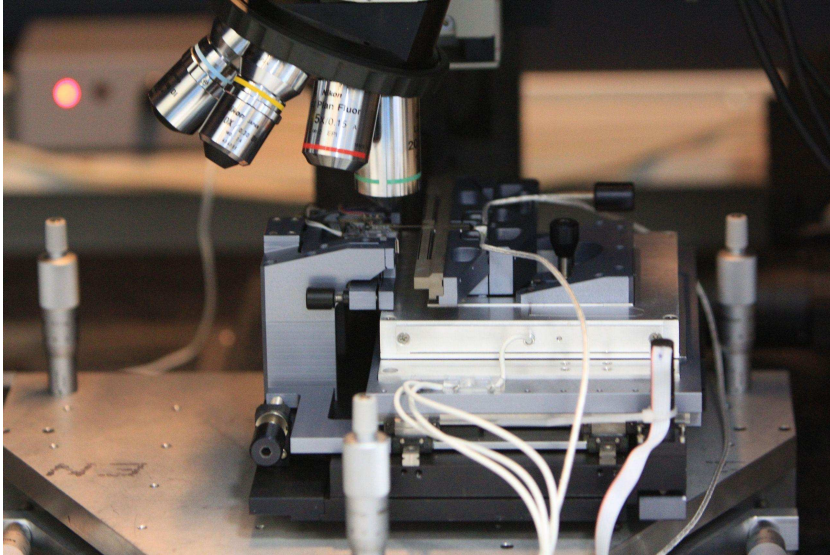
used under a light microscope (LM) and optical profilometer and inside a scanning electron microscope (SEM), see Fig.4.7. Both microscopes are vibration isolated through pneumatic systems. In addition the optical profilometer is placed in a temperature controlled cabinet with  $T = 24 \pm 0.1$  °C.

## Force measurement

The desired geometries dictate the required range and resolution of the force. With cross-sections varying from  $< 0,5 \mu\text{m}^2$  to  $100 \mu\text{m}^2$ , forces range from sub- $\mu\text{N}$ , requiring nN precision, up to 100's of mN. Measuring forces with a single transducer spanning this range, resolution and required reproducibility, is not trivial. This becomes clear from the limited availability of such transducers, which is only applied commercially in nano-indentation equipment [13]. Very sensitive load cells for a more narrow range have been realized by vibrating strings [186] or by (micro)machining simple elastic mechanisms combined with high-resolution microscopy or force sensors, as demonstrated in small scale [106, 115, 151] and fully integrated MEMS based setups [51, 77, 80, 193]. Since each specimen geometry does not require the full force range and minimum resolution, we here adopt a series of elastic-hinge load cells with highly reproducible deflection sensing, each optimized for a certain resolution and range.

Forces are measured through high precision deflection measurements of a monolithic parallel leaf spring mechanism, see Fig.4.8a. For each force range a precision of at least  $10^{-4}$  full scale is desired. A LionSensor precision capacitive sensor (Probe C5-D, driver CPL-190) with a range of  $250 \mu\text{m}$  and resolution of  $9 \text{ nm}$  is employed to measure the leaf spring's deflection,  $u_{\text{LS,I}}$ . This non-contact sensing method does not exert any noticeable force on the leaf spring and attains high precision. The force ranges are determined by the desired minimum precision  $\sigma_F = 10 \text{ nN}$  and maximum force  $F_{\text{max}} = 200 \text{ mN}$ . Matching the required force ranges and precision to the capacitive sensor specifications results in the design specifications listed in Tab.4.2. Since a compact design is mandatory, these mechanisms are produced through wire electrical discharge machining (EDM) of a TiAlV-alloy that has optimal material and manufacturing properties. For load transfer the gripper is shaped as a long beam crossing the chip, see Fig.4.8b. It has a square pin at the end. The other end is a plate that is glued to the load cell. The gripper is produced through wire EDM from a  $0.3 \mu\text{m}$ -thick plate of TiAlV that is polished on one side. Prior to EDM the  $50^3 \mu\text{m}^3$  loading pin is milled that will be inserted into the hole of the free end of the specimen gauge section.

Measurement of such small deflections and forces is susceptible to errors due to thermal expansion and tilt-induced forces that alternate with the low-frequency motion of the vibration isolation frames. To compensate for these errors the load cell contains a second identical leaf-spring mechanism that is not loaded during testing, but senses background forces, see Fig.4.8a. The change in this dummy leaf spring's deflection is therefore solely due to the thermal and tilt fluctuations that are assumed to work on both leaf springs. Assuming that the high precision EDM resulted in identical masses and stiffnesses for both leaf springs, the measured apparent background force of the second dummy leaf spring,  $F_{\text{LS,II}}$  is subtracted from the loaded leaf spring  $F_{\text{LS,I}}$  thus compensating for tilt- and thermal errors.



(a)



(b)

Figure 4.7: (a) Nano-tensile stage on the tip-tilt-rotation positioning platform under a Sensofar Plu2300 optical profilometer. (b) Nano-tensile stage placed in a FEI Quanta 600 ESEM. (Photo courtesy of Bart van Overbeeke Fotografie)

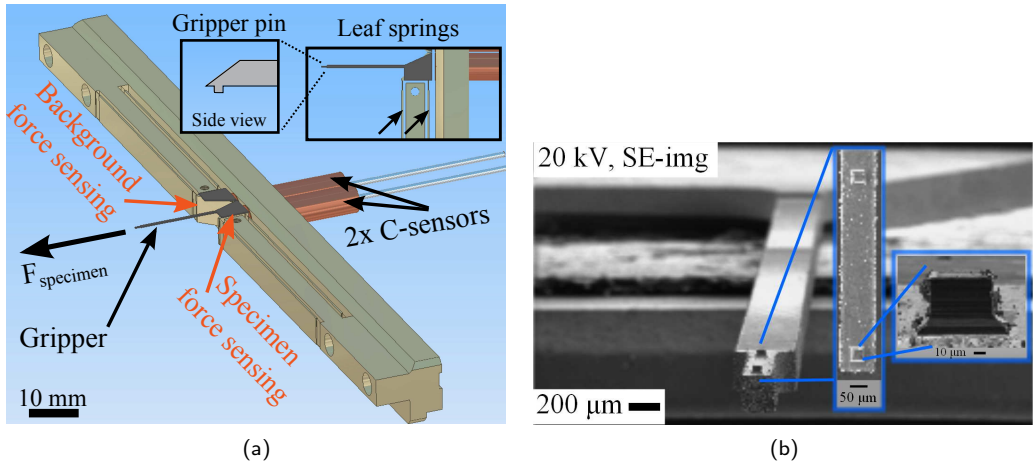


**Figure 4.8:** (a) CAD illustration of the load cell indicating the specimen and background force-sensing parts. Capacitive displacement sensors measure the deflection of leaf springs (right inset) caused by specimen loading. The load is transferred via a small pin on the bottom of the gripper (left inset). (b) SEM image of front-bottom view of gripper highlighting the gripper-end with milled pins of  $50\ \mu\text{m}^3$ .

The calibration of the stiffest load cell is performed with nanoindentation. The two more sensitive ones cannot be calibrated with nanoindentation, because they already deflect to their maximum value when mounted vertically. Indeed, by slightly tilting the load cell from the horizontal plane, gravity causes a deflection. This allows for an alternative, novel calibration method: by measuring the tilt and deflection for various masses placed on the end of the leaf spring, the stiffness can be characterized, see App.D for details. The force-deflection characteristics obtained by calibration yield the stiffness of the load cells, see Fig.4.9(a)-(c) and Tab.4.2. Further, the performance of the force measurement is furthermore specified by its precision and reproducibility. The precision is limited by the noise floor and estimated from the standard deviation of a 10 second sequence of force measurements, see Tab.4.2. Notably, load cell 2 performs slightly better than load cell 1, likely because load cell 1 has a lower eigenfrequency of  $\sim 7\ \text{Hz}$  and is therefore more susceptible to low vibrations. The reproducibility is estimated from a drift characterization by logging the sensor output during 12 h after allowing the system to equilibrate overnight. Figs.4.9(c)-(f) shows that the correction of  $F_{\text{LS,I}}$  by  $F_{\text{LS,II}}$  improves the force measurement by a factor  $\sim 1.5-2$  and hence the reproducibility, which is identified as the slow variations: 200 nN, 100 nN and  $50\ \mu\text{N}$  for respectively load cell 1, 2 and 3. Compared to the load cell range we have  $< 8 \cdot 10^{-4}$ ,  $< 3 \cdot 10^{-5}$  and  $< 2 \cdot 10^{-4}$  full scale. The larger value for load cell 1 again is likely due to differences in stiffness and mass between its leaf springs. Although load cell 1 does not perform completely as intended, the series of load cells provide highly reproducible force measurements for the wide range of specimens, which is essential for time-dependent mechanical characterization.

Table 4.2: Load cell specifications.

Load cell	Range [mN]	Design precision [ $\mu\text{N}$ ]	Design stiffness [N/m]	Realized stiffness [N/m]	Realized precision [ $\mu\text{N}$ ]	Realized reproducibility [ $\mu\text{N}$ ]
1	0-0.250	0.01	1	$1.01 \pm 0.04$	0.08	0.2
2	0-2.5	0.1	10	$13.59 \pm 0.20$	0.07	0.1
3	0-250	10	1000	$1201.45 \pm 0.33$	5.97	50

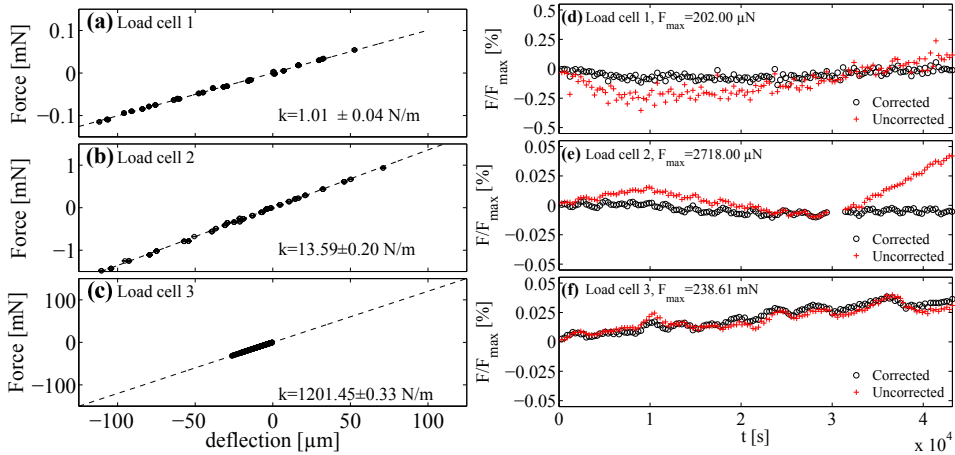


Figure 4.9: (a)-(c) Load cell calibration results per load cell with the measurements (open symbols) and the fitted force-deflection response (dashed line). (d)-(f) Drift characterization of the force measurement per load cell with (O) and without (+) correction using the background measurement.

## Displacement measurement.

In time-dependent anelasticity, small changes in strain of order  $10^{-5} - 10^{-4}$  are of interest over longer periods of time requiring a highly reproducible strain measurement. Strain measurements have been achieved through a diffraction/interferometry technique [188], although it is tedious if not difficult to ensure long term stability for high reproducibility. More promising are full-field imaging techniques combined with digital image correlation yielding deformation fields with sub milli-strain resolution, e.g. local DIC [144, 165] or global/finite element-DIC [12, 84]. However, facets or ROIs of sufficient size and resolution are required for high strain resolutions, which is problematic for specimens of small width. Simple displacement tracking of the gauge end has been done with high resolution displacement measurement techniques e.g. SEM [35], digital image tracking (DIT) of light microscopy images [183] and Fourier analysis of light microscopy images of displaced periodic structures [184]. Digital image tracking can be applied to both SEM and LM images to yield a precision of  $\ll 0.1$  pixel [84]. Additionally, a single image of the substrate and deforming specimen contains relevant information on the drift, which can then be adequately corrected. Therefore, digital image tracking is exploited for high-reproducibility strain measurement.

In order to track the gauge end displacement, in-plane markers are processed along with the test structure, avoiding patterning after fabrication. There are two regions with markers: one besides the specimen on the substrate and the other on the specimen's gauge section, see Fig.4.2. It is assumed that the substrate motion equals the motion of the specimen's fixed end. The motion of the gauge end is tracked separately. Thus the difference between the substrate motion and gauge end motion yields the true gauge end displacement from which the axial strain can be calculated, see fig. 4.10(a). In contrast to Ya'akovovitz et al., who averaged the displacement field obtained from a multi-facet DIC approach [45, 46], here the displacements of one large facet on the substrate and of another on the gauge end are tracked by a DIC algorithm developed for 2D images by Hild and Roux [83]. During long term testing, lighting conditions may change, thereby affecting the DIC performance, which depends on the image brightness and contrast. This can be accounted for in DIC by allowing variations in contrast and brightness of the grey-scale images [165]. In fact, this is only a small extension of a recently developed quasi-3D global DIC code [11, 140]. The degrees of freedom used for the displacement tracking are limited to in-plane rigid body displacements  $u_x, u_y$ . The contrast and brightness are added as an intensity scaling factor,  $\alpha_I$  and an offset  $I_0$  respectively. The exact implementation is straightforward when considering the details by Sutton et al. and the GDIC-basis, which is explained in App.A of the thesis.

Employing GDIC for displacement measurements enables high resolution. Hild and Roux [83] showed that the displacement uncertainty depends on the facet size, with a single facet of  $n = 32^2$  pixels yielding  $\sigma_u < 0.01$  pixel. For the optical setup employed in this study with a 20x objective, a field of view of  $674 \mu\text{m} \times 478 \mu\text{m}$  and a CCD of  $768 \times 576$  pixels, the pixel size is  $0.83 \mu\text{m}$ . Thus, theoretically even with the 20x objective a displacement precision of  $< 8 \text{ nm}$  should be feasible. To analyze the actual performance, the precision  $\sigma_{u,xx}$ , using  $\sim 20$  images captured in 30 s, and the reproducibility  $s_{u,xx}$ , during a 24 hour measurement, are determined from bright field images of an unloaded specimen. These reveal a precision of  $< 5 \text{ nm}$ , see Fig.4.10(b) and  $< 6 \text{ nm}$  for the reproducibility, see



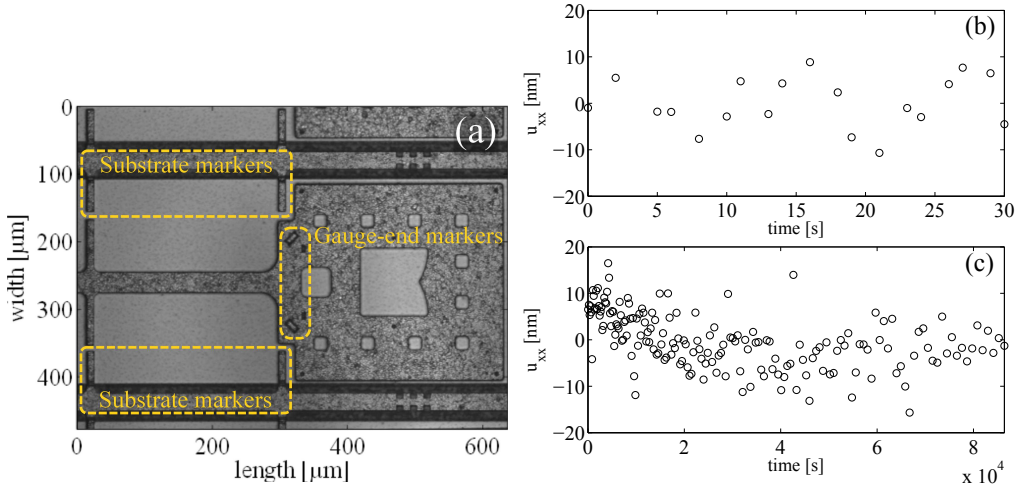


Figure 4.10: (a) The global strain is measured by digital image tracking of the substrate and gauge-end motion. Displacement tracking markers are co-fabricated to allow for robust DIT. Measurement of the x-displacement of the gauge end relative to the substrate reveals excellent precision (b) and stability (c).

Fig.4.10(c). Moreover,  $< 6$  nm reproducibility corresponds to a strains of  $2 \cdot 10^{-5}$  and  $6 \cdot 10^{-6}$  for, respectively, the 300 and 1000  $\mu\text{m}$  long specimens, which meets the target of a highly reproducible displacement measurement system for time-dependent measurements.

## Misalignment control.

The proposed solution for a reliable 3D alignment has been reduced to controlling the tilt  $\theta_y$  and rotation  $\theta_z$  between loading axis and specimen axis. To determine these angles, measurements of the directions of the loading axis and the specimen axis are necessary. Line-direction measurement through Canny-edge detection filtering of 2D images can be used [94], however, it requires two perpendicular imaging systems to determine in- and out-of-plane misalignment. Therefore, here, optical profilometry is employed, which is well suited for measuring the 3D configuration of the chip and the gripper in a limited field of view. From 3D profiles and 2D images these directions can be adequately determined by a novel image processing strategy that combines plane-fitting and (quasi-3D) GDIC applied to full field displacement data [11, 140]. After establishing the misalignment, the rotation manipulators allow for a precise correction. This results in a two step approach for correcting the misalignment.

In the first step, confocal optical profilometry is used to measure the tilt angles of the loading axis,  $\theta_{y,LA}$ , and the specimen's longitudinal axis,  $\theta_{y,SA}$ , with respect to a horizontal datum plane, e.g., the microscope's horizontal plane, see Fig.4.11(a). The difference then gives  $\theta_y$ , which is corrected by manually tilting the chip with a mechanism based on a fine-pitch thumbscrew and an elastic hinge. To measure  $\theta_{y,SA}$ , a surface profile of the die is measured from which the best fitting plane is extracted, described by  $z_{\text{tilted,plane}} = \tan(\theta_y)x + \tan(\theta_x)y + z_0$ , see Fig.4.11(b). It is assumed that, due to microfabrication, the

die is parallel to the specimen, i.e.  $\theta_y = \theta_{y,SA}$ . Hence, the fit yields  $\theta_{y,SA}$ . Using a 50x objective with of 273  $\mu\text{m}$  x 205  $\mu\text{m}$  field of view, surface profiles of the chip surface are obtained with  $\sigma_z < 6$  nm, which is near to the profilometer's z-resolution. Based on this z-precision and the width of the field of view, being  $> 200$   $\mu\text{m}$ , an a priori estimate of the tilt precision is  $\sigma_{\theta_{y,SA}} < 0.03$  mrad. The experimentally obtained precision compares well to this:  $\sigma_{\theta_{y,SA}} < 0.02$  mrad (deduced from repeated measurements).

Next, the angle  $\theta_{y,LA}$  is measured. By moving the gripper along the full range of the loading axis, registering surface profiles of the gripper surface in its extreme positions, and using the quasi-3D GDIC algorithm [11, 140] to extract the 3D displacement vector of a region of interest (ROI),  $\vec{u}_{LA} = u_x\vec{e}_x + u_y\vec{e}_y + u_z\vec{e}_z$ , the loading axis direction is measured and  $\theta_{y,LA} = \text{atan}(u_z/u_x)$  can be calculated, see Fig.4.11(c-d). The natural surface roughness of the gripper serves as pattern for DIC. It is obvious that in order to maximize the precision,  $\sigma_{\theta_{y,LA}}$ , the displacement  $u_x$  needs to be maximized while the precision in  $x$  and  $z$ ,  $\sigma_{u,x}$  and  $\sigma_{u,z}$  need to be minimized. The maximum  $u_x$  corresponds to the actuators maximum displacement, i.e. 200  $\mu\text{m}$ , while the displacement measurement already revealed that image tracking yields  $\sigma_{u,x} < 10$  nm. On the other hand,  $\sigma_{u,z}$  is determined by the height resolution of the profilometry of the gripper surface. Still using the 50x objective, the 200- $\mu\text{m}$  gripper displacement is captured within the same field of view, which is essential for image correlation. This results in  $\sigma_z < 150$  nm for a relatively rough gripper surface ( $R_A = 2.0$   $\mu\text{m}$ ). A priori, a simple error estimate predicts  $\sigma_{\theta_{y,LA}} < 0.75$  mrad. An experimental validation is performed by recording 5 profiles at the maximum  $u_x$ -position that are correlated to the reference at  $u_x = 0$   $\mu\text{m}$ . Taking the standard deviation of the observed  $\theta_{y,LA}$  yields  $\sigma_{\theta_{y,LA}} < 0.1$  mrad. Repeating this sequence results in consistent values for  $\sigma_{\theta_{y,LA}}$ . This value is lower than the a priori estimate, essentially due to statistics through which  $\sigma_{u,z} < \sigma_z$ . The difference  $\theta_{y,LA} - \theta_{y,SA}$  is then corrected with the  $\theta_{y,chip}$  manipulator to within 0.05 mrad, which is validated by remeasuring these angles. Note that at this point the specimen, load cell and loading axis are not necessarily horizontal with respect to the microscope. Therefore, the entire stage is tilted to the horizontal position by either the manual tip-tilt platform or the electrical tilt-actuator to level the load cell and ensure the specimen will be in focus throughout the field of view.

In the second step, the in-plane rotational angles of the loading axis  $\theta_{z,LA}$  and the specimen's longitudinal axis  $\theta_{z,SA}$  are measured with respect to a vertical datum plane, i.e. the profilometer's xz-plane, through bright field images captured with the profilometer, see Fig.4.12(a). The difference of these two angles is  $\theta_z$ , which is corrected by manually rotating the chip about its z-axis with another elastic-hinge mechanism. The chip rotation  $\theta_{z,SA}$  is measured by determining the line-direction of on-chip features, namely the displacement tracking markers on the substrate that are processed with lithographic precision along the specimen's loading direction. Again using GDIC, the line is obtained by matching one set of displacement tracking markers with another in the *same* image, see Fig.4.12(b). It is assumed that the microfabrication is sufficiently precise, to consider line as parallel to the specimen's axis. Hence we obtain the displacement vector  $\vec{u}_{SA} = u_{x,DM}\vec{e}_x + u_{y,DM}\vec{e}_y$ , with  $u_{x,DM}$  and  $u_{y,DM}$  being the distance in the image between two pairs of markers and the angle  $\theta_{z,SA} = \text{atan}(u_{y,DM}/u_{x,DM})$ . An a priori estimate of the precision is obtained from the distance between the markers ( $\Delta u_x = 285$   $\mu\text{m}$ ) and the image tracking precision resulting in  $\sigma_{u,x} = \sigma_{u,y} < 10$  nm and  $\sigma_{\theta,z} < 0.04$  mrad. Experimental assessment of this precision is achieved by determining the standard deviation of  $\theta_{z,SA}$  on five bright field

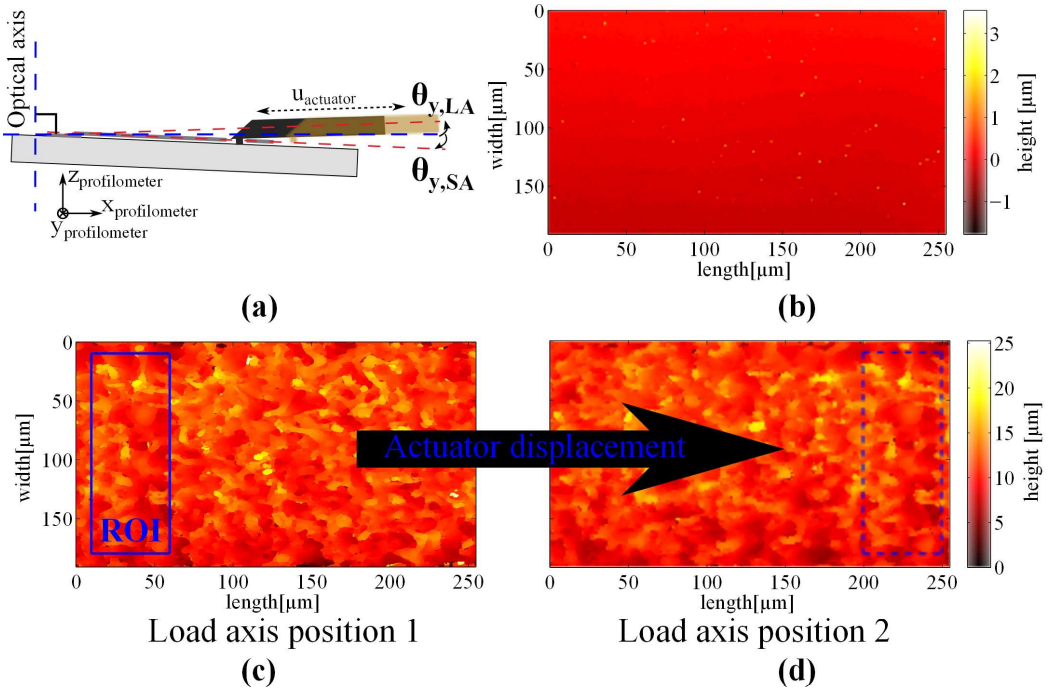


Figure 4.11: (a) Sketch of the measured out-of-plane tilt angles of the loading axis  $\theta_{y,LA}$ , identified by displacing the gripper with the actuator, and specimen axis  $\theta_{y,SA}$ . The angles are defined with respect to a horizontal datum-plane (dashed blue line in x-direction) which is the profilometer's xy-plane. (b) Contour plot of the die surface from which the tilt is obtained by plane-fitting. (c) Contour plot of the gripper surface at one extreme position of the load actuator range showing the region of interest (ROI) tracked with GDIC. (d) Contour plot of the gripper surface after the gripper has been displaced to the other extreme position of the load actuator range.

images acquired with the 20x objective:  $\sigma_{\theta,z,SA} < 0.03$  mrad.

Next,  $\theta_{z,LA}$  is measured in a similar manner as for  $\theta_{y,LA}$ , with the difference that bright field images are recorded with the 20x objective as these suffice for determining the in-plane rotation after aligning  $\theta_y$  in the previous step. Applying the image tracking yields the in-plane displacement of the loading axis  $\vec{u}_{LA} = u_x \vec{e}_x + u_y \vec{e}_y$  from which  $\theta_{z,LA} = \text{atan}(u_y/u_x)$  is calculated, see Fig.4.12(c-d). The estimation of the precision  $\sigma_{\theta,z,LA}$  proceeds similar to that of  $\sigma_{\theta,z,SA}$  and it is validated that also  $\sigma_{\theta,z,LA} < 0.03$  mrad results. After correcting the misalignment to within 0.05 mrad with the chip's  $\theta_z$  manipulator, the correction is remeasured for validation. Finally, the entire tensile stage is rotated in the horizontal plane using the tip-tilt-rotation-translation platform to align the specimen's longitudinal axis to the image x-direction.

The high measurement precision is essentially due to the innovative use of the GDIC algorithm with large facets in (quasi 3D) profiles and images. Besides the good precision, the misalignment setting is highly stable once a chip has been aligned, due to the conceptual design of the entire tensile stage. This was verified by remeasuring the misalignment after repositioning the entire stage under the profilometer after a day. As there are several

specimens next to each other on a chip, no realignment is required when moving the gripper from specimen to specimen. In short, this approach minimizes rotational misalignments significantly without hampering experimental throughput.

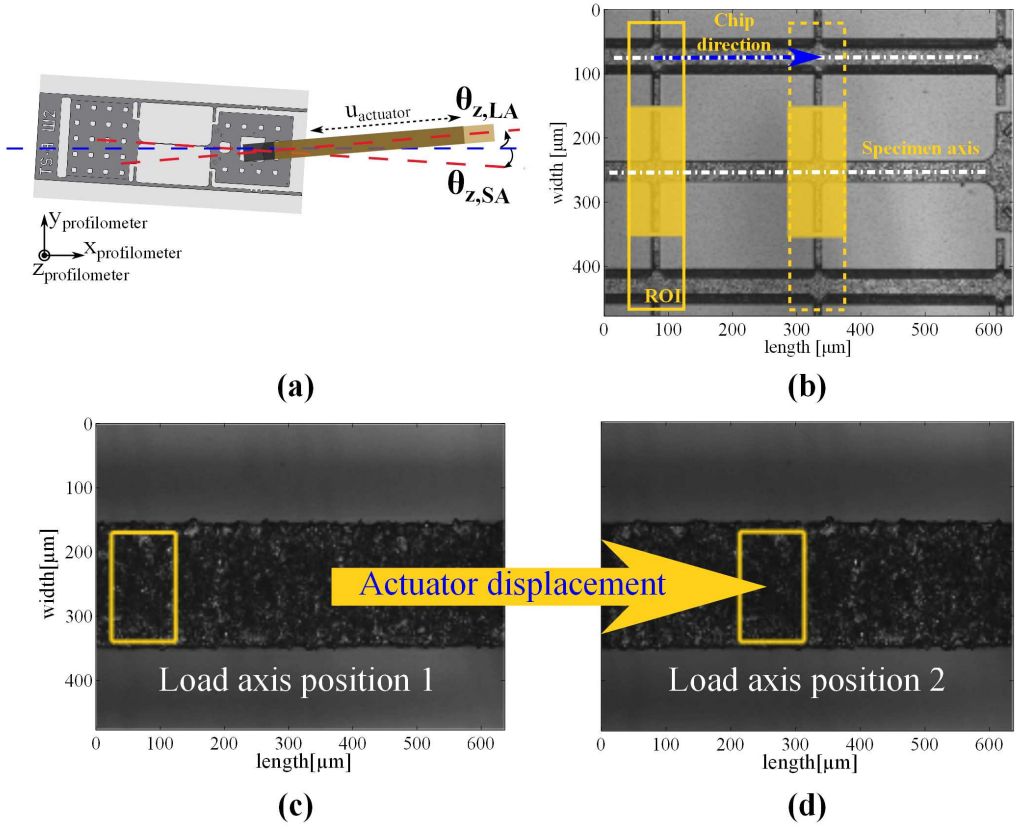


**Figure 4.12:** (a) Sketch of the measured in-plane rotation angles of the loading axis  $\theta_{z,LA}$ , identified by displacing the gripper with the actuator, and specimen axis  $\theta_{z,SA}$ . The angles are defined with respect to a vertical datum-plane (dashed blue line) which is the profilometer's xz-plane. (b) Bright field optical image of the specimen from which the rotation is obtained by identifying the line-direction of the tracking markers using GDIC. (c) Bright field optical image of the gripper surface at one extreme position of the load actuator range showing the region of interest (ROI) tracked with GDIC. (d) Bright field optical image of the gripper surface after gripper has been displaced to the other extreme position of the load actuator range.

## Design summary

The variety of specimen cross-sections requires force measurements with nN precision and ranges up to 100's of mN. Therefore, three exchangeable load cells of different stiffness are built based on monolithic leaf spring designs and high-precision capacitive displacement sensors. A compensation mechanism is incorporated to cope with inevitable mechanical drift. Bright field images obtained with high resolution microscopy are combined with

advanced image tracking of the substrate and the gauge-end to yield drift-insensitive global strain measurements. Several elastic hinges controlled manually by precision thumbscrews enable the alignment of the specimen and the load cell with respect to the loading axis. The alignment occurs under an optical confocal profilometer, which captures 2D bright field images and 3D confocal profiles. Image tracking and plane fitting allows to extract the alignment angles from these images and profiles. These functions are finally incorporated in a compact instrument.

## 4.5 Proof of principle measurements

As a proof of principle, two types of experiments are performed: repeated measurements of the Young's modulus to check accuracy and precision and measurement of the time-dependent anelastic behavior, already observed in microbeam bending experiments, see Ch.2 and 3 [9, 10], and therefore of interest to establish its presence under uniaxial tension.

The Young's modulus is measured from the slope of  $\sigma_{\text{eng}} - \varepsilon_{\text{eng}}$  curves obtained by cyclically loading a tensile specimen with five cycles in the elastic regime. The maximum force in the first cycle is slightly higher than in the subsequent cycles to ensure that subsequent cycles are purely elastic. The force is controlled during these experiments at a rate of  $\sim 45 \mu\text{N/s}$ . This cyclic loading is repeated five times on the same specimen, where it is important to note that the gripper is completely unhooked between the repeated measurements to test the reproducibility of the full measurement including gripper insertion. Multiple specimens are probed with different cross-sections,  $w = 10 \mu\text{m}$  for specimen 1 and 3,  $w = 7 \mu\text{m}$  for specimen 2, and  $l = 1050 \mu\text{m}$ , which are measured with SEM with a precision that is better than 0.1%, relative to the dimension. Forces are measured with load cell 2, with  $\sigma_F = 0.07 \mu\text{N}$ , while deformations are measured by capturing bright field images with the 20x objective at  $\sim 1 \text{ Hz}$ . Fig.4.13(a) shows stress-strain curves for the repeated tests, with an example of the applied cyclic load shown in the inset. The high precision of the methodology entails low noise in the stress and strain measurements. Fig.4.13(b) shows for each load cycle the average with 95% confidence interval of the obtained Young's moduli, which indicate high measurement reproducibility per specimen. Variations/deviations of E-moduli of one specimen are attributed to minor straightening of specimens that were slightly curved due to microfabrication. Variations from specimen to specimen can be attributed to differences in grain texture or slight difference in pre-deformation due to microfabrication. The obtained average modulus  $E = 72.6 \pm 3.7 \text{ GPa}$ , differs within experimental error from reported experimental values [5].

As a second proof of principle measurement, characterization of the time-dependent anelastic behavior is performed on some of the elastically tested specimens. During the first loading stage the force is controlled at a constant force level of  $1575 \mu\text{N}$  to perform a creep test during  $10^5 \text{ s}$ . Subsequently the load is released and the deformation is traced during the next  $10^5 \text{ s}$ , similar to the microbeam bending experiment used to study time-dependent anelasticity in microbeam bending. Images are acquired at logarithmically spaced intervals, see Fig.4.14(a). Force loading and unloading takes several seconds due to the limited PID-controller bandwidth of the setup, see inset Fig.4.14(a). The low noise in stress during the creep stage again reflects the high force reproducibility. The strain measurement reveals a standard deviation of  $\sigma_{\varepsilon,xx} < 6 \mu\varepsilon$ , which corresponds to the value obtained during

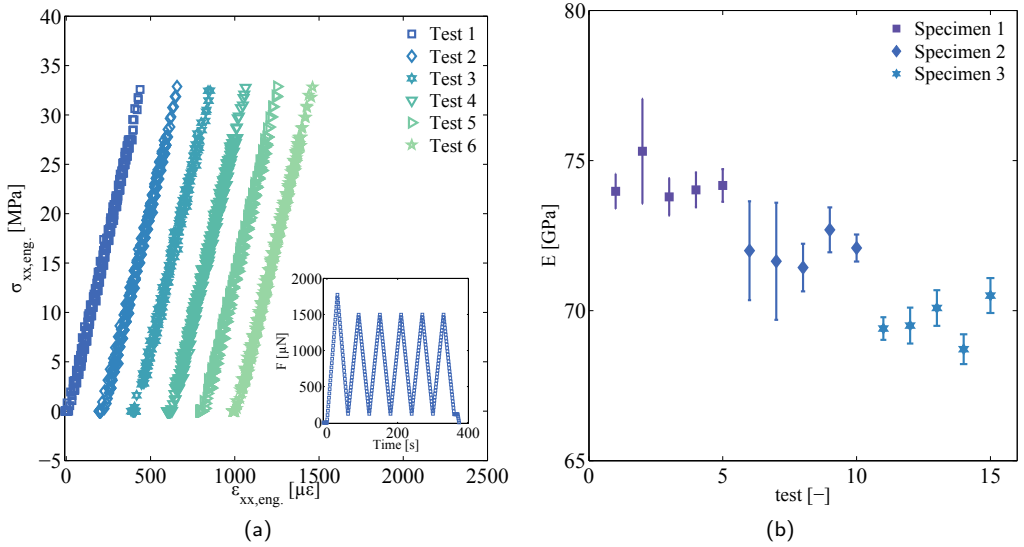


**Figure 4.13:** (a) Cyclic loading experiments, of which the loading pattern versus time is shown in the inset, are repeated on a single specimen to extract the Young's modulus. Each repetition is offset by  $2 \cdot 10^{-4} \mu\epsilon$  for clarity. (b) The measurement of the Young's modulus is well reproducible to within the confidence interval.

validation. The creep experiment shows a typical  $\log(t)$  dependence (Fig.4.14(b)), while the subsequent time-dependent anelastic stage also shows this dependence (Fig.4.14(c)). Even though the stress remains well below the elastic limit, a significant amount of creep occurs at room temperature:  $\sim 10\%$  of the initial strain for the applied load. Moreover, the subsequent time-dependent anelasticity almost completely recovers all deformation up to  $\sim 10 \mu\epsilon$ . The nature of this mechanism is the main topic of Chapter 6.

## 4.6 Conclusion

A novel highly reproducible nano-tensile tester for on-wafer time-dependent testing has been developed. Key achievements are (I) precise loading of the specimens and controlled boundary conditions to ensure a controlled stress state, (II) the fabrication and handling of micron-sized tensile specimens, and (III) measuring the nano-sized applied loads and deformations over long periods of time.

From an analysis of the desired uniaxial tensile loading state, design principles and specifications were derived. To minimize undesired bending stresses, a pin-in-hole gripper load system, which minimized eccentric loading, was implemented together with advanced image correlation algorithms that measured the angular misalignments between specimen and loading axis to within 0.1 mrad. Chips with a large amount of specimens and geometrical variations were realized through MEMS microfabrication. Key features were integrated into the specimens to enable the high reproducibility of strain measurement and rotational alignment, by microscopically visible displacement tracking markers. The precision design

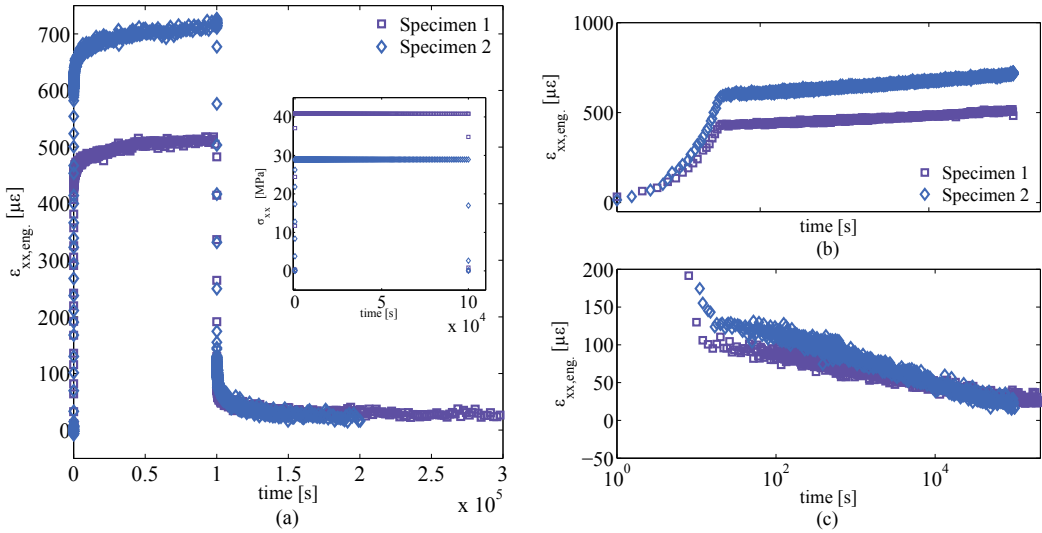


Figure 4.14: (a) Tensile creep experiment at constant stress (see inset) followed by time dependent anelasticity recorded for a tensile specimen. (b) The creep stage shows a typical  $\log(t)$  dependence, while in (c) the time-dependent anelastic recovery phase also reveals a  $\log(t)$  dependence.

and verification of the setup components showed that the aimed high reproducibility of the loading, force and deformation measurement was effectively obtained. Three load cells with a drift compensation mechanism achieved a force range from 70 nN to 200 mN with a reproducibility exceeding 0.1% full scale of the respective load cell. The displacement measurement was performed by image tracking of the substrate markers and specimen gauge markers, yielding  $\sigma_{u,x} < 6$  nm, and  $\sigma_{\epsilon,xx} < 6$   $\mu\epsilon$  for the tested specimens. Proof of principle measurements illustrated the high reproducibility and precision of this nano-tensile tester. Measurement of the Young's modulus of 5- $\mu\text{m}$  thick Al-(1wt%)Cu tensile specimens resulted in a value of  $E = 72.6 \pm 3.7$  GPa. Time-dependent anelasticity measurements were performed during 56 hours on these specimens confirming the high strain reproducibility  $\sigma''_{\epsilon,xx} < 6$   $\mu\epsilon$ . These micron-scaled experiments revealed a pronounced creep stage, followed by an unexpected near-complete recovery of the creep deformation. It is expected that this on-wafer nano-tensile testing methodology combined with the large amount of specimen variations enables systematic studies into time-dependent anelasticity of thin metal films.

## Acknowledgment

The authors acknowledge ir. E.C.A. Dekkers, ir. R.J.L.J de Regt and P. Minten of the Engineering and Prototyping Center and S. Garenfeld and P.W.C. van Hoof of the Dept. of Mech. Eng. of the Eindhoven University of Technology for collaborating on the design and realization of the nano-tensile stage. Furthermore, the authors acknowledge the aid of dr.ir. M.A.J. van Gils, and ir. A. den Dekker of EPCOS Netherlands BV and dr.ir. E. van den Heuvel and ing. E. Alexander-Moonen of Philips Innovations Services during the design and fabrication of the specimen wafers.

## Chapter 5

# Some observations on $\theta$ precipitation in Al-(1wt%)Cu thin films

Reproduced from; L.I.J.C. Bergers, J.P.M. Hoefnagels, J.Th.M. de Hosson and M.G.D. Geers, *Some observations on  $\theta$  precipitation in Al-(1wt%)Cu thin films*, in preparation

### Abstract

The precipitation state of Al-(1wt%)Cu thin films influences the mechanical strength and creep. To establish an optimal strength of Al-(1wt%)Cu thin films through precipitation strengthening, nano-indentation hardness measurements were performed on Al-(1wt%)Cu thin films solution treated at 550 °C for 15 min and aged at 190 °C. These revealed an unexpected decrease in hardness at  $\sim 8$  hours, followed by a saturating increase for aging durations  $< 48$  hours. A detailed microstructural analysis was performed with HRTEM, WAXD, SEM and EDS. HRTEM analysis of thin films as-received from microfabrication processing revealed that GP zones and  $\theta$  precipitates were present, while  $\theta'$  could not be observed. Specimens were then subjected to homogenization and aging for 0, 6, 8, 10 and 24 hours. WAXD confirmed the presence of  $\theta$  precipitates for aging durations longer than 8 hours, which is sooner than bulk-alloy precipitation, while indicating that  $\theta'$  was not present. Through-thickness measurements using BSE and EDS of aged specimens highlighted that  $\theta$  precipitates, nucleate and grow essentially at grain boundary grooves, though also at the specimen surface, while depleting Cu from the grain interior. To explain the absence of  $\theta'$  and the fast nucleation of  $\theta$ , it is hypothesized that  $\theta$  precipitation is favored, because energetically favorable grain boundary grooves act as preferred nucleation sites. Finally, it is hypothesized that the growing precipitation at the surface and grain boundary grooves depletes the Cu in the thin film interior while lightly strengthening the surface, thus explaining the weakeningstrengthening sequence observed in the hardness measurements.



## 5.1 Introduction

The aluminum-copper alloy (Al-Cu) system, with copper as the solute element, is well known for its mechanical performance resulting from different metastable and stable  $\text{Al}_x\text{Cu}_y$  precipitates that can co-exist, depending on composition and thermal history. This was already discovered in the early 1900s by the German metallurgist Alfred Wilm [86], who observed that, at room temperature, quenched Al-(4wt%)Cu hardens over a period of several days due to precipitation. By optimizing the heat treatment, efficient combinations of light weight and high strength properties are achievable. The Al-Cu alloy was therefore one of the first aluminum alloy systems to be employed in aerospace structures, such as the Wright flyers crank case [61] and later with its prime application in rigid airship frames in the 1920s and 1930s.

The precipitation process is now well understood, at least for engineering applications of bulk Al-Cu [72, 136, 147]. The solubility of copper is only 0.1wt% at room temperature, see Fig. 5.1(a). A copper concentration above the solubility limit is metastable, in which case the copper will cluster and eventually form stable  $\text{Al}_2\text{Cu}$  precipitates, i.e. the so-called  $\theta$  phase. Despite the low Gibbs free energy of  $\theta$ , its formation rate is very slow at low temperatures due to its high interface energy, because the  $\theta$  crystal structure is incoherent with FCC aluminum. Consequently, the formation of  $\theta$  is often preceded by other smaller, metastable Al-Cu clusters with higher Gibbs free energy but a lower interface energy: (I) nucleation in the matrix of nano-meter sized coherent Guinier-Preston zones, GP1 and GP2, which are ordered, solute-rich clusters of atoms; (II) formation of the much larger semi-coherent  $\theta'$  precipitates mainly at GP zones or dislocations. The effect of this sequential precipitation mechanism on the Al-Cu material strength is shown in Fig.5.1(b), depicting the hardness as a function of aging time, for a range of copper concentrations. For the considered aging temperature, an optimum in hardness, referred to as the peak-aged condition, is found between  $\sim 1$  and  $\sim 10$  days depending on the copper concentration. The presence of this peak is attributed to the prevalence of finely dispersed  $\theta'$  precipitates, whereas upon further aging weaker  $\theta$  precipitates precipitate from/at  $\theta'$ , grain boundaries and interfaces and grow at the expense of  $\theta'$  resulting in a decrease of hardness [72].

In contrast to bulk metallic alloys, the precipitation process in thin films and Al-Cu thin films in particular, has been studied to a lesser extent. There is evidence that  $\theta$  precipitation occurs much faster in thin films [116]. This is of interest, because pure Al-Cu thin films are applied in conducting wires in micro-electronics and mechanical structures in metallic micro-electro-mechanical systems (MEMS). This combines the desired electrical characteristics of Al, with the required resistance against electro-migration and creep [41, 42]. Recently, it was shown in [9] that pure Al-(1wt%)Cu thin films, processed in a MEMS fabrication line, exhibit a significant time-dependent anelastic deformation recovery after unloading over a period of days, see Fig. 5.1(c). It has been hypothesized that this behavior is related to the precipitation state [47].

Therefore, as a first preliminary experiment to determine at which aging times a significant change in precipitation state occurs, the hardness as a function of aging time was measured for the above-mentioned MEMS-processed Al-(1wt%)Cu thin films, by applying the same heat treatment as used for Fig. 5.1(b). The measurement procedure is discussed in Sec. 5.3 however, the results are already displayed in Fig. 1(d). Surprisingly, a decrease in

hardness is observed instead of a peak, and this occurred already at 8 hours instead of  $\sim 10$  days as would be expected for bulk Al-(1wt%)Cu based on Fig. 5.1(b). Whereas this early transition in hardness agrees with the above-mentioned faster precipitation in thin films, the fact that the hardness decreases rather than increases is not easily explained, triggering further analysis in the thin-film  $\text{Al}_x\text{Cu}_y$  precipitation mechanism. For this purpose, this chapter presents a detailed investigation of the  $\text{Al}_x\text{Cu}_y$  precipitation process in Al-(1wt%)Cu thin films. This material system can be regarded as a model system for precipitation in thin-film (aluminum) alloys in general, because (i) its bulk counterpart is fairly well understood, and (ii) pure Al-Cu is relatively simple compared to typical engineering (aluminum) alloys, which can contain a much larger variety of (semi-)coherent and incoherent precipitates. Therefore, the strategy is as follows. First, the precipitation state of the as-received Al-(1wt%)Cu thin films exhibiting the time-dependent anelastic recovery is characterized. Subsequently, the heat treatment is discussed in view of its influence on the hardness measurement, such as a change in grain size causing the reduction in hardness. After identifying the precipitation state as the cause of the hardness decrease, different analysis techniques are employed to unravel the micro-structural origin of this phenomenon.

## 5.2 Characterization of as-received Al-(1wt%)Cu

The micro-fabrication processing scheme to make chips with the MEMS structures, of which a cantilever beam example is shown in Fig. 5.1(c), includes a number of sequential patterning, deposition and etching steps on silicon wafers, similar to those discussed in chapter 4. For the present investigation, the following processing steps are important: (i) the plasma sputter deposition of pure Al-(1wt%)Cu to a thickness of  $5\ \mu\text{m}$  at a substrate temperature of  $450\ \text{°C}$ , followed by an unforced cool-down to room temperature in air; (ii) after the Al-Cu deposition process, several deposition, wet etch and photolithography processes were performed to structure the free standing thin film. Temperatures varied between  $50\ \text{°C}$  and  $400\ \text{°C}$  in a time span of several minutes to an hour depending on the process. This last process step exposed the structures to temperatures of  $50\text{-}60\ \text{°C}$  for  $10\text{'s}$  of minutes. This  $5\ \mu\text{m}$ -thick Al-(1wt%)Cu free-standing film is next referred to as the as-received film.

A free-standing structure of the as-received film was analyzed by high-resolution transmission electron microscopy (HRTEM). Careful specimen preparation was achieved by subsequent ultrasonic cutting, polishing, dimpling, and precision ion polishing at  $4\ \text{kV}$  (PIPS system of Gatan). The latter did not generate amorphous aluminum regions due to Ga-ions implantation, in contrast to focused ion beam milling. Subsequent high resolution imaging and electron diffraction analysis was performed with a JEM 2010F microscope ( $E_{\text{beam}} = 200\ \text{kV}$ ), combined with energy-dispersive X-ray spectroscopy (EDS;  $127\ \text{eV}$  resolution, Bruker EDS system).

First, an EDS analysis of the aluminum matrix was performed (not shown). All peaks could be identified and correspond to Al or Cu, yielding concentrations of  $(99.80 \pm 0.01)\text{wt}\%$  and  $(0.20 \pm 0.01)\text{wt}\%$  for Al and Cu respectively. However, the copper concentration is much lower than the average concentration of  $1\text{wt}\%$  in the Al-Cu thin films. This indicates that most of the copper has migrated out of the probed region, e.g., to the top or bottom

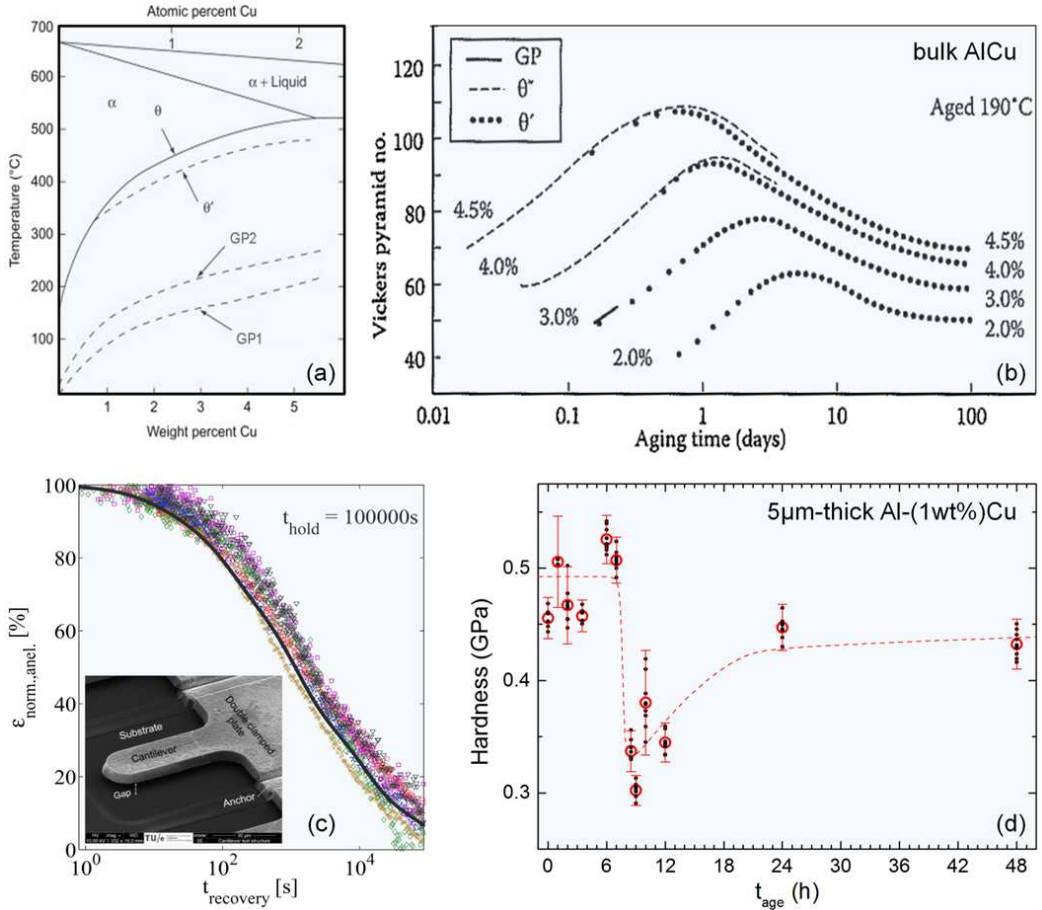


Figure 5.1: (a) (partial) equilibrium phase diagram of Al-Cu, where the solvus lines of GP1, GP2, and  $\theta'$  (dashed lines) and  $\theta$  (solid line) denote the upper temperature limit of stability of the respective precipitate (figure is reproduced from [147]). (b) Hardness measurements of bulk aluminum with different copper weight fractions, after homogenization at 550 °C and aging at 190 °C, showing a peak in hardness between  $\sim 1$  and  $\sim 10$  days depending on the copper fraction (figure is reproduced from [147]). (c) 5µm-thick Al-(1wt%)Cu cantilever beams, shown in the inset of (c), exhibit a significant time-dependent anelastic recovery over a period of  $\sim 1$  day, after a pro-longer period of sustained cantilever beam deflection. This recovery is depicted for several beams by the normalized anelastic strain,  $\epsilon_{\text{norm.,anel.}}$ , as a function of the time,  $t_{\text{recovery}}$ , after load release, see chapter 3 for details. (d) Nano-indentation hardness measurement as a function of aging time for the Al-(1wt%)Cu thin film of figure (c) after the same heat treatment as used for figure (b). The measurements show a decrease in the hardness instead of a peak, already at 8 hours instead of days.

surface of the free-standing structure or its grain boundaries. Next, overview images of the aluminum matrix were made in bright and dark field TEM, together with diffraction patterns from the Al[111], Al $\bar{1}$ 12] and Al[011] zones. Two of the dark field images are shown in Fig. 5.2(a) and (b) along with their diffraction patterns and the reflection used for the dark field images. These overview images consistently reveal a high density of dislocations, with pronounced dislocation structures,  $\rho_d \approx 130 \cdot 10^{12} \text{ 1/m}^2$  estimated using the method by John Steeds [164]. Dislocations appear through the thermal contraction during the cool down step after deposition. This contraction induces a biaxial tensile strain in the thin film well beyond the yield strain. Besides dislocations, many precipitates can be observed. Most of them were GP zones, which were identified in HRTEM Al[110] bright field images, as shown in Fig. 5.2(c) and (d). Moreover, this identification was confirmed by local EDS analysis, which showed an increase in copper concentration at the GP zones. The HRTEM images clearly show that GP zones are coherent precipitates of a few nanometer in size, with GP2 being somewhat larger than GP1, in agreement with the literature [72]. Moreover, GP zones were observed throughout the aluminum matrix. Their presence is logical considering the final processing steps at elevated temperatures below the GP-solvi, see Fig. 5.1(a). Furthermore, these specimens have been stored at room temperature for at least two years, during which further GP precipitation and growth is possible.

In addition to GP zones,  $\theta$  precipitates are observed, as shown in Figs. 5.2(e)-(g). The  $\theta$  crystal structure is positively identified from its atomic structure, shown in Fig. 5.2(f), and its selected area diffraction pattern, shown in Fig. 5.2(g). The random misorientation of the Al<sub>2</sub>Cu diffraction pattern with the (faint) Al diffraction pattern, resulting from little aluminum material above or below the  $\theta$  precipitate, shows that their orientations are uncoupled, as one would expect for fully incoherent precipitates. The dark field image in Fig. 5.2(h) also shows that the orientation of the large  $\theta$  precipitate is unrelated to that of its smaller neighbor. These  $\theta$  precipitates lie on an aluminum grain boundary, as shown in Fig. 5.2(e). This is consistent with literature where  $\theta$  precipitates in thin films are mainly found on grain boundaries and at interfaces [43, 55, 116, 118, 120, 175]. However, a few precipitates are also observed in the grain interior. The presence of these precipitates likely results from the relatively high temperatures for short time intervals to which the specimen was exposed during processing.

The most remarkable observation is the fact that one type of precipitates was not found at all: the  $\theta'$  precipitates. Given the thermal history and taking into account that even  $\theta$  precipitates are present, one would expect  $\theta'$  precipitates to be present. Moreover, since  $\theta'$  precipitates principally nucleate at GP zones, dislocations and sometimes even grain boundaries (Ref.[118, 147, 174]), which are abundant here, one would expect the  $\theta'$  precipitates to be finely dispersed over the aluminum matrix and thus be visible in this detailed TEM analysis. Moreover, it will be shown below that X-ray diffraction data also indicates the absence of  $\theta'$  precipitates. Therefore, it is unlikely that the missing  $\theta'$  precipitates are measurement artifacts. The absence of  $\theta'$  precipitates could be related to a kind of precipitation kinetics that is specific to thin films which may explain the absence of a pronounced hardness peak in Fig. 5.1(d).

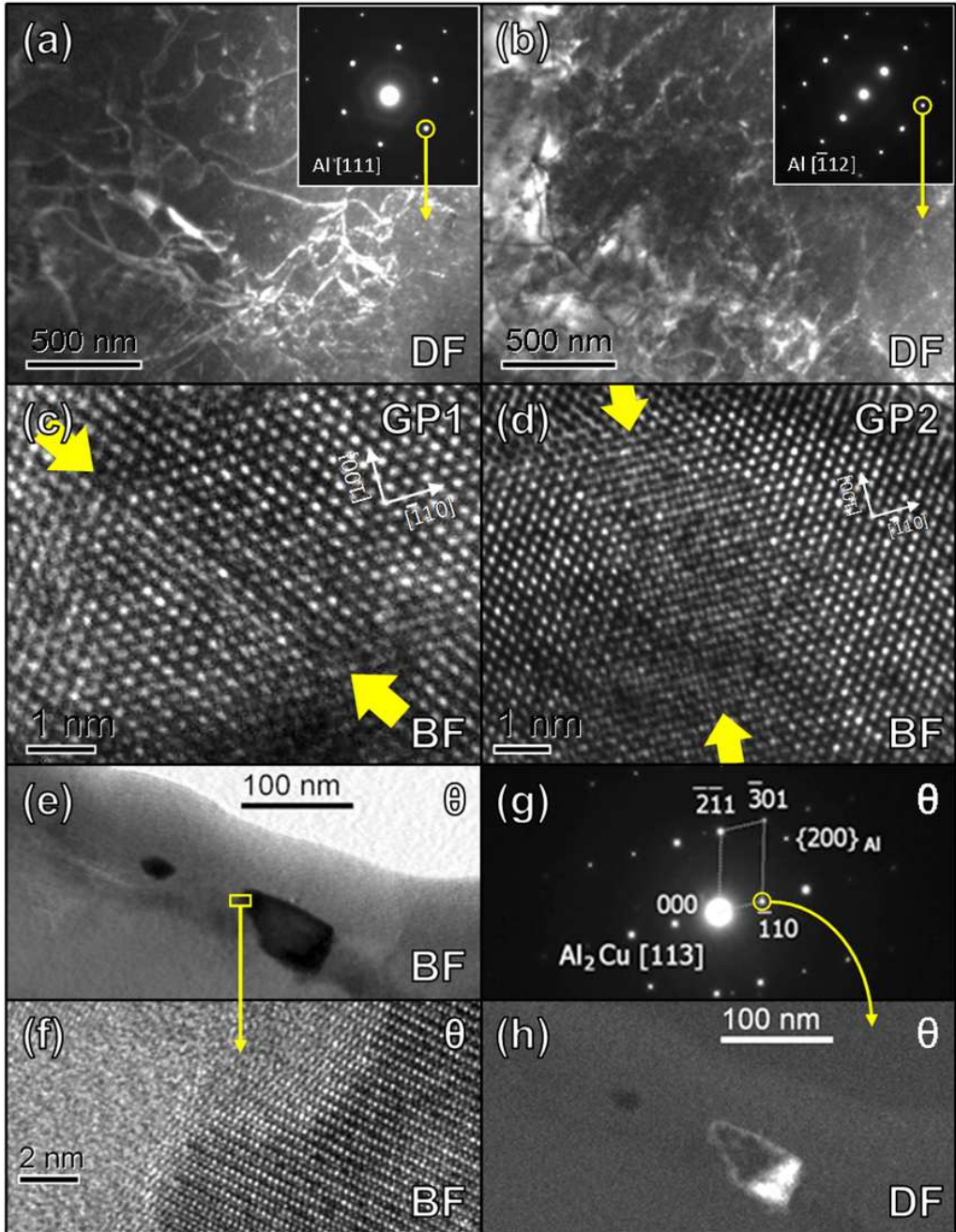


Figure 5.2: Transmission electron microscopy (TEM) images of the as-received Al-(1wt%)Cu microstructure. (a,b) Dark field (DF) image of the aluminum matrix (obtained with the encircled reflection indicated in the diffraction pattern) showing many dislocation structures. (c, d) HRTEM Al[110] bright field (BF) images of the crystal structure of Guinier-Preston zones, GP1 and GP2, as indicated by the arrows. (e,f,g,h) images of  $\theta$  precipitates: (e) two  $\theta$  precipitates at a grain boundary, (f) HRTEM enlargement of the largest precipitate, (g) selected area Al<sub>2</sub>Cu[113] diffraction (SAD) pattern of this precipitate in which the Al<sub>2</sub>Cu crystal structure is identified, and (h) dark field image obtained with the Al<sub>2</sub>Cu{110} reflection, for the same area as (e).

## 5.3 Controlling the precipitate microstructure

The measurements on the as-received material show that a well-controlled heat treatment procedure is required to gain further understanding of the thin film precipitation formation process. Generally, heat treatments for Al-Cu alloys usually involve the following stages [147]: (i) solution treatment and homogenization at a temperature well above the  $\theta$  solvus to dissolve all  $\text{Al}_x\text{Cu}_y$  precipitates and uniformly distribute the Cu-solutes; (ii) rapid cooling or quenching usually to room temperature to obtain a supersaturated solid solution ( $\alpha'$  phase); (iii) aging to enable controlled decomposition of the  $\alpha'$  phase through subsequent formation of GP1, GP2,  $\theta'$ , and  $\theta$  precipitates, as explained in the introduction. Concerning step (i), complete homogenization of Al-(1wt%)Cu, requires a temperature well above  $\sim 350$  °C, see Fig. 5.1(a). Here, the choice was made for 15 minutes at 550 °C based on a calculation of the maximum required diffusion time for given diffusion length ( $\sim 10$   $\mu\text{m}$ ) at this temperature, which results in negligible native oxide growth [18] or grain growth (further discussed below). Regarding step (ii), quenching in water results in mechanical deformation due to stiction of the free-standing MEMS structures to the underlying silicon chip, while quenching in air is too slow. Therefore, a quenching procedure was developed, in which the silicon chip is placed on a thin layer of ethanol on a large cold polished block of copper. The ethanol layer greatly enhances the heat transfer achieving a cooling rate of  $\sim 300$  °C/s, while having a thickness less than half the chip thickness, which prevents the wetting of the chips surface. Finally, step (iii) requires again an appropriate combination of aging time,  $t_{\text{aging}}$ , and temperature. An aging temperature of 190 °C was chosen for two reasons: (I) it is well above the GP1 and GP2 solvi (see Fig. 5.1(a)), which excludes the formation of GP-zones and limits the type of expected precipitates to  $\theta$  and  $\theta'$ , thereby facilitating interpretation; (II) this temperature was also used in the hardness measurements of bulk Al-Cu in Fig. 1(b), which enables direct comparison.

### Solution heat treatment

A series of Al-(1wt%)Cu MEMS structures were subjected to the proposed heat treatment, for which the temperatures were controlled to within 2% of the target temperature. Before investigating the precipitation formation process, it was validated whether all alloying elements had dissolved without altering the grain size or grain structure. To this end, a chain of the largest  $\theta$  precipitates, which were identified at a particular grain boundary, were compared before and after the solution treatment, see Fig. 5.3. EDS analysis of the copper concentration shows that even these largest  $\theta$  precipitates fully dissolved into the matrix, while Cu redistributed homogeneously over the matrix (compare Fig. 5.3(b) with (c)). Moreover, no traces of other elements besides aluminum and copper were found after homogenization, therefore, the material is not contaminated during the heat treatment.

Additionally, a detailed map of crystal orientations and grain boundaries was acquired before and after solution treatment. Figure 5.4(a) shows a top view specimen image of a free-standing MEMS structure that was imaged with electron back-scatter diffraction (EBSD). No grain boundary migration, nor grain growth can be observed. It is therefore assumed that grain growth does not occur in the subsequent aging heat treatment at 190 °C. Furthermore, it was analyzed whether systematic spatial variations in the (average)

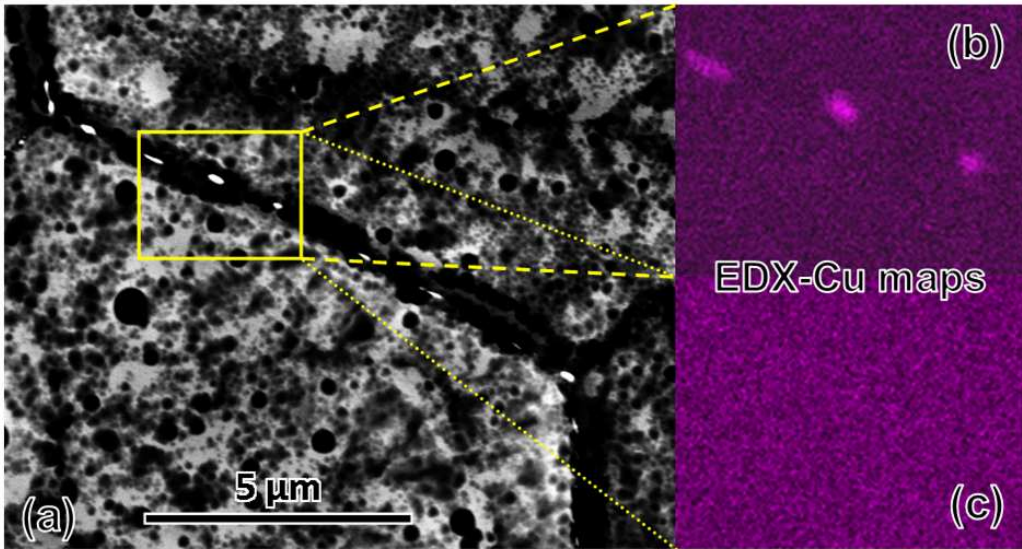


Figure 5.3: The effect of the homogenization step at 550 °C on the precipitate state in the as-received Al-(1wt%)Cu material. (a) back-scatter electron (BSE) image of large  $\theta$  precipitates (with sizes up to half a micrometer) aligned on a grain boundary. (b,c) EDS maps of the copper concentration (b) before and (c) after the solution heat treatment, showing that all copper has been dissolved. BSE and EDS performed in a FEI Sirion FEG-SEM with EDAX EDS system and Apollo SDD detector. BSE obtained with  $E_{\text{beam}} = 15$  kV, EDS measured with  $E_{\text{beam}} = 20$  kV.

grain structure for different positions on the wafer exist due to thermal gradients during processing. To this end, large portions of the wafer were imaged using light microscopy, see Fig.5.4(b), and it was found that the grain size was smaller near the wafer edge. Subsequent EBSD analysis showed that the grain size at the wafer center and edge is, respectively,  $(14 \pm 6) \mu\text{m}$  and  $(7 \pm 3) \mu\text{m}$ , of which Fig. 5.4c gives an example. Moreover, EBSD consistently shows that the Al-(1wt%)Cu thin films have a pronounced Al $\langle 111 \rangle$  texture, i.e. the vast majority of crystals have their  $\langle 111 \rangle$  axis aligned within  $20^\circ$  to the surface normal. To exclude grain size effects, all further analyses were performed on specimens obtained from the wafer center.

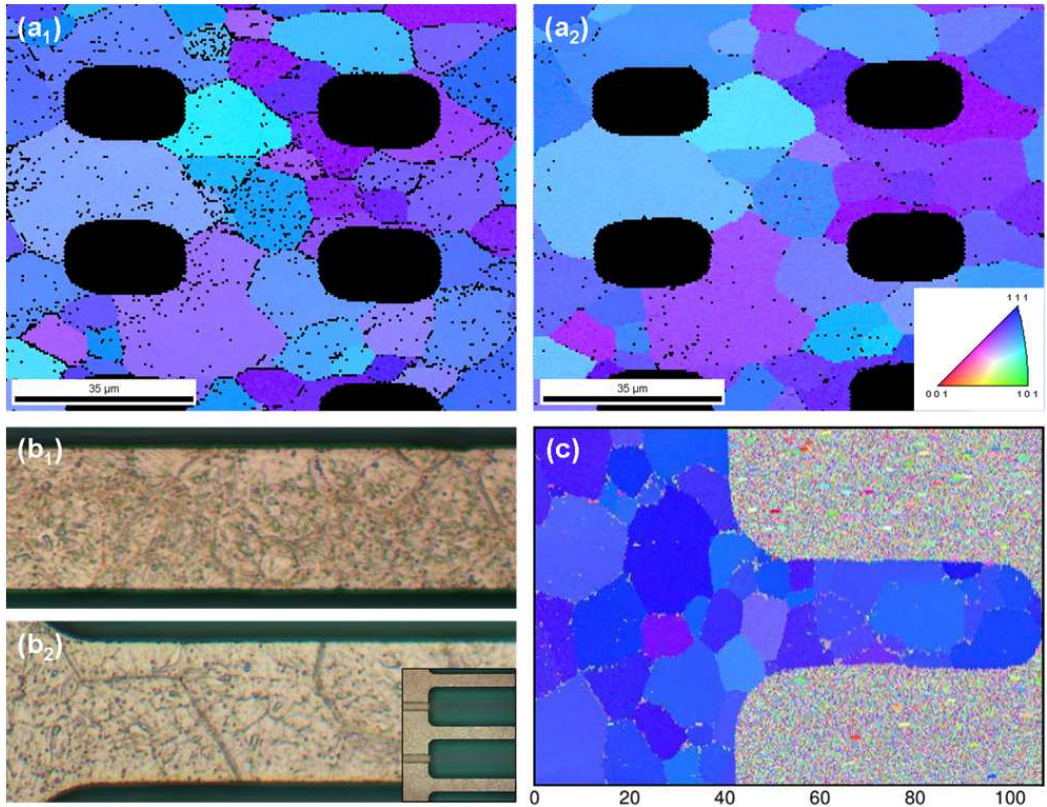


Figure 5.4: (a) electron back-scatter diffraction (EBSD) measurements of a free-standing MEMS structure before (a1) and after (a2) the solution treatment of 15 minutes at  $550^\circ\text{C}$ , for which no grain boundary motion could be observed (the black areas are holes in the free-standing structure, introduced for underetching these structures to remove a sacrificial layer during processing). (b) Examples of optical images, obtained at the edge (b1) and at the center (b2) of the wafer, which were used to investigate systematic differences in grain size over the wafer. Etching during processing attacked grain boundaries, making these optically visible (broad lines). The small inset shows an overview of a set of  $20 \mu\text{m}$ -wide free-standing cantilevers. (c) Example of an EBSD image of a cantilever with anchor, which was used to analyze grain sizes and grain boundaries. The colors in figures (a) and (c) indicate the local crystal orientation according to the inverse pole figure color map shown in the inset, indicating a pronounced Al $\langle 111 \rangle$  texture of the grains in the Al-(1wt%)Cu thin films. EBSD collected with FEI Sirion FEG-SEM and EDAX OIM system with  $E_{\text{beam}} = 20 \text{ kV.}$ , step size of  $0.5 \mu\text{m}$ .



## Artificial aging

Since the solution heat treatment did not alter the grain structure, nano-indentation measurements were performed on sections of Al-Cu thin film that were substrate-supported by the chip as a relatively fast way to identify the peak-aged condition. An MTS XP nano-indenter in a controlled environment (pneumatic vibration isolation table,  $T = 21 \pm 0.5$  °C) was operated under load control with indentation depths limited to 500 nm, in accordance with the 10%-film thickness rule. Preliminary measurements showed, however, an unexpected decrease in the hardness instead of a peak, as already stated in the introduction. The indentation procedure was scrutinized for possible influences of: mounting-induced specimen tilt, surface roughness, underlying substrate, choice of hardness extraction procedure (that of [74, 156] was finally adopted under the assumption of known and constant reduced modulus), variation of indentation depth (from 100 nm to 500 nm), and the time of day and order of the measurements. However, the decrease was persistent and could not be explained by any of these possible effects. To exclude the potential influence of individual grain boundaries underneath the indenter tip, the initially-used Berkovich tip was replaced by a large spherical indenter ( $d = 250$   $\mu\text{m}$ ), which reduced the measurement noise further, yielding the data shown in Fig. 5.1(d). From these indentation analyses it was concluded that the unexpected trend in hardness is not caused by a measurement artifact or a variation in grain structure. The observed effect must be due to intra-granular changes in the microstructure induced by the aging treatment. Based on the large change in hardness after  $t_{\text{aging}} = 8$  h, artificial aging times of 0, 6, 8, 10, and 24 hours were selected for further analysis of the precipitation state.

X-ray diffraction (XRD) spectroscopy was performed to identify the precipitates present at these five aging times. To this end, the Al-(1wt%)Cu MEMS structures were transferred from the underlying substrate which contained several unknown thin films. The structures are gently embedded in a thin layer of cyanoacrylate glue and, after solidification of the glue into a foil, the foil is removed from the chip. Preliminary XRD 2-theta line-scan measurements using a powder diffractometer did not show the expected precipitates. The absence of diffraction peaks may be caused by a preferential texture of the precipitates or a limited amount of precipitates of random orientation in the measurement volume, through which diffraction peaks can be missed in an XRD line scan. Therefore, 2D wide-angle X-ray diffraction (WAXD) patterns were obtained at the European Synchrotron Research Facility, see Fig. 5.5(a)-(e). Measurements were performed at the BM26B DUBBLE beam line: beam diameter of  $\sim 5$  mm; wavelength of 0.1033 nm; CCD detector with resolution of  $1024^2$  and  $97.65\mu\text{m}^2$  pixels positioned at a distance of  $\sim 75$  mm. Specimens were mounted in transmission configuration with the surface normal parallel to the X-ray beam. To facilitate their interpretation, radial diffraction plots were obtained by (i) azimuthal integration of the intensity rings in the WAXD patterns of Fig.5.5 and (ii) subsequent subtraction of the corresponding glue background spectrums (e.g. Fig. 5.5(f)). This procedure yielded the five radial intensity spectra shown in Fig. 5.6.

All five specimens show a strong Al{111} reflection at  $2\text{-theta}=25.50$  that is much larger than the Al200 reflection at  $2\text{-theta}=29.50$ , which in fact is only observed for  $t_{\text{aging}} = 8$  h and  $t_{\text{aging}} = 10$  h specimens, see Figs. 5.5 and 5.6. This large difference in peak intensity is due to the predominant Al{111} texture, also observed with EBSD in Fig. 5.4, whereas the few individual reflections on the Al{200} ring in Fig. 5.5(c) and (d) indicate the presence of

a few crystals that have a large misorientation relative to the Al $\langle 111 \rangle$  texture within the  $\sim 5$  mm broad X-ray beam. Indeed, 3D-orientation calculations show that the predominant Al $\{111\}$  texture with its misorientation spread within  $\sim 20^\circ$ , favors the Al $\{111\}$  reflection, which is strongest for crystals with a misorientation of the  $\langle 111 \rangle$  axis to the surface normal of  $\sim 8^\circ$  (which depends slightly on the misorientation direction), whereas, the Al $\{200\}$  reflection is optimal for an angle of the  $\langle 111 \rangle$  axis to surface normal of  $\sim 40^\circ$ . Crystals with such a large misorientation are rare and could not be observed in the three EBSD images in Fig. 5.4.

Besides these aluminum peaks, only two other reflections, at  $2\text{-}\theta = \sim 27.5^\circ$  and  $\sim 28^\circ$ , could be positively identified above the noise level, and only for aging times of 10 h and especially 24 h. These two reflections do not correspond to aluminum or  $\theta'$  reflections. Instead, they are attributed to the Al $_2$ Cu $\{220\}$  and Al $_2$ Cu $\{122\}$  reflections of the  $\theta$  precipitates, even though their positions are shifted to a somewhat lower angle compared to the tabulated spectrum of bulk Al $_2$ Cu (known as Khatyrkite). This shift would correspond to a tensile strain of  $\sim 0.5\%$  in the  $\theta$  precipitates, which may be realistic since these precipitates preferentially grow in the grain boundary grooves at the surface, as discussed below, where surface tension is high [135]. This case may be comparable to the tensile stress that develops in the island-coalescence regime in thin film deposition [54]. Moreover, the smooth shape of the Al $_2$ Cu $\{122\}$  ring in azimuthal direction indicates that a considerable quantity of  $\theta$  precipitates was present in the X-ray beam. However, even though TEM analysis (Fig. 5.2) revealed  $\theta$  precipitates that are fully incoherent with the aluminum matrix, the Al $_2$ Cu $\{122\}$  ring in the WAXD spectra of Fig. 5.5(d) and (e) show a pronounced preferential orientation, which again may be related to their growth at the surface and in grain boundary grooves. This preferential orientation explains the mismatch in the ratio of the  $\{220\}$  to  $\{122\}$  intensities compared to the tabulated bulk Al $_2$ Cu spectrum, as well as the absence of the two other expected Al $_2$ Cu reflections (i.e. the  $\theta\{211\}$  and  $\theta\{222\}$  reflections at, respectively,  $2\text{-}\theta = \sim 25^\circ$  and  $\sim 37^\circ$ ). These latter reflections could also be eclipsed by, respectively, the nearby Al $\{111\}$  reflection and the large noise level close to the end of the detector range at  $2\text{-}\theta = \sim 38^\circ$ .

Finally, it is striking that none of the three  $\theta'$  reflections (i.e. the  $\theta'\{200\}$ ,  $\theta'\{103\}$ , and  $\theta'\{202\}$  reflection at, respectively,  $2\text{-}\theta = \sim 20^\circ$ ,  $\sim 34^\circ$ , and  $\sim 36^\circ$ ) were observed for any of the five specimens. As  $\theta'$  precipitates nucleate in the Al-Cu bulk at GP zones or dislocations, they are expected to be finely-dispersed over the aluminum matrix [147], while their amount is expected to be noticeably larger than that of  $\theta$  precipitates, which were already observed in large quantity in the X-ray beam. Especially the absence of the strong  $\theta'\{103\}$  reflection is surprising. Because of their semi-coherent nature,  $\theta'$  precipitates have their  $[001]$  axis parallel to Al $[001]$  [147]. Therefore, the strong Al $\{111\}$  texture strongly affects the orientation distribution for  $\theta'$ . 3D-orientation calculations show that half of the  $\theta'$  population should be favorably oriented for the  $\theta'\{103\}$  reflection, which, for this sub-population, is strongest for aluminum crystals with a misorientation of the  $\langle 111 \rangle$  axis to the surface normal of  $\sim 10^\circ$  also depending slightly on the misorientation direction. Therefore, taking into account the misorientation spread of  $\sim 20^\circ$  of the Al $\langle 111 \rangle$  texture, the strong  $\theta'\{103\}$  reflection should be present if  $\theta'$  precipitates are present in the aluminum matrix. The absence of  $\theta'$  reflections is in line with the TEM observations, although the solution treatment and aging likely reduce nucleation sites for  $\theta'$ : dislocations could be largely annealed during solution treatment, while GP zones would be dissolved due to the

aging temperature being above their solvi.

More insight in the formation of  $\theta$  precipitates may be gained by measuring the copper concentration over the film thickness as a function of aging time. To this end, focused ion beam milling was used to make slanted cross-sections of the aged free-standing films, after which back-scatter electrons (BSE) images and EDS-Cu images were measured to investigate the evolution of the copper concentration, see Fig. 5.7. Note that only copper clusters above a few tens of nanometers exceed the EDS noise level, which must be  $\theta$  precipitates because  $\theta'$  has been ruled out and GP zones are assumed not to be present at an aging temperature of 190 °C. In the BSE images also smaller precipitates can be identified, whereas precipitates in roughness valleys are not or only partially visible.

Now let us first examine the evolution of the  $\theta$  precipitates on the top surface. As already discussed above (Fig. 5.3(c)), after homogenization, the copper concentration is homogeneously distributed. After 6 hours of aging, a few surface precipitates can be observed. With only 2 and 4 additional hours of aging, many more and larger precipitates appear at the surface, and it becomes apparent that most of them are located in a grain boundary groove (GBG). For the 24h specimen, much more precipitates are found on the surface, however, the increase of precipitate size seems to have saturated. Conversely, the internal  $\theta$  precipitates, which are observed from the cross-section, follow the opposite trend. For both 6 and 8 hours of aging, two internal precipitates were found in the film interior and all four of them were located at a grain boundary. However, the two precipitates of the 6h specimen are larger than their 8h aging counterparts, and from 10 hours aging onward no precipitates are found anymore in the grain interior. This suggests that the few  $\theta$  precipitates that have nucleated on the internal grain boundaries within the first 6 hours of aging, gradually disappear upon further aging. Although  $\theta$  precipitates are thermodynamically stable, they may dissolve for two reasons: (I) small precipitates may dissolve facilitating the growth of a few large precipitates to reduce system's precipitate-matrix interface energy, so called Ostwald ripening [72]; (II) if energetically more favorable sites are present within the copper diffusion length, e.g. free surface or GBGs, a net copper-flux to these lower-energy sites may occur.

Summarizing the observations made: (a) the  $\theta'$  precipitates are absent in the detailed TEM analysis of the as-received material; (b)  $\theta'$  precipitates are absent in the WAXD analysis; (c) no peak-aged condition is found in the hardness measurements of these films. Other investigations of thin film Al-Cu of similar composition also have not revealed the presence of  $\theta'$  [116]. It may therefore be concluded that  $\theta'$  precipitates are most likely absent in these Al-(1wt%)Cu thin films. Apparently the precipitation behavior is quite different from that of its bulk counterpart; this faster formation may be related to the nearby presence of free surface for thin films.

The following hypothesis explains the absence of  $\theta'$  and the relatively fast occurrence of  $\theta$  in the thin film compared to the bulk alloy. It is reasonable to assume, that most  $\theta$  precipitates nucleate in a GBG because GBGs are the energetically most favorable locations for  $\theta$  to nucleate in these thin films. This implies that the total defect energy, of GBG and precipitate, lowers inside a GBG, by partially relaxing the high surface tension that exists in GBGs [54, 135]). The hypothesis that the total defect energy is lower than in the bulk alloy may explain a number of observations: (i) it causes a net flux of copper atoms from  $\theta$  precipitates in the grain interior and on internal grain boundaries to  $\theta$  in GBGs,

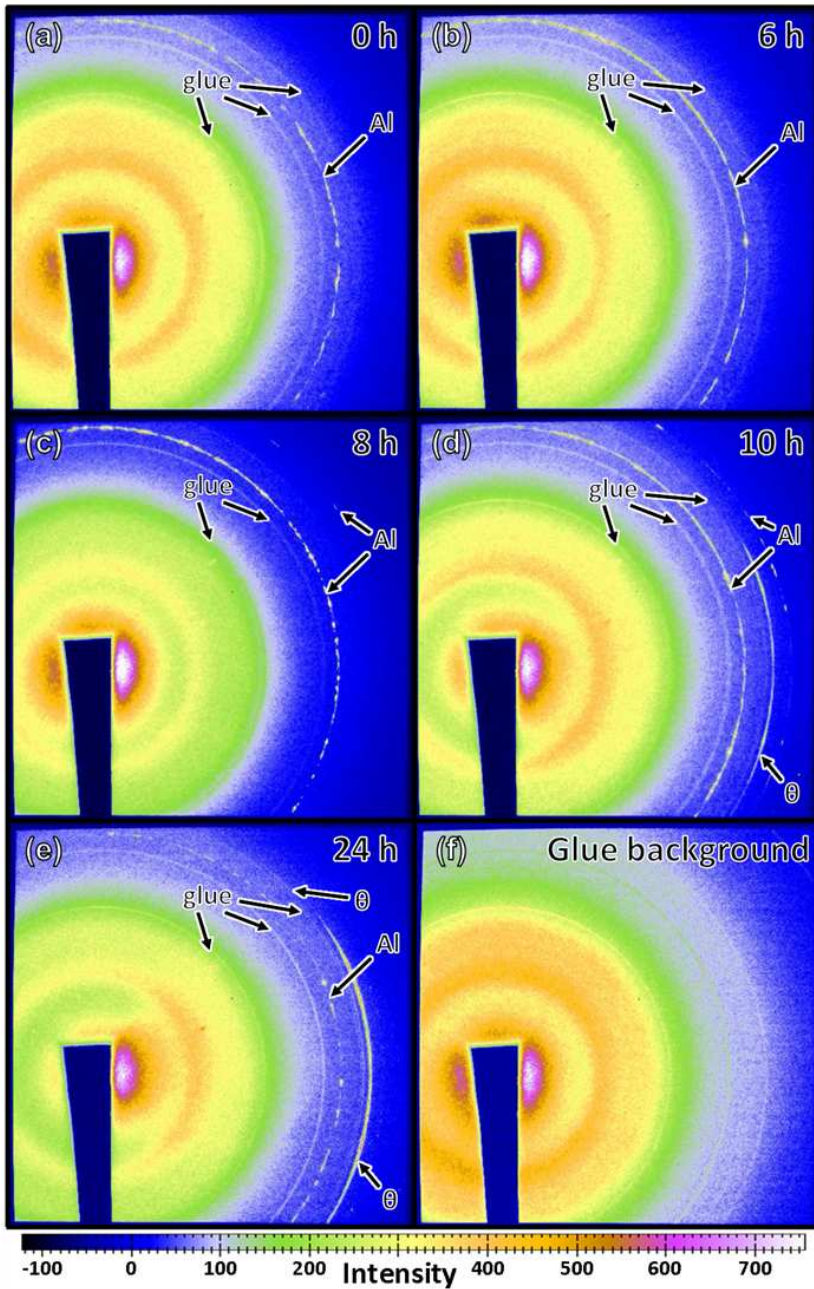


Figure 5.5: raw 2D wide-angle X-ray diffraction (WAXD) patterns, for Al-(1wt%)Cu MEMS structures, artificially aged at (a) 0, (b) 6, (c) 8, (d) 10, and (e) 24 hours, and subsequently transferred from their underlying substrate to cyanoacrylate(glue) foils. For each aging state, Al-Cu-on-glue and glue-only diffraction pattern were recorded, where the (supposedly amorphous) glue showed a few minor reflections attributed to polymer crystallization, see, e.g., (f). Indicated in the images are the most pronounced diffraction rings of aluminum,  $\theta$  precipitates, and glue.

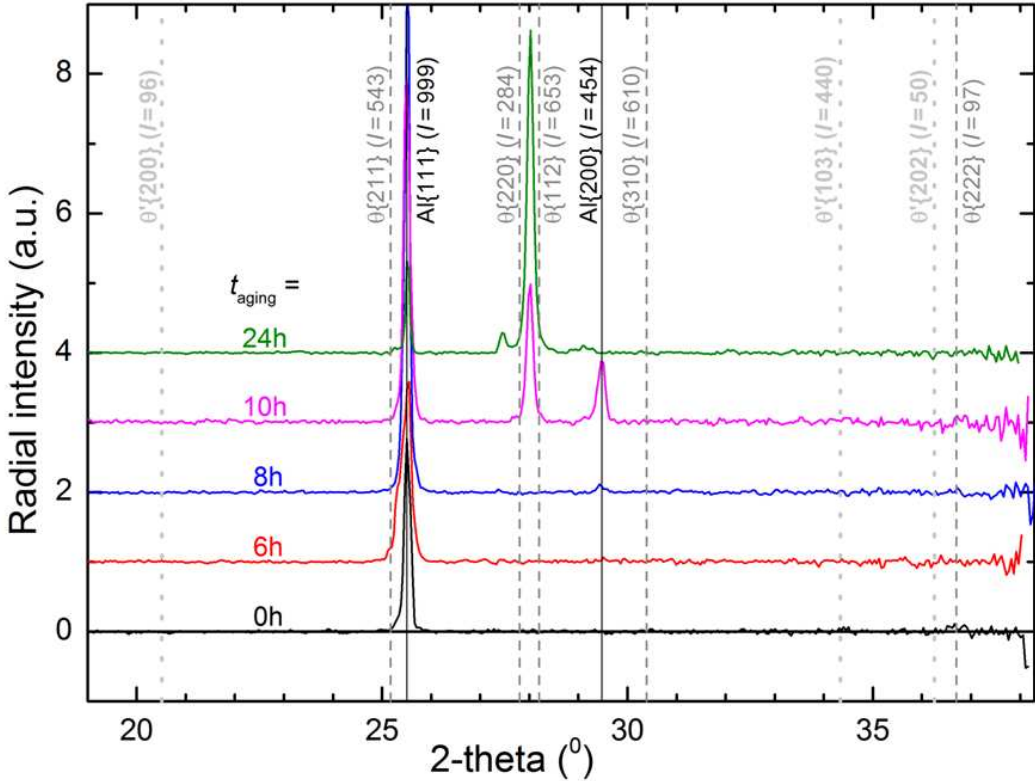


Figure 5.6: Radial X-ray diffraction spectra of Al-(1wt%)Cu, artificially aged for  $t_{\text{aging}} = 0, 6, 8, 10,$  and  $24$  hours, where the radial diffraction intensity is obtained by (i) azimuthal integration of the intensity rings in the 2D WAXD patterns of Fig. 5.5. and (ii) subtraction of the corresponding glue background spectrums. For clarity, the spectra are vertically shifted with increasing aging time. Reference positions of reflections that are pronounced enough to rise above the noise level are indicated by solid, dashed, and dotted vertical lines for, respectively, aluminum [143],  $\theta$  precipitates [123] and  $\theta'$  precipitates (calculated using hkl-indices from [162] and d-spacing values from [72]). The relative intensity between reflections of the same crystal is indicated between the brackets with a maximum of 999.

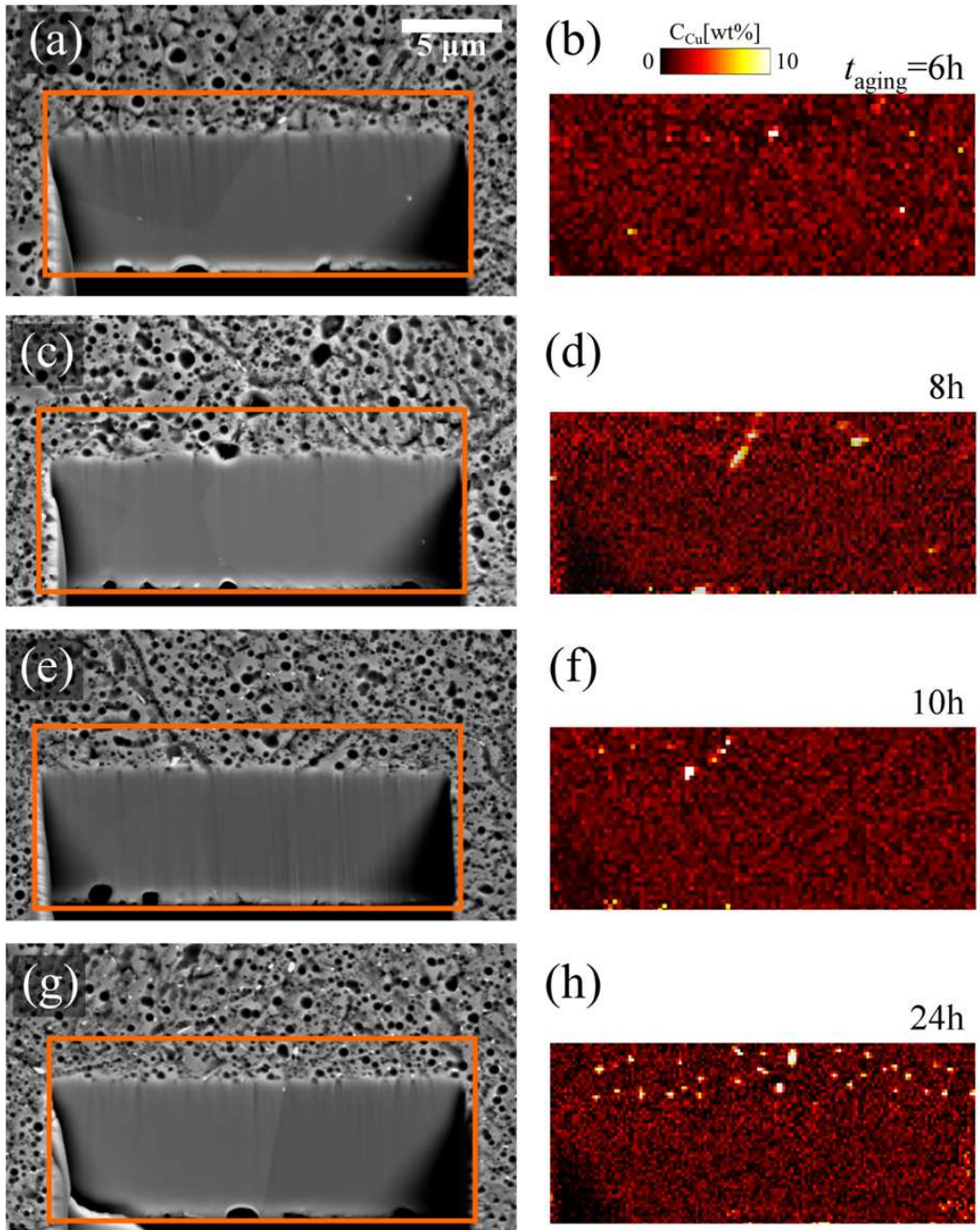


Figure 5.7: (left) Back-scatter electron (BSE) images of slanted cross-section of (different) free-standing 5 μm-thick Al-(1wt%)Cu structures, artificially aged for different  $t_{\text{aging}}$ . (right) Energy dispersive X-ray spectroscopy (EDS) images of the copper concentration, corresponding to the region in the orange box on the left. From top to bottom, image pairs (a,b), (c,d), (e,f), and (g, h) correspond to  $t_{\text{aging}} = 6, 8, 10,$  and  $24$  hours. The cross-sectional EDS-Cu plot of  $t_{\text{aging}} = 0$ h (not shown) is completely homogeneous, in agreement with Fig. 5.3(c). BSE images obtained with  $E_{\text{beam}} = 10$  kV. EDS mapping performed with  $E_{\text{beam}} = 5$  kV., resulting in  $d_{\text{X-ray volume}} \approx 0.5$  μm.

i.e. explaining the gradual disappearance of the former  $\theta$  precipitates after  $\sim 8$  hours of aging; (ii) it favors  $\theta$  nucleation, since it induces a larger reduction in free energy than  $\theta'$  nucleation, which could only occur in the aluminum matrix; (iii) it triggers a higher  $\theta$  nucleation rate in GBGs than in the bulk, thereby explaining the faster appearance of  $\theta$  in Al-(1wt%)Cu thin films (only  $\sim 8$  hours) compared to the bulk Al-(1wt%)Cu alloy (more than  $\sim 10$  days), see Fig. 5.1(b)). The free surface is expected to have a less strong, yet similar role as the GBG in (iii). Hence, it is suggested that the GBGs are energetically more favorable for Cu to diffuse to and precipitate at as  $\theta$ , thus preventing the nucleation of  $\theta'$  and reducing the  $\theta$  precipitation in the bulk of the film.

## 5.4 The hardness decrease revisited

A possible explanation is next formulated for the observed hardness decrease in the nano-indentation measurement on these Al-(1wt%)Cu thin films. With increasing aging time, copper can easily diffuse to the surface, using the internal grain boundaries as fast diffusion pathways, where  $\theta$  precipitates start to nucleate in the GBGs already after a couple hours. These, however, are not expected to affect the indentation hardness, because their presence on the surface does not obstruct the dislocation motion in the interior. At the same time, a limited amount of  $\theta$  precipitates will form in the interior and on internal grain boundaries, because this requires shorter copper diffusion distances. These internal  $\theta$  precipitates do form obstacles for dislocation motion, and indeed trigger a minor increase in hardness as seen in Fig. 5.1(d) around  $t_{\text{aging}} = 6$  h. This is in line with traditional precipitate strengthening theory. Later on, see Fig. 5.1, these internal  $\theta$  precipitates dissolve, favoring precipitate growth at the surface or GBGs, which is in line with Ostwald ripening [72]. This may explain the hardness decrease at  $\sim 8$  h aging. At the same time, the  $\theta$  precipitates at the surface not only increase in number, but also grow to a considerable size, forming sufficiently large obstacles to dislocations that tend to escape from the surface. This may cause dislocation pile-ups at these surface precipitates. Towards 24 h aging, the size of the surface precipitates stabilizes, which may explain the saturation in hardness for large aging times.

## 5.5 Conclusions

Nano-indentation hardness measurements of 190 °C aged Al-(1wt%)Cu thin films showed a weak peak-aged condition followed by a decrease in hardness. A detailed microstructural analysis on the as-received thin film with HRTEM revealed that GP zones and  $\theta$  precipitates were present, while  $\theta'$  could not be observed. The presence and location of GP-zones and  $\theta$  precipitates were explained by the thermal history and appears to be consistent with literature observations. The absence of  $\theta'$  precipitates, though in line with other literature reports, could not be trivially explained for the as-received thin film, since suitable potential nucleation sites were present and the thermal history did not a priori preclude the formation of  $\theta'$  precipitate.

Since the observations of the as-received thin films were not conclusive, Al-Cu specimens were next solution treated at 550 °C and artificially aged at 190 °C up to 48 hours to create

a well defined precipitation state without GP zones. EBSD did not show any grain growth. EDS confirmed the dissolution of existing precipitates and a homogeneous distribution of Cu prior to aging. Measurements of the hardness of aged specimens revealed a slight increase in hardness at 6 hours, followed by a decrease in hardness at  $\sim 8$  hours and subsequently a slow increase and saturation of the hardness. A selection of specimens around this hardness transition was analyzed with WAXD, BSE-imaging and EDS-mapping. WAXD confirmed the presence of  $\theta$  precipitates for aging durations longer than 8 hours, while indicating that  $\theta'$  was not present. Consistently, no  $\theta'$  was identified in TEM, suggesting that precipitation of  $\theta'$  must be highly unfavorable in thin films. Through-thickness measurements using BSE and EDS of aged specimens highlighted that Cu clusters, i.e.  $\theta$  precipitates, nucleate and grow essentially at grain boundary grooves, though also at the specimen surface, at the expense of the interior of the thin film.

The following hypothesis explaining these observations was made. Precipitation of  $\theta$  is favored, because energetically favorable grain boundary grooves act as preferred nucleation sites. This would occur more easily than  $\theta'$  precipitation, hence explaining the absence of  $\theta'$ . It also occurs faster than regular  $\theta$ -precipitation in the interior of the thin film, thereby explaining the relatively fast nucleation of  $\theta$ , as seen in WAXD. Finally, it is hypothesized that the growing precipitation at the surface and grain boundary grooves depletes the Cu in the thin film interior. This would explain the observed weakening of the material, reflected by a decrease in hardness, followed by strengthening through the precipitate-rich surface, resulting in a minor increase in hardness for longer aging times.

## Acknowledgment

Prof. dr. J. Th. M de Hosson and dr. J. Rao of the Materials Science group, Department of Physics at the University of Groningen are gratefully acknowledged for the TEM analyses. For preliminary X-ray diffraction and subsequent discussions the authors acknowledge ing. M. M. R. M. Hendrix at the Department of Chemical Engineering and Chemistry, Eindhoven University of Technology. ir. M. van Drongelen is thanked for providing beam-time and performing WAXD measurements at the DUBBLE beamline at the ESRF. BSc. B.A. G ottgens is acknowledged for performing the nano-indentation experiments and grain size characterization.





## Chapter 6

# On the underlying micromechanisms in time-dependent anelasticity in Al-(1wt%)Cu thin films

---

Reproduced from; L.I.J.C. Bergers, J.P.M. Hoefnagels and M.G.D. Geers, *On the underlying micromechanisms in time-dependent anelasticity in Al-Cu alloy thin films*, in preparation

### Abstract

This chapter discusses potential micromechanisms underlying time-dependent anelasticity observed in Al-(1wt%)Cu thin films. The analyzed deformation mechanisms involve dislocations, solute diffusion, grain boundaries and precipitates. In order to investigate the role of these mechanisms, Al-(1wt%)Cu alloy thin films are heat treated to systematically change the precipitate state, while characterizing the grain boundary distribution with EBSD. Micromechanical characterization is performed by microbeam bending, nano-tensile creep testing and nano-indentation. Results in microbeam bending reveal a similar time-dependent evolution of the anelastic strain after load release for all precipitate and grain boundary states considered. The magnitude of the recovered strain also does not significantly vary with the precipitate or grain boundary configuration. The nano-tensile creep test also indicates the same time-dependent anelastic evolution, indicating that the loading state does not effect the underlying mechanisms. Hence, the results obtained do not reveal a discernible effect of the precipitate state, the grain boundary density or the loading state. Based on uniaxial creep and time-dependent anelasticity measurements in pure Al specimens, it is made plausible that the time-dependent anelasticity most likely originates from dislocation climb limiting the depinning and by-pass of entangled dislocations, while distributed dislocation pile-ups pinned at dislocation lines provide an internal driving force.

## 6.1 Introduction

Time-dependent anelasticity, i.e. the recovery of plastic deformation over time, affects manufactured metal products at the macroscale, e.g. delayed spring back in sheet metal [176, 177], and at the microscale [9]. As demonstrated in Ch.2-4 for microbeams and microtensile specimens of Al-(1wt%)Cu, summarized in Fig.6.1, time-dependent anelasticity contributes significantly in the minutes and days following the removal of the external load, whereas at the macroscale it only becomes relevant at time scales of weeks or longer. This significant effect at the microscale compromises the reliable operation of metallic micro-electromechanical systems (MEMS)[32, 121, 185], e.g. radio-frequency MEMS switches in which deformation states are switched at both high and low frequencies. The underlying micromechanisms responsible for this anelastic response in Al-Cu alloy thin films are not well understood, which is the motivation of this study.

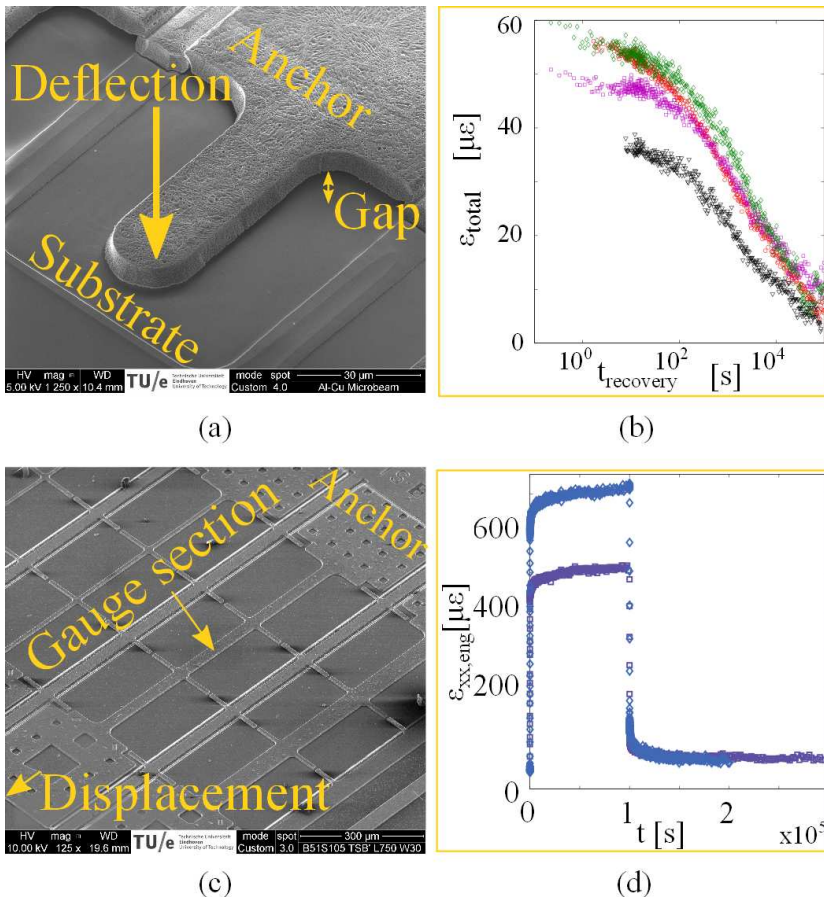


Figure 6.1: (a) Al-(1wt%)Cu microbeams revealing time-dependent anelasticity (b) after releasing a prolonged deflection. (c) Al-(1wt%)Cu microtensile specimens show (c) creep under prolonged constant load followed by time-dependent anelasticity after load removal.

The occurrence of time-dependent anelasticity necessitates an internal driving force that reverses the deformation in the absence of an external load. Additionally, a diffusion-limited mechanism is required to retard the deformation recovery over time scales of seconds, days or even longer. Internal driving forces may originate from back-stresses induced by polarized dislocation structures formed during deformation at obstacles like grain boundaries, other interfaces, precipitates, obstacles or under loading conditions that trigger a heterogeneous distribution of geometrically necessary dislocations (GNDs), e.g. beam bending [40, 134]. Triple junctions or irregularities at grain boundaries may also store energy during grain boundary sliding, which is also a possible diffusional mechanisms [15, 148]. Alternative diffusional mechanisms are dislocation climb at particles or precipitates [3], or dislocation pinning and drag by solutes [72, 97, 154]. Reports that explicitly discuss thin film time-dependent anelasticity, mostly put forward grain boundary sliding as an explanation [4, 29, 88, 91, 108, 109, 114, 178, 179]. However, the studied materials are mainly pure, small grained ( $d \leq 3 \mu\text{m}$ ), aluminum thin films ( $\leq 3 \mu\text{m}$ ) and reveal limited relaxation times in the order of minutes at room temperature. Other reports on nanocrystalline and microcrystalline specimens, which discuss time-dependent anelasticity under the name of reversible plasticity, explain the behavior through residual stresses due to highly heterogeneous deformation, which is recovered by thermally activated dislocation mechanisms [117, 149, 150]. Even though several explanations of the observed time-dependent anelastic behavior offer exist, they typically depend on the film thickness, grain size and alloy composition, which is different from the Al-(1wt%)Cu thin films studied here. Most striking is the difference between reported time scales and that which is observed for this Al-Cu alloy: seconds to minutes for the reported, versus hours and days for these Al-Cu alloy thin films. It is not clear what mechanisms underlie this difference. Therefore, the goal of this chapter is to investigate which mechanisms may be responsible for the driving force and the diffusional mechanism controlling time-dependent anelasticity of Al-(1wt%)Cu thin films.

The variety of possible mechanisms requires a systematic approach to unravel the physical origin of this time-dependent anelasticity. The alloy microstructure can be systematically varied through heat treatments to create a single precipitate phase in the matrix. Although the grain structure in these Al-(1wt%)Cu structures cannot be altered after fabrication (since recrystallization would require mechanical work), one can take advantage of the statistical variation in grain size, where some specimens have only one or two grains along their length, while others have many grains. The specimens can then be mechanically characterized using microbeam bending to quantify the time-dependent anelastic behavior, as presented in Ch.3. The effect of microstructure is analyzed by quantifying the evolution of time-dependent anelasticity, affected by diffusion-limited mechanisms, as well as the magnitude of anelasticity, affected by the internal driving force. Additionally, the loading state may trigger polarized dislocation structures through GNDs in bending. Therefore, time-dependent anelasticity is also investigated in uniaxial tension.

The following section discusses the characterization of the precipitate state and the granular microstructure. Next, the experimental results are discussed with respect to (i) the precipitate effects on the temporal evolution and the magnitude of time dependent recovery, (ii) the grain boundary effects on the temporal evolution and the quantified time-dependent recovery, (iii) a comparison of bending versus uniaxial tension. The final section discusses the observations, leading to a plausible hypothesis for the underlying mechanism of time-dependent anelasticity in the studied thin films.

## 6.2 Experimental characterization

In order to control the precipitate state, the alloy microstructure of the microbeam specimens was altered according to the procedure applied in chapter 5: after solution treatment and homogenization at 550 °C for 15 min. specimens were aged at 190 °C for a number of hours. The homogenization heat treatment was chosen such that it results in a complete dissolution of all existing precipitates in the as-received state. Subsequently, the aging treatment temperature was selected such that GP-zones will not nucleate and only  $\theta$  and  $\theta'$  can nucleate over time. While it was shown in Chapter 5 that  $\theta'$  precipitates are most likely not present in these specimens, the  $\theta$ -phase was observed to precipitate: with increasing aging duration  $\theta$  precipitates first nucleate and grow at internal grain boundaries, whereas for longer aging times  $\theta$  precipitates nucleate at the surface, predominantly at grain boundary grooves, at the expense of the earlier formed interior precipitates. This transformation from internal to surface  $\theta$  precipitates matches a transition in hardness at approximately 8 hours of aging (at 190 °C). Therefore, specimens with aging times of 0h, 6h, 8h, 10h, and 24h were mechanically tested. In addition, the as-received alloy microstructure, containing a mixture of GP zones and few small  $\theta$  precipitates was also mechanically tested. It was shown in Chapter 5 that the locations of grain boundaries in the aluminum matrix does not change through these heat treatments. Therefore, this specimen set allows for a systematic variation of the precipitate state, without varying the grain boundary microstructure.

The grain boundary microstructure may be independently controlled by using thermo-mechanical treatments, but this is not desirable here. Instead, we exploit the results of Chapter 5 showing that the grain boundary microstructure systematically varies over the wafer due to thermal gradients in wafer-processing, resulting in finer-grained specimens near the edge of a wafer. Local variations in grain size in individual microbeams may be large due to grain size statistics. Therefore, for each tested specimen, each individual grain boundary was identified in orientation imaging maps (OIMs) collected with electron backscatter diffraction (EBSD) (FEI Sirion FEG-SEM with EDAX OIM system,  $E_{\text{beam}} = 20$  kV, stepsize 0.2  $\mu\text{m}$ ), see Fig.6.2(a). Note that these EBSD measurements were performed after mechanical testing to avoid charging induced forces. These might induce a microbeam deflection, which would affect the mechanical response.

These OIMs enabled the direct visualization of the grain boundary structure, from which its influence on the mechanical behavior can be assessed. However, in microbeam bending the stress field is strongly heterogeneous, as illustrated in Fig.6.2(b) in a simulation of a deflecting microbeam. As a result, the role that a grain boundary (GB) might play in the observed time-dependent anelasticity (with respect to grain boundary sliding or as a barrier for dislocation motion causing pile-up and storage of back-stress), depends strongly on its position within the cantilever beam. Hence, to properly account for the grain boundary effect, a qualitative measure is introduced. The GB density is weighted with the normalized stress profile from a linear elastic finite element simulation, i.e. the relative contribution of a grain boundary section to the value of the weighted GB density was linearly scaled with the local stress level at that GB section. Subsequently, the weighted GB densities of all microbeams have been ranked with increasing weighted density from  $\rho'_{\text{GB}} = 1$  to  $\rho'_{\text{GB}} = N$ , with  $N = 47$  the total number of tested specimens. Fig.6.2(c) shows that the spread in grain boundary microstructure within the specimen set is large, from just a few GBs in

total with no GB in the high-stress region at all ( $\rho'_{GB} = 1$ ), to many grain boundaries along the entire specimen ( $\rho'_{GB} = 47$ ).

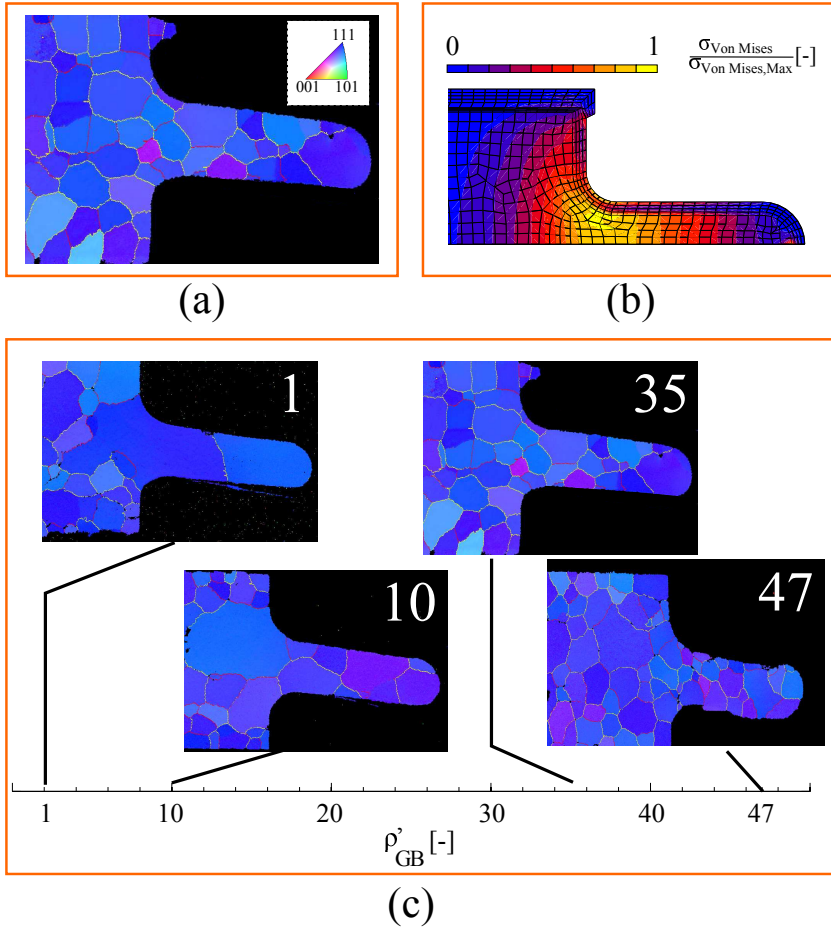


Figure 6.2: (a) EBSD map showing the location of each grain boundary on the specimen. (b) Linear elastic FEM simulation illustrating the heterogeneous stress field upon microbeam bending. Due to symmetry only half the geometry is simulated. (c) The grain boundary locations are weighted with the stress field to obtain a weighted grain boundary density per specimen, which are compared relative to each other to extract a qualitative ranking of grain boundary density,  $\rho'_{GB}$ . The highest number corresponds to the largest weighted grain boundary density within the specimen batch.

Micromechanical characterization was performed in order to evaluate the effects of precipitate state, affected by aging, and grain boundary density on the time-dependent anelasticity. To this end, the microbeam bending methodology presented in Chapters 2 and 3 was employed. Microbeam specimens of  $l = 65$  or  $200 \mu\text{m}$ ,  $w = 21 \mu\text{m}$  and  $t = 4.8 \mu\text{m}$  were selected and in total 47 microbeams, with a minimum of four specimens for each heat treatment/alloy-microstructure variation, were prepared and tested. The experiment consisted of a constant deflection applied to cantilevers during  $10^5$  s, followed by load release and subsequent measurement of the beam curvature evolution, which was converted to strain at the surface where the beam is attached to the anchor. The applied deflection was

varied and together with the various lengths the resulting applied strain ranges between 0.05% and 0.80%. The loading and strain measurement sequence and terminology for the microbeam bending experiment is described in Fig.6.3(a), involving: the total applied strain  $\varepsilon_{\text{hold,applied}}$ ; the applied strain minus the permanent strain  $\varepsilon_{\text{hold,anel.}}$ ; the amount of anelastic strain that is recovered in time after unloading,  $\varepsilon_{\text{anel.,recov.}}$ , and the remaining permanent strain  $\varepsilon_{\text{perm.}}$ .

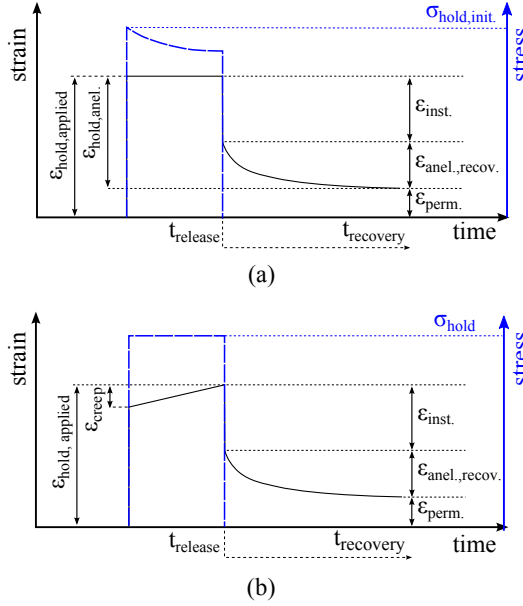


Figure 6.3: (a) The microbeam bending test entails a constant deformation during  $10^5$  s followed by removal of the external load. (b) During nano-tensile creep testing first a constant force is applied during  $10^5$  s followed by removal of the external load.

In addition, nano-tensile tests were performed under conditions that resemble those of the microbeam bending tests, i.e. specimens were also loaded over a period of  $10^5$  s, after which the specimens were unloaded and released to contract freely over time. To this end, the nano-tensile creep test, discussed in Ch.4, was applied to Al-(1wt%)Cu specimens of length  $l = 1050 \mu\text{m}$ ,  $t = 5.3 \mu\text{m}$  and  $w = 10 \mu\text{m}$ , see Fig.6.1(c). The tensile specimens were fabricated in a similar manner as the microbeams, though the processing sequence, and thus thermal history differed. This may result in a slightly different precipitate state compared to the as-received microbeams. The grain boundary distribution, measured with EBSD, revealed an average grain size of  $d = 5 - 8 \mu\text{m}$ . Contrary to the bending tests, the force level in the nano-tensile tests was kept constant to an engineering stress of  $\sigma_{\text{eng.}} = 28.9 \text{ MPa}$ , which is below the yield stress. The yield stress was established by cyclically loading the specimen in the elastic regime 25 times to a stress level between 30-35 MPa, confirming that the load-unload sequence was elastic. The load sequence and involved strains for the creep-anelasticity experiments are described in Fig.6.3(b). In addition to the strains defined in microbeam bending, there is a creep strain,  $\varepsilon_{\text{creep}}$ , during loading. Due to the control-bandwidth of the setup, the force release takes several seconds, necessitating to disregard the initial 10's of seconds in the analysis. A direct comparison

between the tensile and bending strain evolution becomes possible due to the comparable loading sequence.

### 6.3 Time dependent anelasticity in microbeam bending

Microbeam bending experiments were performed for the 47 cantilevers with aging states ranging from as-received to 0h, 6h, 8h, 10h, and 24h aged and weighted grain boundary density ranging from  $\rho'_{GB} = 1$  to  $\rho'_{GB} = 47$ . For each bending test, the strain versus time after load release, i.e. the time-dependent anelastic response (e.g. Fig. 6.1(b)), was obtained. To properly compare the temporal evolution and magnitude of the time-dependent anelasticity, the anelastic model presented in Chapter 3, was applied to this data. It was shown to accurately describe the measured behavior and therefore allows for a good estimation of  $\varepsilon_{perm.}$  and  $\varepsilon_{anel.recov.}(t_{release})$ . By normalizing the temporal evolution using these estimates, the effect of difference in loading amplitude between the different microbeams tests can be eliminated (under equal load duration, as explained in Chapter 3):  $\varepsilon_{anel.recov.norm.} = \varepsilon_{anel.recov.}(t_{recovery})/\varepsilon_{anel.recov.}(t_{release})$ . This enables a direct comparison of the temporal evolution between the various experiments, yielding insight in the diffusion-limited mechanism underlying the time-dependent anelasticity.

The resulting normalized anelastic strain recovery evolution for all microbeams is plotted in Fig.6.4(a). In spite of the scatter of the data, it is an important observation that all specimens display time-dependent anelastic behavior. The apparent small decrease in relaxation time for longer aging times, is clearly smaller than the scatter in relaxation times, with all relaxation times being on the order of approximately a day. Therefore, the time-dependent anelastic behavior seems to originate from the same underlying diffusion-limited mechanism. This is surprising, considering the significant change in precipitate state with aging treatment: from an absence of precipitates at 0h aging, to small interior  $\theta$  precipitates at 6h aging, to only a few large surface  $\theta$  precipitates at 24h aging, to a mixture of precipitates including GP zones for the as-received specimens. Therefore, the responsible diffusion-limited mechanism is expected to be independent of the precipitate state, i.e. precipitates do not play a significant role in this mechanism.

After evaluating the temporal evolution with the anelastic material model, the maximum magnitude of the anelastic recovery,  $\varepsilon_{max,anel.recov.}$ , is extracted with this model to gain insight into the internal driving force. This was done by plotting  $\varepsilon_{anel.recov.}$  as function of  $\varepsilon_{hold,anel.}$ . These results are shown on a double-log plot in Fig.6.4(b). Moreover, from the model's description in Chapter 3, a linear relation can be derived for  $\varepsilon_{anel.recov.}$ , i.e.  $\varepsilon_{anel.recov.}(t_{release}) = A\varepsilon_{hold,anel.}$ , where  $A$  depends on the obtained material parameters,  $E_i$ ,  $\tau_i$  and hold duration. Therefore,  $A$  is expected to change with aging condition. This relation, which yields a line with a slope of 1 on a double-log plot, has been fitted to the measurements per aging state, taking into account the error bars, see Fig.6.4(b). These trendlines facilitate separating the effect of variations in load amplitude between measurements from the possible systematic effects due to the microstructure.

The following observations can be made from Fig.6.4(b). For each aging set, the linear relation appears to capture the response to within experimental error. This confirms that



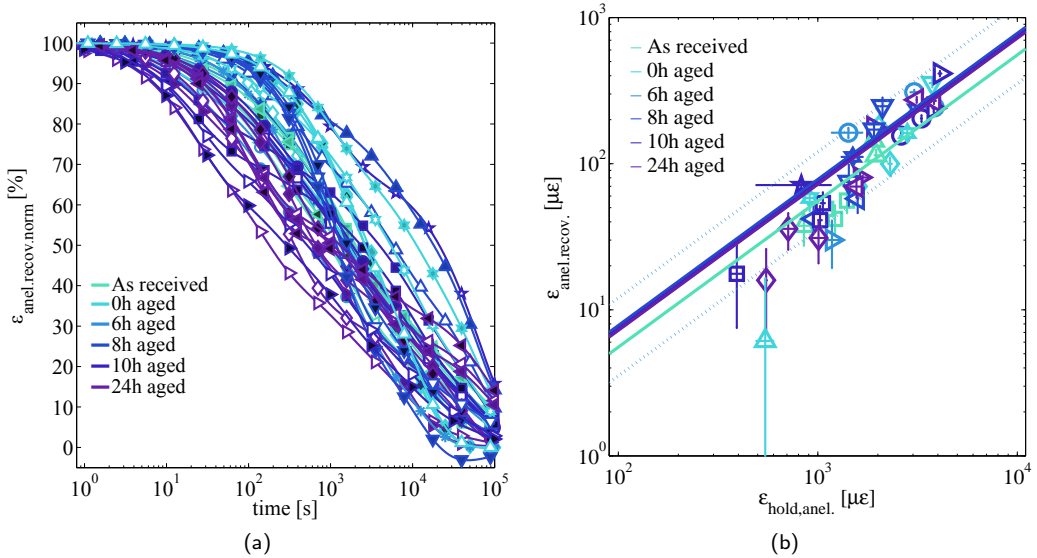


Figure 6.4: (a) the normalized anelastic recovery evolutions after load release and (b) the amplitude of these anelastic recovery evolutions, for all 47 measured microbeam specimens. The heat treatment variation is color-coded from blue/green (light) to purple (dark), ranging from as-received to 24h aging, while symbols denote the different specimens. In (b), for each set of data points of a certain heat treatment, a trendline is added. The upper and lower bounds of the prediction intervals are shown as well.

the applied anelastic model adequately describes the time-dependent anelastic behavior, for all aging conditions. Even though for each aging condition a slightly different model response is obtained, each trendline lies well within the prediction interval. In fact, the trendlines of the 0h, 6h, 8h, 10h, and 24h data sets almost overlap each other, while the trendline of the as received state lies slightly lower. These results suggest that the precipitate state has no discernible effect on the amplitude of the anelastic recovery. Considering the noticeable differences in precipitate configuration between the aging sets, this result strongly suggests that precipitates are not involved in the micro-mechanism related to the internal driving force. Since precipitates have no significant role in the diffusion-limited mechanism, it is therefore concluded that, in these Al-(1wt%)Cu thin films, the presence of precipitates can not explain the pronounced long-term time-dependent anelastic recovery. If an influence exists, it is clearly limited and not significant.

To unravel the influence of the grain boundary density, the normalized strain evolutions measured with microbeam bending are grouped per aging state and color coded using  $\rho'_{\text{GB}}$  as color weight relative to the specimens within the group, see Fig.6.5. The different plots reveal the spread of the temporal evolution within each group and do not show any systematic influence of  $\rho'_{\text{GB}}$ , i.e. none of the plots show a monotonic increase or decrease in the relaxation time with  $\rho'_{\text{GB}}$ . On the contrary, the effect of  $\rho'_{\text{GB}}$  on the relaxation time appears completely uncorrelated, even though specimens with large differences in grain boundary density were compared, see Fig. 6.2(c). This suggests that grain boundaries do not have an influence on the time-dependent anelastic recovery, i.e. the diffusion-limited

micro-mechanism, controlling the relaxation time, is not related to the presence of grain boundaries.

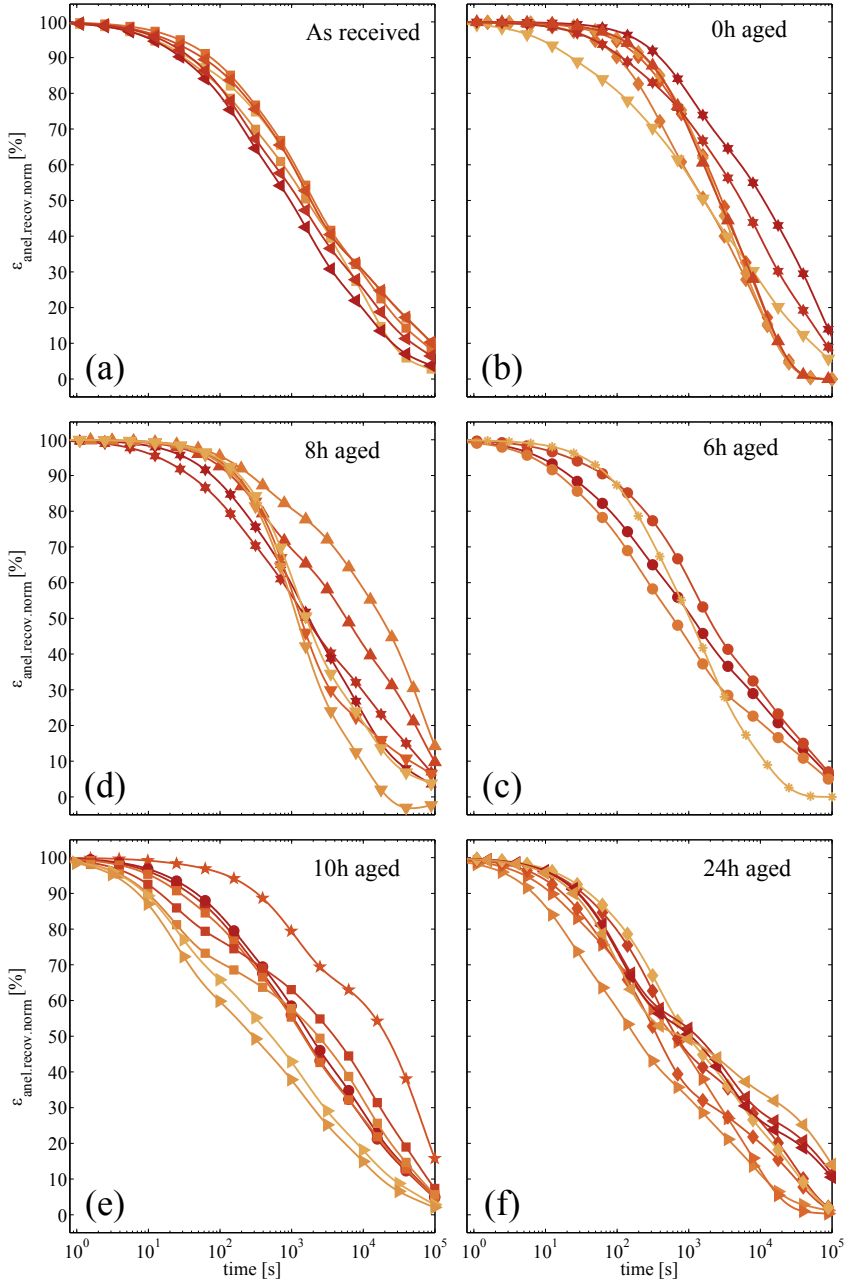


Figure 6.5: Influence of the grain boundary density on the normalized anelastic recovery evolution for specimens (a) as-received and (b) 0 h, (c) 6 h, (d) 8 h, (e) 10 h and (f) 24 hours aged condition. The color intensity (ranging from light orange to dark red) corresponds to the increase in grain boundary density,  $\rho'_{GB}$ .

The effect of the grain boundary density on the amplitude of strain recovery is investigated in Fig.6.6, which shows  $\varepsilon_{\text{anel.recov.}}$  versus  $\varepsilon_{\text{hold.anel.}}$  separately for each aging state, where the color of the symbols denotes its ranking in  $\rho'_{\text{GB}}$  relative within the group. A possible effect of grain boundary density should be visible from a correlation between  $\rho'_{\text{GB}}$  (depicted by the symbol color) and the difference between the data point and the trendline. For instance, one may expect that all data points corresponding to a high  $\rho'_{\text{GB}}$  (i.e. dark red color) always lie above the trend line, and vice versa. However, again, no correlation is observed between this difference and  $\rho'_{\text{GB}}$  for any of the aging states. This indicates that  $\rho'_{\text{GB}}$  does not have a noticeable effect on the value of  $\varepsilon_{\text{anel.recov.}}$ . This is also illustrated in Fig.6.7, which shows that  $\varepsilon_{\text{anel.recov.}}$  normalized by  $\varepsilon_{\text{hold.anel.}}$  is uncorrelated with  $\rho'_{\text{GB}}$ . The inset shows the grain boundary distribution of the two extremes of  $\rho'_{\text{GB}}$  to emphasize that even for the case of almost no grain boundaries, a similar strain ratio is obtained as for specimens with ample grain boundaries. These observations clearly indicate that the internal driving force does not originate from the presence of grain boundaries.

The fact that the internal driving force does not depend on grain boundaries, is consistent with the observation that also the diffusion-limited micro-mechanism seems unrelated to the grain boundary boundary. Therefore, combining the results from Figs. 6.5, 6.7, and 6.6, it may be concluded that the origin for the long-term time-dependent anelastic recovery, in these Al-(1wt%)Cu thin films, is not to be associated with grain boundaries. This does not exclude that grain boundaries may facilitate the underlying mechanism to some extent, but not significant enough for the investigated specimens/materials. It is thus concluded that typical grain boundary mediated mechanisms proposed in the literature, i.e. grain boundary sliding and pinning at triple junctions, and dislocation GB pile-ups, do not play a primary role in the time-dependent anelasticity in these specimens.

## 6.4 Time dependent anelasticity in nano-tensile testing

The question remains which micromechanism could be the cause of the observed time-dependent anelasticity. One option could be polarized dislocation structures due to GNDs formed in bending. Therefore, similar experiments, i.e. prolonged loading for  $10^5$  s, followed by free relaxation, were performed, but this time under uniaxial tension loading, to see the effect of the applied loading state. For this, specimens of length 1052  $\mu\text{m}$ , 10  $\mu\text{m}$  width and 5.3  $\mu\text{m}$  thickness and grain size of 5–7  $\mu\text{m}$  were tested. Fig.6.8(a) shows, for two specimens, the evolution of the strain versus time during the constant force loading period as well as after load removal. In addition, separate plots show the loading and unloading part of the evolution on a logarithmic time scale, see Fig.6.8(b,c). First of all, the evolution of both specimens are nearly identical, which shows that the loading conditions were nearly identical for both specimens. After reaching the elastic strain of 420  $\mu\varepsilon$ , creep occurs up to a creep strain of  $\varepsilon_{\text{creep}} = 90 \mu\varepsilon$  and  $80 \mu\varepsilon$  for specimen S1 and S2, respectively. After load release, both specimens initially show the same amount of elastic recovery of  $\varepsilon_{\text{inst.}} = 420 \mu\varepsilon$ , which is followed by (near) complete time-dependent anelastic recovery of  $\varepsilon_{\text{anel.recov.}} = 60 \mu\varepsilon$  and  $70 \mu\varepsilon$  for specimen S1 and S2, respectively, resulting in a permanent deformation of  $\varepsilon_{\text{perm.}} = 30 \mu\varepsilon$  and  $= 10 \mu\varepsilon$ . Hence, the two specimens reveal a similar anelastic behavior, whereby the differences observed are due to the variations in grain orientation and grain size distribution.

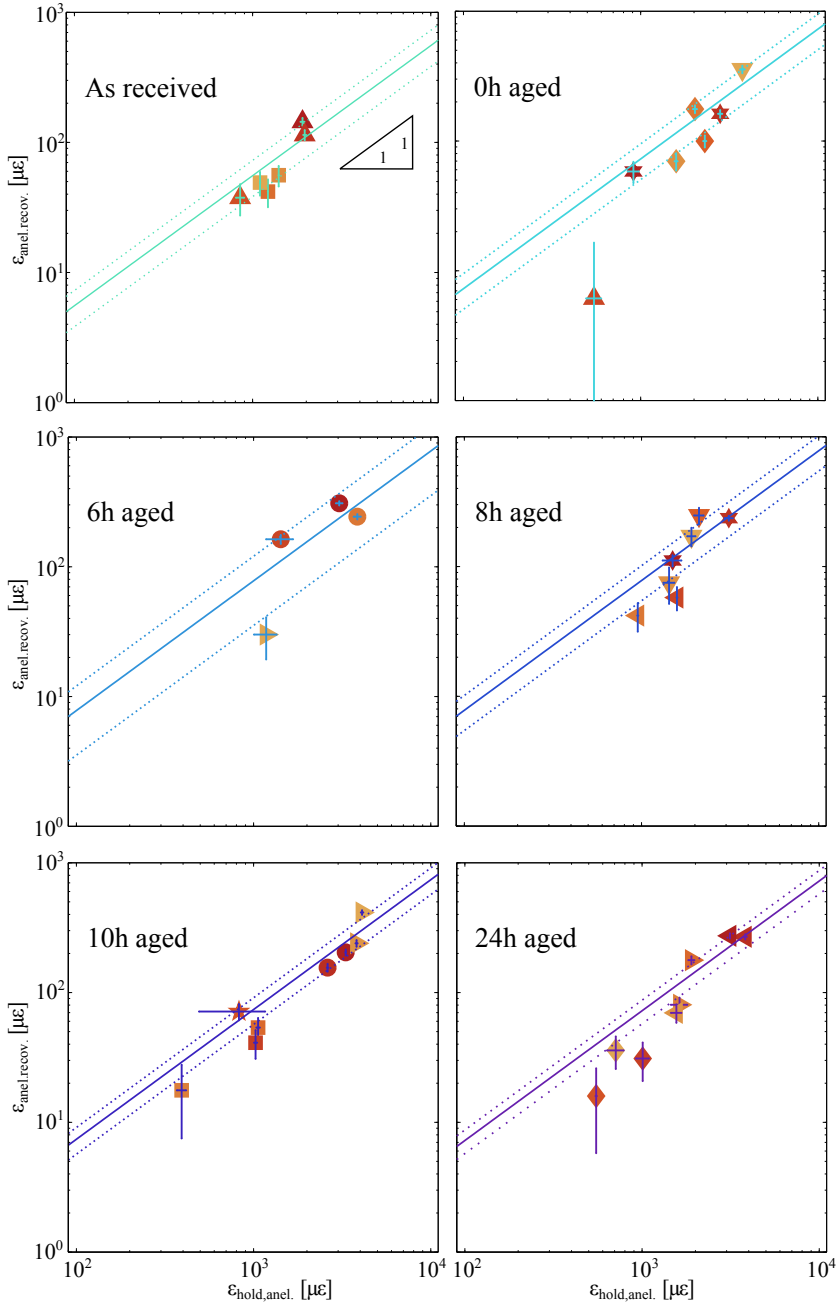


Figure 6.6: Influence of the grain boundary density on the normalized anelastic recovery evolution for specimens (a) as-received and (b) 0 h, (c) 6 h, (d) 8 h, (e) 10 h and (f) 24 hours aged condition. The color intensity of the symbols (ranging from light orange to dark red) corresponds to the increase in grain boundary density,  $\rho'_{\text{GB}}$ .

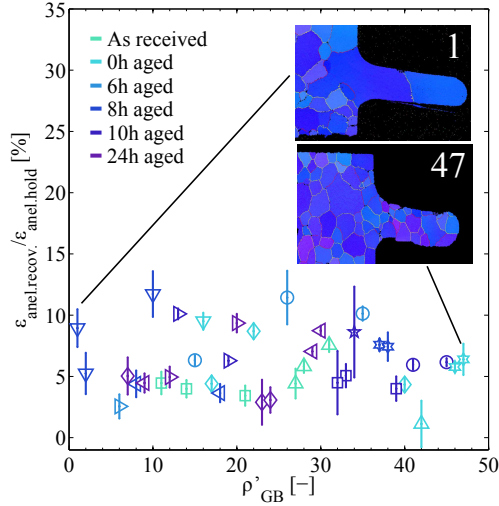


Figure 6.7: The strain ratio as function of weighted GB density,  $\rho'_{\text{GB}}$ . The inset shows a specimen with lowest  $\rho'_{\text{GB}}$  and one with highest  $\rho'_{\text{GB}}$ , which visualizes the large spread in grain boundary density between the tested microbeam specimens.

Interestingly, both micro-tensile specimens show a time-dependent anelastic recovery with a similar relaxation time,  $\approx 1$  day, as observed in the microbeam bending tests. The occurrence of time-dependent anelasticity in both test cases suggests that a bending-induced heterogeneous stress/strain field is not required as an internal driving force. Given that similar relaxation times are observed in bending and uniaxial tension, the same underlying mechanism is expected to be active. Moreover, when comparing Fig.6.8(b) to Fig.6.8(c) a similar time constant is observed as during recovery. Hence, during loading the same (reverse) mechanism as for the anelastic recovery seems to govern the time-dependent behavior. Furthermore, when comparing the behavior during recovery in the tensile test to that in the bending test, a linear  $\log(t)$  relation stands out, whereas the microbeam bending experiments consistently showed a more non-linear  $\log(t)$ . This deviation may result from the difference in loading state. During uniaxial tensile loading the stress is macroscopically uniform over the thickness, which distributes the driving force accordingly throughout the material. In bending, however, the stress magnitude increases with increasing distance from the neutral bending line, which results in a non-linear  $\log(t)$  relation. The time-dependent behavior is triggered only beyond a certain threshold stress and therefore depends nonlinearly on the applied stress. In addition to the microbeam bending showing that grain boundaries and precipitates have no significant role in time-dependent anelasticity, it is concluded that the internal driving force does not stem from a bending-induced heterogeneous stress/strain field.

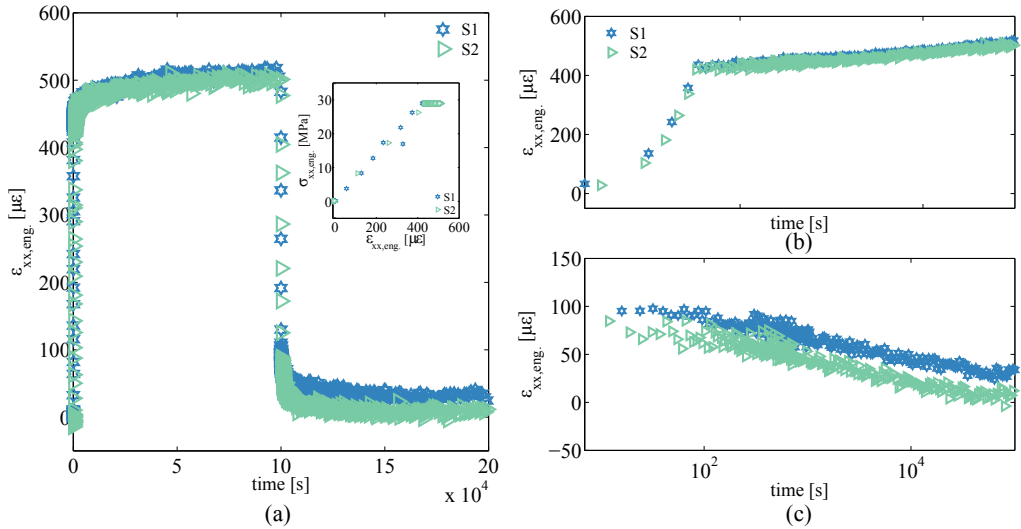


Figure 6.8: Creep and time-dependent anelasticity experiments performed in uniaxial tension on two micro-tensile specimens result in: (a) strain evolution during the experiment with inset showing the corresponding  $\sigma(\epsilon)$  curve; (b) strain evolution during the loading phase emphasizing the creep; (c) strain evolution after load removal showing time-dependent anelasticity.

## 6.5 Possible mechanisms

Up to this point, the micro-mechanical characterization only excluded possible mechanisms in terms of their role in the observed time-dependent anelasticity. Dislocation pile-up and related diffusional mechanisms involving precipitates, grain boundaries, or heterogeneous stress/strain fields appeared to have an insignificant contribution. Although some of these mechanisms are reported to play a role in other thin Al and Al-Ti films [88, 91, 109], these tested materials were thinner, with smaller grains and a different composition compared to the Al-Cu thin film studied here, resulting in shorter time constants on the order of minutes. Therefore the results of the previous sections do not necessarily contradict the previously reported results. The alloying element copper is notably different from the reported materials, which may well influence the time-dependent anelastic recovery. We therefore focus on micromechanisms in which copper solutes may make the difference. A second micromechanism of interest here, is dislocation-dislocation interaction. Although strain levels are low, which likely precludes the formation of pronounced dislocation networks, the strain and stress levels are sufficiently high for dislocation-dislocation interactions to be relevant. This may involve diffusion-limited dislocation climb of segments of edge dislocations [57]. These two mechanisms are explored next.

In general, the mechanical effect of solute atoms can be observed in the plastic strain evolution of a material, e.g., through the Portevin-Le-Chatelier effect, or more generally termed, dynamic strain aging. In this mechanism, solutes drag and pin moving dislocations that flow under applied stress. Dislocations escape in bursts from these solutes, causing jumps in strain. Besides being visible in uniaxial tension experiments, the effects of these

mechanisms have been reported in depth-sensing indentation studies of bulk dilute Al-Cu alloys as strain bursts in the force-displacement curve [27].

Therefore, the nano-indentation hardness measurements, presented in Chapter 5, were re-examined to see if strain bursts in the flow behavior were present. Fig.6.9 shows for each aging state of Al-Cu the force-displacement curves obtained by nano-indentation with a spherical tip,  $d = 250 \mu\text{m}$  up to a maximum force of  $\approx 250 \text{ mN}$ , corresponding to an indentation depth of  $\approx 400 \text{ nm}$ , followed by unloading. At large forces, clear bursts in strain are observed, which are alternated by stages with a smooth gradual force increase. Interestingly, these strain bursts are observed for all aging states. In addition (not shown here), indentations performed using a sharper tip (Berkovich), showed that the transitions between the alternating burst and smooth stages become 'sharper' with decreasing plastic zone size, probably due to the decrease of mobilized dislocations underneath the indenter tip. All indents showed these strain bursts, including indents for which the plastic zone did not contain any grain boundary. Therefore, the strain bursts originate from the grain interior. In fact, the observed strain bursts resemble the Portevin-Le-Chatelier effect reported in the Al-Cu indentation studies in [27].

On the basis of these observations, it is hypothesized that solute copper atoms are also here responsible for dynamic strain aging in the investigated Al-(1wt%)Cu thin films. Furthermore, indentation studies on different dilute Al-Cu alloys have shown that the strain bursts disappear in the presence of GP-zones [26, 27]. Therefore, the occurrence of strain bursts in all heat treated specimens confirms that indeed no (or little) GP-zones are present in the heat treated specimens and, conversely, that a sufficiently large Cu solute concentration is present in all heat treated specimens to significantly affect the glide of dislocations inside the grains. Since the other considered mechanisms did not underlie the time-dependent anelasticity in these films, it is reasonable to assume that diffusing Cu solutes could play a role in the time-dependent anelasticity by pinning and dragging of dislocations.

Further confirmation of the role of Cu and that of dislocation-dislocation interactions can be obtained by performing a similar nano-tensile creep experiment on pure aluminum tensile specimens (99.9% pure Al). Two specimens were tested having  $\approx 1050 \mu\text{m}$  length, width of  $7 \mu\text{m}$ , thickness of  $5.9 \mu\text{m}$  and grain sizes of  $10 - 15 \mu\text{m}$ . These cross-sections differed slightly from the Al-Cu specimens, resulting in slightly higher applied stress levels:  $29.7 \text{ MPa}$  and  $30.2 \text{ MPa}$  for specimen 3 (S3) and, 4 (S4) respectively, compared to  $28.9 \text{ MPa}$  for Al-Cu specimens 1 and 2, see inset of Fig.6.10(a). The strain evolution of the pure Al is depicted next to the data obtained for the Al-Cu specimens in Fig.6.10. After reaching the elastic strain of  $450 \mu\epsilon$  for S3, respectively  $520 \mu\epsilon$  for S4, a large non-saturating creep occurs, amounting to a total creep strain of  $\epsilon_{\text{creep}} = 1235 \mu\epsilon$  and  $1065 \mu\epsilon$  for specimen S3 and S4, respectively. This is much larger than the  $\epsilon_{\text{creep}} = 90 \mu\epsilon$  observed for the Al-Cu specimens. After load release, both specimens show approximately the same amount of elastic recovery as during loading:  $\epsilon_{\text{inst.}} = 495 \mu\epsilon$  for S3 and  $\epsilon_{\text{inst.}} = 478 \mu\epsilon$  for S4. This is followed by time-dependent anelasticity recovery  $\epsilon_{\text{anel.recov.}} = 203 \mu\epsilon$  and  $175 \mu\epsilon$  for specimen S3 and S4, respectively, which remarkably is larger, by a factor of  $\approx 2 - 2.5$ , compared to the Al-Cu specimens. The resulting permanent deformation is  $\epsilon_{\text{perm.}} = 982 \mu\epsilon$  and  $= 936 \mu\epsilon$ .

As in the case of Al-Cu creep tensile tests, here the pure Al specimens show similar in-

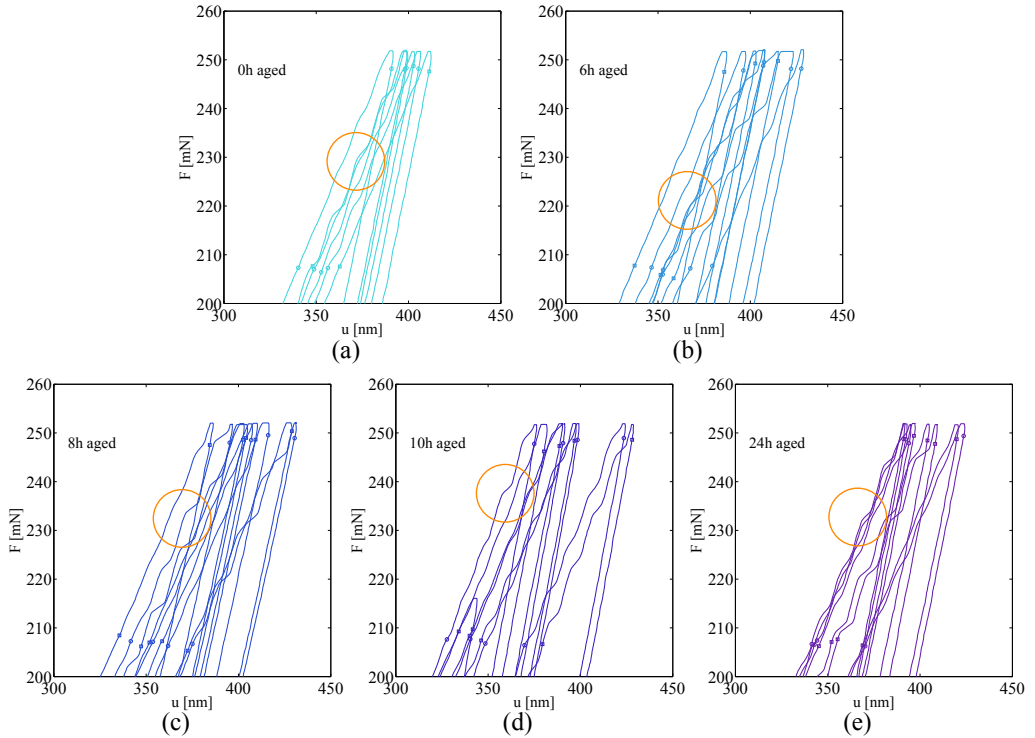


Figure 6.9: Strain bursts in force-displacement measurements, using nano-indentation measurements, indicating dynamic strain aging linked to Cu solutes. Each tested specimen exhibited this behavior.

stantaneous elastic loading and unloading, and a recovery strain. However, the amount of permanent deformation in pure Al is much larger than that observed for Al-Cu specimens, which is due to the precipitation and solute strengthening effect of Al-Cu. Also, the amount of time-dependent anelastic recovery is  $\approx 2 - 2.5$  as much as that observed in the Al-Cu specimens. During loading it is clear that the deformation mechanism in pure Al has completely different time-constant compared to that of the Al-Cu alloy. Remarkably, the time constants involved in the time-dependent anelastic recovery in pure Al and Al-Cu appear nearly identical. This suggests that the same micromechanism contributes to time-dependent anelasticity in the pure Al and Al-Cu specimens, leaving the dislocation-dislocation interactions and dislocation climb of (segments of) edge dislocations as most likely mechanism. The increase of amplitude of anelasticity for pure Al specimens, however, indicates that Cu-solutes might have a secondary role. The mechanism of dislocation-dislocation interactions, and/or dislocation climb of (segments of pinned) dislocations has been reported in high temperature creep and creep-reversal experiments for bulk pure aluminum [64, 65], an aluminum-magnesium alloy [21] and other alloys such as stainless steels [7, 73] or Ti-alloys [48, 49]. In the case of pure Al, *Gibeling* and *Nix* argued that the anelastic recovery is driven by long range back stress resulting from heterogeneous dislocation structures i.e. sub-grains, while limited by thermally activated processes, e.g. cutting or junction unpinning of dislocations in these structures [64, 65]. The suggested



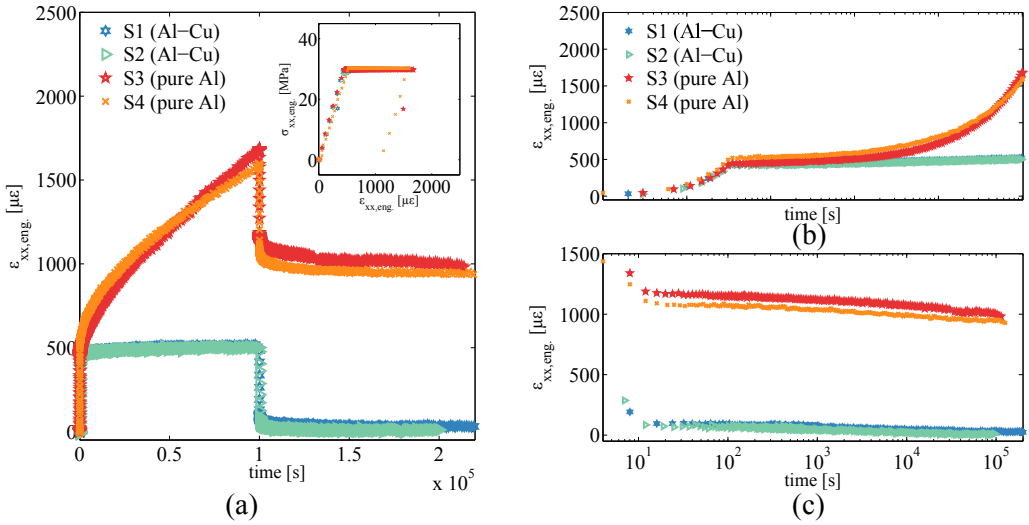


Figure 6.10: Creep and time-dependent anelasticity experiments performed in uniaxial tension on two Al-(1wt%)Cu micro-tensile specimens (S1 and S2) and two pure Al specimens (S3, S4): (a) strain evolution during the experiment with inset showing the corresponding  $\sigma(\epsilon)$  curve; (b) strain evolution during load emphasizing the creep; (c) strain evolution after load removal showing time-dependent anelasticity.

theory discarded diffusion limited climb, because it apparently could not describe multiple deformation rates. Given this discrepancy with results reported here, and the unlikely formation of sub-grain in the Al(-alloy) thin films studied here, their theory likely does not apply here. However, the reports on anelasticity in alloys did suggest that dislocation climb was involved through the (un)bowing of dislocation segments between pinning points, which was driven by the applied stress or the build up line tension, resulting in the anelastic deformation and recovery [7, 21, 48, 49, 73]. Interestingly, the dislocation line tension, and not long range back stresses, were considered as driving force for the recovery. Although none of the above reports provide a conclusive explanation for the observations in this work, they do not exclude that dislocation-dislocation interactions and/or dislocation climb of (segments of pinned) dislocations are responsible.

Perhaps, a plausible hypothesis for the time-dependent recovery may be formulated as follows. During loading, the existing low density dislocation distribution is mobilized and/or dislocation sources are activated. Dislocation-dislocation interactions immobilize dislocations, resulting in distributed pile-ups. Diffusion limited dislocation climb might allow the formation of jogs in these immobilized dislocations: segments of the dislocations climb out of the slip plane thus by-passing the immobile segments. Some of the dislocations escape completely and contribute to permanent plasticity, while others still have long-range interactions with each other. After load removal, back-stresses from these dislocation-dislocation interactions partially reverse the dislocation motion, which likely re-encounter other dislocations. Reverse climb may occur, which is possible if enough time is given, thus finally resulting in partial recovery of the deformation. Cu and its precipitates are expected to play a secondary role. A clear role of Cu solutes is to pin more dislocations, thus reducing the number of mobile dislocations and hence limiting the plastic creep. Possibly

this pinning forms a larger barrier than dislocation-dislocation immobilization, further reducing the dislocations that can escape by climb. To a certain extent the mobile Cu solutes may also diffuse to and pin the surrounding dislocations in the matrix. This might further limit the amount of dislocation climb occurring and thus explain the reduced amplitude in time-dependent recovery for the Al-Cu thin films.

## 6.6 Conclusions

This chapter aimed to unravel the microstructural origin of the time-dependent anelasticity observed in Al-(1wt%)Cu thin films. First, mechanisms related to precipitates and grain boundaries were investigated. Therefore, systematic variations in precipitate state were made through aging heat treatments. The effect of grain boundaries was estimated by qualitatively weighing the grain boundary density with the Von Mises stress magnitude along the beam. Based on this qualitative measure the beams were subsequently compared to each other.

These microstructural effects on time-dependent anelasticity were then evaluated through micromechanical testing. Microbeam bending experiments revealed that precipitates and grain boundaries could not explain the temporal evolution or the amount of time-dependent anelasticity. Additionally, uniaxial tensile creep and anelasticity experiments showed a similar time-dependent anelasticity response in small grained Al-(1wt%)Cu specimens, which precludes heterogeneous deformations as a driving force.

These results strongly suggest that (i) driving forces do not originate from grain boundary sliding mechanisms, strong heterogeneous deformation, i.e. bending, grain boundary induced dislocation pile-ups; (ii) diffusion limited precipitate-dislocation interactions or diffusion in grain boundary sliding are not significant. Nano-indentation experiments on the aged specimens revealed strain bursts, which originate from dislocation pinning and drag by Cu-solutes, i.e. dynamic strain aging. In addition, uniaxial creep and time-dependent anelasticity experiments on pure Al specimens revealed pronounced creep, but similar time-dependent anelastic recovery as for Al-Cu specimens. Hence, it was hypothesized that a dislocation-dislocation based mechanism is most plausible: dislocation-climb in dislocation entanglements. Diffusion-limited dislocation climb may trigger the time-dependent anelasticity through the by-pass of pinned and entangled dislocations. Cu solutes may have a secondary contribution by pinning. The driving force is expected to result from distributed dislocation pile-ups against these pinned and entangled dislocation lines.

## Acknowledgment

The authors acknowledge ing. B.A. Göttgens for his work on the material characterization, microbeam bending and nano-indentation measurements.



# Chapter 7

## Conclusions and recommendations

---

The two goals of this research were to:

1. develop on-wafer mechanical characterization methods suitable for characterizing size-effects in time-dependent anelasticity at the microscale across timescales relevant to MEMS, i.e. from seconds to a day,
2. acquire insights into the underlying physical micro-mechanisms responsible for the time-dependent anelasticity at the  $\mu\text{m}$  length scale.

### 7.1 Methodologies for on-wafer characterization of time-dependent anelasticity

For the first goal two complimentary experimental methodologies were developed that utilize on-wafer specimens: a microbeam bending and nano-tensile testing method. The microbeam bending was capable of controlling the deflection of on-wafer cantilevers with a precision of  $\leq 50$  nm and stability to within 3% of the applied deflection by using a simple, effective microclamp. Careful thermomechanical design of the microclamp eliminated mechanical play and hysteresis in loading, while minimizing thermal expansion errors. Initially confocal optical profilometry combined with simple drift correction through image tracking was sufficient for demonstrating time-dependent anelasticity in microbeam bending up to half a day. However, for measurements up to more than a day, dual wavelength digital holographic microscopy combined with a novel quasi 3D global digital image correlation procedure was required to accurately extract the beam's curvature evolution over the course of a day, yielding a strain resolution of  $\leq 4 \mu\epsilon$ . A simple multi-mode linear visco-elastic model described the time-dependent anelastic behavior adequately based on data obtained from several microbeams deflected to several strain levels for  $10^5$  s. The model also incorporated a plastic element, which enabled a basic characterization of the instantaneous plasticity.

The nano-tensile test allowed full stress and strain control of on-wafer tensile specimens

of various geometries. A high degree of alignment and a minimum of unwanted bending stress have been achieved by (i) an innovative pin-in-hole gripping mechanism with load-centering feature and (ii) sub-mrad angular alignment through a quasi 3D digital image tracking procedure and elastic-hinge manipulators. Multiple load cells with high precision read-out and an original approach to correct background disturbances yielded a range up to 200 mN, a resolution of 70 nN, and a reproducibility exceeding 0.1% full scale range of each respective load cell. An innovative calibration procedure allowed the complete calibration of load cells with stiffness  $\leq 100$  N/m. High reproducibility strain measurements have been achieved by combining high-resolution light microscopy and image tracking of substrate and specimen gauge markers. This yielded a resolution in displacement of  $\sigma_u < 6$  nm, and in strain of  $\sigma_{\varepsilon,xx} < 6 \mu\varepsilon$ . The compact nano-tensile tester in principle enabled in-situ scanning electron microscopy experimentation. Proof of principle measurements of the Young's modulus of 5- $\mu\text{m}$  thick Al-(1wt%)Cu tensile specimens resulted in a value of  $E = 72.6 \pm 3.7$  GPa, illustrating the high precision and reproducibility. Subsequently, time-dependent anelasticity measurements performed during 56 hours revealed a pronounced creep stage, followed by the near-complete time-dependent anelastic recovery of the creep deformation.

In short the developed methodologies were successful at mechanically characterizing the microstrain and sub- $\mu\text{N}$  deformations of on-wafer specimens over timescales of seconds to days. The microfabrication produced a wide array of geometrical variations in the specimens, which enables the analysis of size-effects in time-dependent anelasticity.

## 7.2 Insights into the underlying physical micromechanisms

To obtain insights into the underlying micromechanisms, systematic variations were made to the microstructure and measured through nano-indentation, high-resolution transmission electron microscopy (HRTEM), scanning electron microscopy (SEM), electron backscatter diffraction (EBSD), wide angle X-ray diffraction (WAXD) and energy dispersive spectroscopy (EDS). The precipitate state was varied from the as-received state through a homogenizing solid-solution heat treatment at 550 °C followed by aging heat treatments at 190 °C up to 24 hours. The influence on the time-dependent anelasticity was measured using the microbeam bending methodology and the nano-tensile test. The following conclusions resulted:

The as-received state contained Cu that was mostly clustered in GP-zones and in some  $\theta$ -precipitates mainly at grain boundaries, while a significant amount of dislocations were present. With aging duration the  $\theta$  phase precipitates less in the thin film interior and more at the surface and more specifically at grain boundary grooves. Further characterization of the microstructure revealed an absence of  $\theta'$  precipitates for all aging states. Additionally, the applied aging resulted in a slight increase in hardness, followed by a decrease and subsequent slight increase up to a saturation level. Large variations were present in the precipitate state, i.e. GP-zones, solid-solution, small dispersed precipitates, large precipitates at grain boundary grooves and surface, and a variable grain boundary structure, ranging from one or two grains to many in the stress affected region. Despite these large

variations, the time-dependent anelasticity in microbeam bending was observed to be unaffected by these variations: there was no discernible effect on the temporal evolution or the amplitude of the anelastic strain measured after load removal. Furthermore, uniaxial tensile loading and bending loading revealed nearly equal time scales involved in the time-dependent anelasticity, indicating that the heterogeneous loading state does not contribute to the driving force of the anelasticity. Nano-indentation revealed strain bursts during loading for all heat treated states, which were related to dynamic strain aging affected by Cu-solutes. Finally, uniaxial tensile loading of pure aluminum specimens revealed similar time-dependent anelastic recovery as compared to the Al-Cu specimens, though of larger amplitude.

Due to the long time-scales involved, a diffusion limiting mechanism is believed to be responsible for the time-dependent anelasticity. Further, given that the anelastic recovery occurs after complete load removal, a driving force that reverses the dislocation motion, such as back stresses from dislocation-dislocation interactions, is believed to be present. Based on these observations the following hypotheses were proposed:

1. The absence of  $\theta'$  originates from the preferred precipitation of  $\theta$  at grain boundary grooves and free surface locations, because these are energetically favorable: a greater reduction of the material system energy is possible at these locations as opposed to precipitation in the thin film interior.
2. The hardness evolution results from the slight initial increase of  $\theta$  precipitates in the interior, followed by a decrease of the hardness due to preferential  $\theta$  growth at grain boundary grooves and the free surface, which weakens the thin film interior. Further aging grows the surface precipitates and increases the surface strength, thus posing a stronger barrier to dislocation motion and increasing the hardness.
3. The observations that neither grain boundaries nor the presence of copper (precipitates) have an influence on the temporal evolution of the time-dependent anelasticity strongly suggest that a diffusion-limited dislocation mechanism is active, independent from the presence of copper (precipitates) and grain boundaries. It is expected that dislocation climb contributes through the by-pass of pinned segments of edge dislocations.
4. The observations that neither grain boundaries, precipitates, nor strong heterogeneous deformations, have an influence on the amount of time-dependent anelasticity, suggest that the driving force is based on dislocation-dislocation interactions: distributed dislocation pile-ups against pinned and entangled dislocation segments. Possibly, the presence of copper (precipitates) plays a secondary role, by increasing the amount of pinned dislocations.

## 7.3 Recommendations

Several recommendations for further research are proposed.

- Ideally an in-situ TEM experiment would give more insights into the driving forces and diffusion-limited mechanisms underlying the time-dependent anelasticity. This might be done with an in-situ straining stage or a pico indenter where a fixed load or displacement/deflection of a Al-Cu specimen is performed. Observations of dis-

location state and chemical composition before, during and after loading would be desired in regions where the dislocations would pile up.

- Further substantiation of the role of Cu-solutes in time-dependent anelasticity could be investigated numerically. Firstly, atomistic simulations could be employed that take into account the diffusion of Cu-solutes and the Cu-dislocation interactions. Based on these findings, a numeric implementation in a strain gradient crystal plasticity model [47] could be extended to simulate the MEMS behavior.
- A numerical study of the Cu-diffusion and precipitation behavior for these thin films might be conducted to test the hypothesis on the observed precipitation behavior.
- Conducting (time-dependent) mechanical experiments at various temperatures and stresses will allow for the characterization of activation energies and threshold stresses involved in the deformation mechanisms offering a more quantitative understanding of the active micromechanisms in thin film mechanics. The nano-tensile tester is also equipped with a heating element for elevated temperature testing up to 150 °C and is therefore well suited for these experiments.
- To advance the understanding of plasticity in alloys, size-effects related to plastic behavior at shorter time scales as well as other plasticity mechanisms may also be studied for these Al-Cu alloy thin films. The available variations in geometry and the use of in-situ electron microscopy with the nano-tensile tester offers ample opportunities: dislocation-grain boundary interactions, precipitate phase and size influences, size-effects of grain size, size-effects of surface-to-volume ratios, grain orientation effects.
- The nano-tensile tester may be employed to study microscale mechanics of other materials: interfaces in multi-phase materials, e.g. dual phase steel, the effect of passivation layers in thin metal films, e.g. pure Al vs. pure Au. Depending on the possibility of integrating the material of interest into the current microfabrication scheme, alternative specimen fabrication routes should be explored, e.g. (focussed) ion beam milling. These routines should take into account the limitations imposed by the nano-tensile test, to enable the alignment and strain measurement.
- Single crystal studies could be conducted to exclude grain boundary effects and further substantiate the results presented in Chapter 6. However, creating single crystal specimens by thin film deposition techniques requires special growth methods [90, 138, 168]. Alternatively, laser-assisted recrystallization techniques might be employed to locally recrystallize as-received structures [8] as demonstrated in Al-interconnects [79]. Although it is not a widely adopted technique, it might offer novel MEMS-fabrication routes to control thin film properties in the stages after deposition, lithography and etching.
- The successful application of the microbeam bending and nano-tensile testing methodologies to on-wafer specimens also benefits the research and development loop of the actual MEMS. Test specimens can be co-fabricated with test-wafers of the actual MEMS and the mechanical behavior can be directly characterized. Specifically, the microbeam bending methodology is suitable for adoption in an industrial R&D environment, due to the limited amount of customized hardware involved, i.e. the microclamp is a cheap simple part, profilometers are available in MEMS R&D labs and non-proprietary software is involved.
- It would be interesting to further improve and validate the multi-mode visco-elasticity model. A 3D implementation of the obtained parameters in a finite element model of an actual device could be compared to an experimentally measured response of

that device. This would clearly underline the utility of the microbeam bending methodology in MEMS research and development.

- The presented model could be combined with integrated digital image correlation (IDIC) to improve the parameter estimation. IDIC is a novel advanced integrated parameter identification technique. Instead of simply using global digital image correlation to extract deformations from profile to profile over the course of time, integrated digital image correlation would combine the mechanical model and the entire sequence of profiles to directly extract the material parameters. This has the benefit of extending the number of data points and reducing the number of degrees of freedom in the correlation routine, making it more robust and improving the accuracy of the parameters.





# References

---

- [1] R. Artigas, *Optical Measurement of Surface Topography*. Berlin, Germany: Springer-Verlag Berlin Heidelberg, 2011, ch. Imaging Confocal Microscopy, pp. 237–286.
- [2] E. Arzt, “Size effects in materials due to microstructural and dimensional constraints: A comparative review,” *Acta Mater.*, vol. 46, no. 16, pp. 5611–5626, 1998.
- [3] E. Arzt, G. Dehm, P. Gumbsch, O. Kraft, and D. Weiss, “Interface controlled plasticity in metals: Dispersion hardening and thin film deformation,” *Progr. Mater. Sci.*, vol. 46, no. 3-4, pp. 283–307, 2001.
- [4] S. P. Baker, R. P. Vinci, and T. Arias, “Elastic and anelastic behavior of materials in small dimensions,” *MRS Bull.*, vol. 27, no. 1, pp. 26–29+13, 2002.
- [5] N. I. Barbosa, R. R. Keller, D. T. Read, R. H. Geiss, and R. Vinci, “Comparison of electrical and microtensile evaluations of mechanical properties of an aluminum film,” *Metall. Mat. Trans. A*, vol. 38 A, no. 13, pp. 2160–2167, 2007.
- [6] M. Baumgärtel and H. H. Winter, “Interrelation between continuous and discrete relaxation time spectra,” *J. Non-Newton. Fluid.*, vol. 44, pp. 15–36, 1992.
- [7] W. Beere and I. G. Crossland, “Primary and recoverable creep in 20/25 stainless steel,” *Acta Metall.*, vol. 30, no. 10, pp. 1891–1899, 1982.
- [8] Y. Bellouard, T. Lehnert, J. Bidaux, T. Sidler, R. Clavel, and R. Gotthardt, “Local annealing of complex mechanical devices: a new approach for developing monolithic micro-devices,” *Mater. Sci. Eng. A*, vol. 273-275, pp. 795 – 798, 1999.
- [9] L. I. J. C. Bergers, J. P. M. Hoefnagels, N. K. R. Delhey, and M. G. D. Geers, “Measuring time-dependent deformations in metallic MEMS,” *Microelectron. Reliab.*, vol. 51, no. 6, pp. 1054–1059, 2011.
- [10] L. I. J. C. Bergers, J. P. M. Hoefnagels, and M. G. D. Geers, “Characterizing time-dependent anelastic microbeam bending mechanics,” *J. Micromech. Microeng.*, p. in preparation, 2013.

- [11] L. I. J. C. Bergers, J. Neggers, M. G. D. Geers, and J. P. M. Hoefnagels, "Enhanced global digital image correlation for accurate measurement of microbeam bending," in *Adv. Mater. Model. Struct.*, ser. Advanced Structured Materials, H. Altenbach and S. Kruch, Eds. Springer Berlin Heidelberg, 2013, vol. 19, pp. 43–51.
- [12] G. Besnard, F. Hild, and S. Roux, "'Finite-element' displacement fields analysis from digital images: Application to Portevin-Le-Châtelier bands," *Exp. Mech.*, vol. 46, no. 6, pp. 789–803, 2006.
- [13] B. Bhushan and X. Li, "Nanomechanical characterisation of solid surfaces and thin films," *Int. Mater. Rev.*, vol. 48, no. 3, pp. 125–164, 2003.
- [14] J. A. Bielen, J. Stulemeijer, D. Ganjoo, D. Ostergaard, and S. Noijen, "Fluid-electrostatic-mechanical modeling of the dynamic response of RF-MEMS capacitive switches," in *EuroSime 2008: Int. Conf. Thermal, Mechanical and Multi-Physics Simulation Experiments in Microelectronics and Micro-Systems*, 2008, p. 4525083.
- [15] H. G. Bohn, M. Prieler, C. M. Su, H. Trinkaus, and W. Schilling, "Internal friction effects due to grain boundary sliding in large- and small-grained aluminium," *J. Phys. Chem. Sol.*, vol. 55, no. 10, pp. 1157–1164, 1994.
- [16] A. Bosseboeuf and S. Petitgrand, "Characterization of the static and dynamic behaviour of M(O)EMS by optical techniques: Status and trends," *J. Micromech. Microeng.*, vol. 13, no. 4, pp. S23–S33, 2003.
- [17] J. Bressers, S. Holdsworth, P. Harris, C. Larsen, M. Sanders, M. Steen, and G. Tjoa, *A code of practice for the measurement of misalignment induced bending in uniaxially loaded tension-compression test pieces*. E.C. Institute of Adv. Mater., Petten Site, 1995.
- [18] A. J. Brock and M. J. Pryor, "The kinetics of the oxidation of aluminumcopper alloys in oxygen at high temperature," *Corros. Sci.*, vol. 13, no. 3, pp. 199 – 227, 1973.
- [19] F. R. Brotzen, C. T. Rosenmayer, C. G. Cofer, and R. J. Gale, "Creep of thin metallic films," *Vacuum*, vol. 41, no. 4-6, pp. 1287–1290, 1990.
- [20] T. E. Buchheit, S. J. Glass, J. R. Sullivan, S. S. Mani, D. A. Lavan, T. A. Friedmann, and R. Janek, "Micromechanical testing of MEMS materials," *J. Mater. Sci.*, vol. 38, no. 20, pp. 4081–4086, 2003.
- [21] L. O. Bueno and R. L. Bell, "Anelastic creep behaviour of RR-58 aluminum alloy at 180 °C: Phenomenological aspects and analysis based on the unbowing of dislocation segments," *Mater. Sci. Eng. A*, vol. 410-411, no. 0, pp. 72 – 78, 2005.
- [22] V. Burg, J. M. J. Den Toonder, A. Van Dijken, J. P. M. Hoefnagels, and M. G. D. Geers, "Characterization method for mechanical properties of thin freestanding metal films for RF-MEMS," in *EuroSime 2006: Int. Conf. Thermal, Mechanical and Multi-Physics Simulation Experiments in Microelectronics and Micro-Systems*, 2006, pp. 1–7.

- 
- [23] F. Cacchione, A. Corigliano, B. De Masi, and C. Riva, "Out of plane vs in plane flexural behaviour of thin polysilicon films: Mechanical characterization and application of the weibull approach," *Microelectron. Reliab.*, vol. 45, no. 9-11, pp. 1758–1763, 2005.
- [24] F. Cacchione, A. Corigliano, B. De Masi, and M. Ferrera, "Out of plane flexural behaviour of thin polysilicon films: Mechanical characterization and application of the weibull approach," *Sens. Lett.*, vol. 4, no. 2, pp. 184–190, 2006.
- [25] I. Chasiotis and W. G. Knauss, "A new microtensile tester for the study of MEMS materials with the aid of atomic force microscopy," *Exp. Mech.*, vol. 42, no. 1, pp. 51–57, 2002.
- [26] N. Q. Chinh, F. F. Csikor, and J. Lendvai, "Influence of Guinier-Preston zone formation on plastic instabilities in depth sensing indentation tests," *Mater. Sci. Forum*, vol. 331–337 II, pp. 1007–1012, 2000.
- [27] N. Q. Chinh, J. Gubicza, Z. Kovács, and J. Lendvai, "Depth-sensing indentation tests in studying plastic instabilities," *J. Mater. Res.*, vol. 19, no. 1, pp. 31–45, 2004.
- [28] D. H. Choi and W. D. Nix, "Anelastic behavior of copper thin films on silicon substrates: Damping associated with dislocations," *Acta Mater.*, vol. 54, no. 3, pp. 679–687, 2006.
- [29] D. H. Choi, H. Kim, and W. D. Nix, "Anelasticity and damping of thin aluminum films on silicon substrates," *J. Microelectromech. Syst.*, vol. 13, no. 2, pp. 230–237, 2004.
- [30] B. W. Christ, "Effects of misalignment on the pre-macroyield region of the uniaxial stress-strain curve," *Metall. Trans.*, vol. 4, no. 8, pp. 1961–1965, 1973.
- [31] K. H. Chung, S. Scholz, G. A. Shaw, J. A. Kramar, and J. R. Pratt, "Si traceable calibration of an instrumented indentation sensor spring constant using electrostatic force," *Rev. Sci. Instrum.*, vol. 79, no. 9, 2008.
- [32] E. Collin, J. Kofler, S. Lakhroufi, S. Pairis, Y. Bunkov, and H. Godfrin, "Metallic coatings of microelectromechanical structures at low temperatures: Stress, elasticity, and nonlinear dissipation," *J. Appl. Phys.*, vol. 107, no. 11, p. 114905, 2010.
- [33] T. Connolley, P. E. Mchugh, and M. Bruzzi, "A review of deformation and fatigue of metals at small size scales," *Fatigue Fract. Eng. Mater. Struct.*, vol. 28, no. 12, pp. 1119–1152, 2005.
- [34] A. Corigliano, F. Cacchione, B. De Masi, and C. Riva, "On-chip electrostatically actuated bending tests for the mechanical characterization of polysilicon at the micro scale," *Meccanica*, vol. 40, no. 4-6 SPEC. ISS., pp. 485–503, 2005.
- [35] M. Coulombier, G. Guisbiers, M.-S. Colla, R. Vayrette, J.-P. Raskin, and T. Pardoën, "On-chip stress relaxation testing method for freestanding thin film materials," *Rev. Sci. Instrum.*, vol. 83, no. 10, 2012.
- [36] E. Cuhe, F. Bevilacqua, and C. Depeursinge, "Digital holography for quantitative phase-contrast imaging," *Opt. Lett.*, vol. 24, no. 5, pp. 291–293, 1999.

- [37] E. Cuche, P. Marquet, and C. Depeursinge, “Simultaneous amplitude-contrast and quantitative phase-contrast microscopy by numerical reconstruction of fresnel off-axis holograms,” *Appl. Opt.*, vol. 38, no. 34, pp. 6994–7001, 1999.
- [38] G. Dehm, “Miniaturized single-crystalline fcc metals deformed in tension: New insights in size-dependent plasticity,” *Progr. Mater. Sci.*, vol. 54, no. 6, pp. 664 – 688, 2009.
- [39] G. Dehm, C. Motz, C. Scheu, H. Clemens, P. H. Mayrhofer, and C. Mitterer, “Mechanical size-effects in miniaturized and bulk materials,” *Adv. Eng. Mater.*, vol. 8, no. 11, pp. 1033–1045, 2006.
- [40] E. Demir and D. Raabe, “Mechanical and microstructural single-crystal Bauschinger effects: Observation of reversible plasticity in copper during bending,” *Acta Mater.*, vol. 58, no. 18, pp. 6055 – 6063, 2010.
- [41] J. M. J. Den Toonder and A. R. Van Dijken, “Optimization of mechanical properties of thin free-standing metal films for RF-MEMS,” in *Mater. Res. Soc. Symp. Proc.*, ser. Nanoengineered Assemblies and Advanced Micro/Nanosystems, J. L. et al., Ed., vol. 820, 2004, pp. 177–182.
- [42] F. M. d’Heurle, “The effect of copper additions on electromigration in aluminum thin films,” *Metall. Trans.*, vol. 2, no. 3, pp. 683–689, 1971.
- [43] A. G. Dirks and J. J. Van Den Broek, “ $\theta$ -Al<sub>2</sub>Cu formation at room temperature in metastable Al-Cu alloy films,” *Acta Metall.*, vol. 37, no. 1, pp. 9 – 15, 1989.
- [44] M. R. Douglas, “Lifetime estimates and unique failure mechanisms for a digital micromirror device,” in *Proc. Int. Reliab. Phys. Symp.*, 1998, pp. 9–16.
- [45] C. Eberl, “Digital image correlation and tracking - a free matlab code,” <http://www.mathworks.nl/matlabcentral/fileexchange/12413>, Jan. 2010. [Online]. Available: <http://www.mathworks.nl/matlabcentral/fileexchange/12413>
- [46] C. Eberl, D. S. Gianola, and K. J. Hemker, “Mechanical characterization of coatings using microbeam bending and digital image correlation techniques,” *Exp. Mech.*, vol. 50, no. 1, pp. 85–97, 2010.
- [47] I. Ertürk, K. Gao, J. A. Bielen, J. A. W. Van Dommelen, and M. G. D. Geers, “Crystal plasticity based modeling of time and scale dependent behavior of thin films,” *GAMM-Mitteilungen*, vol. 36, pp. 161–185, 2013.
- [48] M. Es-Souni, “Primary and anelastic creep of a near  $\alpha$ -Ti alloy and their dependencies on stress and temperature,” *Mech. Time-Dep. Mater.*, vol. 2, no. 3, pp. 211–228, 1998.
- [49] M. Es-Souni, “Primary, secondary and anelastic creep of a high temperature near  $\alpha$ -Ti alloy Ti6242Si,” *Mater. Charact.*, vol. 45, no. 2, pp. 153 – 164, 2000.
- [50] D. Fabrègue, N. André, M. Coulombier, J. P. Raskin, and T. Pardoën, “Multipurpose nanomechanical testing machines revealing the size-dependent strength and high ductility of pure aluminium submicron films,” *Micro. Nano. Lett.*, vol. 2, no. 1, pp. 13–16, 2007.

- 
- [51] Femtotools AG., “Ft-fs10000 mechanical probe,” <http://www.femtotools.com>, Jan. 2010. [Online]. Available: <http://www.femtotools.com>
- [52] R. Fenner, *Mechanics of Solids*. Boca Raton, FLorida, USA: CRC Press LLC, 1999.
- [53] J. N. Florando and W. D. Nix, “A microbeam bending method for studying stress-strain relations for metal thin films on silicon substrates,” *J. Mech. Phys. Solids*, vol. 53, no. 3, pp. 619–638, 2005.
- [54] J. A. Floro, E. Chason, R. C. Cammarata, and D. J. Srolovitz, “Physical origins of intrinsic stresses in Volmer-Weber thin films,” *MRS Bull.*, vol. 27, no. 1, pp. 19–25, 2002.
- [55] D. R. Frear, J. E. Sanchez, A. D. Romig, and J. W. Morris, “The evolution of microstructure in Al-2%Cu thin films: Precipitation, dissolution, and reprecipitation,” *Metal. Trans. A*, vol. 21, no. 9, pp. 2449–2458, 1990.
- [56] L. B. Freund and S. Suresh, *Thin Film Materials: stress, defect formation and surface evolution*, 1st ed. Cambridge, UK: Cambridge University Press, 2003.
- [57] J. Friedl, *Dislocations*, 1st ed. Oxford: Pergamon Press LTD, 1964.
- [58] J. Gaspar, M. E. Schmidt, J. Held, and O. Paul, “Wafer-scale microtensile testing of thin films,” *J. Microelectromech. Syst.*, vol. 18, pp. 1062 – 1076, 2009.
- [59] J. Gass, A. Dakoff, and M. K. Kim, “Phase imaging without  $2\pi$  ambiguity by multiwavelength digital holography,” *Opt. Lett.*, vol. 28, no. 13, pp. 1141–1143, 2003.
- [60] R. S. Gates and J. R. Pratt, “Prototype cantilevers for si-traceable nanonewton force calibration,” *Meas. Sci. Tech.*, vol. 17, no. 10, pp. 2852–2860, 2006.
- [61] F. W. Gayle and M. Goodway, “Precipitation hardening in the first aerospace aluminum alloy: The Wright flyer crankcase,” *Science*, vol. 266, no. 5187, pp. 1015–1017, 1994.
- [62] M. G. D. Geers, W. A. M. Brekelmans, and P. J. M. Janssen, “Size effects in miniaturized polycrystalline fcc samples: Strengthening versus weakening,” *Int. J. Solids Struct.*, vol. 43, no. 24, pp. 7304–7321, 2006.
- [63] D. S. Gianola and C. Eberl, “Micro- and nanoscale tensile testing of materials,” *JOM*, vol. 61, no. 3, pp. 24–35, 2009.
- [64] J. C. Gibeling, “A phenomenological description of creep transients based on anelasticity,” *Acta Metall.*, vol. 37, no. 12, pp. 3183 – 3193, 1989.
- [65] J. C. Gibeling and W. D. Nix, “Observations of anelastic backflow following stress reductions during creep of pure metals,” *Acta Metall.*, vol. 29, no. 10, pp. 1769–1784, 1981.
- [66] J. J. Y. Gill, L. V. Ngo, P. R. Nelson, and C. J. Kim, “Elimination of extra spring effect at the step-up anchor of surface-micromachined structure,” *J. Microelectromech. Syst.*, vol. 7, no. 1, pp. 114–121, 1998.

- [67] J. R. Greer and J. T. M. De Hosson, “Plasticity in small-sized metallic systems: Intrinsic versus extrinsic size effect,” *Prog. Mater. Sci.*, vol. 56, no. 6, pp. 654–724, 2011.
- [68] J. R. Greer, W. C. Oliver, and W. D. Nix, “Size dependence of mechanical properties of gold at the micron scale in the absence of strain gradients,” *Acta Mater.*, vol. 53, no. 6, pp. 1821–1830, 2005.
- [69] H. Guckel, D. Burns, C. Rutigliano, E. Lovell, and B. Choi, “Diagnostic microstructures for the measurement of intrinsic strain in thin films,” *J. Micromech. Microeng.*, vol. 2, no. 2, pp. 86–95, 1992.
- [70] G. Guisbiers and L. Buchaillet, “Size and shape effects on creep and diffusion at the nanoscale,” *Nanotechnology*, vol. 19, no. 43, 2008.
- [71] G. Guisbiers, M.-S. Colla, M. Coulombier, J. P. Raskin, and T. Pardoen, “Study of creep/relaxation mechanisms in thin freestanding nanocrystalline palladium films through the lab-on-chip technology,” *J. Appl. Phys.*, vol. 113, no. 2, 2013.
- [72] P. Haassen, *Physical Metallurgy*, 3rd ed. Cambridge: Cambridge University Press, 1996.
- [73] E. Hajná, V. Šustek, and J. Čadek, “Creep and anelasticity in a 21Cr37Ni austenitic stainless steel at a constant homogeneous dislocation structure,” *Mater. Sci. Eng.*, vol. 82, no. C, pp. 1–11, 1986.
- [74] J. H. Han and M. T. A. Saif, “In situ microtensile stage for electromechanical characterization of nanoscale freestanding films,” *Rev. Sci. Instrum.*, vol. 77, no. 4, 2006.
- [75] M. A. Haque and M. T. A. Saif, “Mechanical behavior of 30-50 nm thick aluminum films under uniaxial tension,” *Scripta Mater.*, vol. 47, no. 12, pp. 863–867, 2002.
- [76] M. A. Haque and M. T. A. Saif, “Microscale materials testing using MEMS actuators,” *J. Microelectromech. Syst.*, vol. 10, no. 1, pp. 146–152, 2001.
- [77] M. A. Haque and M. T. A. Saif, “A review of MEMS-based microscale and nanoscale tensile and bending testing,” *Exp. Mech.*, vol. 43, no. 3, pp. 248–255, 2003.
- [78] A. L. Hartzell, M. G. da Silva, and H. R. Shea, *MEMS Reliability*. Springer Science+Business Media, LLC, Boston USA, 2011.
- [79] C. S. Hau-Riege and C. V. Thompson, “Microstructural evolution induced by scanned laser annealing in Al interconnects,” *Appl. Phys. Lett.*, vol. 75, no. 10, pp. 1464–1466, 1999.
- [80] S. S. Hazra, M. S. Baker, J. L. Beuth, and M. P. de Boer, “Demonstration of an in situ on-chip tensile tester,” *J. Micromech. Microeng.*, vol. 19, no. 8, 2009.
- [81] K. J. Hemker and W. N. Sharpe Jr., “Microscale characterization of mechanical properties,” *Ann. Rev. Mater. Res.*, vol. 37, pp. 92–126, 2007.
- [82] C. Hierold, “From micro- to nanosystems: mechanical sensors go nano,” *J. Micromech. Microeng.*, vol. 14, no. 9, p. S1, 2004.

- 
- [83] F. Hild and S. Roux, “Digital image correlation: From displacement measurement to identification of elastic properties - a review,” *Strain*, vol. 42, no. 2, pp. 69–80, 2006.
- [84] F. Hild and S. Roux, “Comparison of local and global approaches to digital image correlation,” *Exp. Mech.*, vol. 52, pp. 1503–1519, 2012.
- [85] H. Hirakata, N. Fukuhara, S. Ajioka, A. Yonezu, M. Sakihara, and K. Minoshima, “The effect of thickness on the steady-state creep properties of freestanding aluminum nano-films,” *Acta Mater.*, vol. 60, no. 11, pp. 4438 – 4447, 2012.
- [86] E. Hornbogen, “Hundred years of precipitation hardening,” *J. Light Metals*, vol. 1, no. 2, pp. 127 – 132, 2001.
- [87] S. Hyun, W. L. Brown, and R. P. Vinci, “Thickness and temperature dependence of stress relaxation in nanoscale aluminum films,” *Appl. Phys. Lett.*, vol. 83, no. 21, pp. 4411–4413, 2003.
- [88] S. Hyun, T. K. Hooghan, W. L. Brown, and R. P. Vinci, “Linear viscoelasticity in aluminum thin films,” *Appl. Phys. Lett.*, vol. 87, no. 6, pp. 1–3, 2005.
- [89] T. S. J. A. Rogers and Y. Huang, “Materials and mechanics for stretchable electronics,” *Science*, vol. 327, no. 5973, pp. 1603–1607, 2010.
- [90] A. Jankowski and J. Hayes, “The evaporative deposition of aluminum coatings and shapes with grain size control,” *Thin Solid Films*, vol. 447–448, pp. 568–574, 2004.
- [91] A. J. Kalkman, A. H. Verbruggen, and G. C. A. M. Janssen, “Young’s modulus measurements and grain boundary sliding in free-standing thin metal films,” *Appl. Phys. Lett.*, vol. 78, no. 18, pp. 2673–2675, 2001.
- [92] A. J. Kalkman, A. H. Verbruggen, and S. Radelaar, “High-temperature tensile tests and activation volume measurement of free-standing submicron Al films,” *J. Appl. Phys.*, vol. 92, no. 11, pp. 6612–6615, 2002.
- [93] A. J. Kalkman, A. H. Verbruggen, and G. C. A. M. Janssen, “High-temperature bulge-test setup for mechanical testing of free-standing thin films,” *Rev. Sci. Instrum.*, vol. 74, no. 3, pp. 1383–1385, 2003.
- [94] D. J. Kang, J. H. Park, M. S. Shin, J. E. Ha, and H. J. Lee, “Specimen alignment in an axial tensile test of thin films using direct imaging and its influence on the mechanical properties of BeCu,” *J. Micromech. Microeng.*, vol. 20, no. 8, 2010.
- [95] W. Kang and M. T. A. Saif, “A novel method for in situ uniaxial tests at the micro/nano scalepart I: Theory,” *J. Microelectromech. Syst.*, vol. 19, no. 6, pp. 1309–1321, 2010.
- [96] W. Kang, J. H. Han, and M. T. A. Saif, “A novel method for in situ uniaxial tests at the micro/nanoscalepart II: Experiment,” *J. Microelectromech. Syst.*, vol. 19, no. 6, pp. 1322–1330, 2010.
- [97] T.-S. Kê, “Anomalous internal friction associated with the precipitation of copper in cold-worked Al-Cu alloys,” *Phys. Rev.*, vol. 78, no. 4, pp. 420–423, 1950.



- [98] D. Kiener, W. Grosinger, G. Dehm, and R. Pippan, "A further step towards an understanding of size-dependent crystal plasticity: In situ tension experiments of miniaturized single-crystal copper samples," *Acta Mater.*, vol. 56, no. 3, pp. 580–592, 2008.
- [99] D.-H. Kim, M.-W. Kim, J.-W. Jeon, K.-S. Lim, and J.-B. Yoon, "Mechanical reliability of a digital micromirror with interdigitated cantilevers," *J. Microelectromech. Syst.*, vol. 19, no. 5, pp. 1197–1206, 2010.
- [100] M. K. Kim, "Principles and techniques of digital holographic microscopy," *J. Photon. Energy*, pp. 018005–018005, 2010.
- [101] S. W. Kim, C. S. Oh, and H. J. Lee, "Specimen aligning techniques in tensile and fatigue tests for thin films," *Fatigue Fract. Eng. Mater. Struct.*, vol. 30, no. 1, pp. 64–71, 2007.
- [102] B. Kolman and D. R. Hill, *Introductory Linear Algebra with Applications*, 6th ed. Upper Saddle River, N.J.: Prentice Hall, 1997.
- [103] O. Kraft and C. A. Volkert, "Mechanical testing of thin films and small structures," *Adv. Eng. Mater.*, vol. 3, no. 3, pp. 99–110, 2001.
- [104] D. J. Krus, G. Mearini, K. Chaffee, and R. W. Hoffman, "3D finite element analysis of thin-film stresses using ALGOR personal-computer-based software," *J. Vac. Sci. Technol. A*, vol. 9, no. 4, pp. 2488–2493, 1991.
- [105] J. Kühn, T. Colomb, F. Montfort, F. Charrière, Y. Emery, E. Cuche, P. Marquet, and C. Depeursinge, "Real-time dual-wavelength digital holographic microscopy with a single hologram acquisition," *Opt. Express*, vol. 15, no. 12, pp. 7231–7242, 2007.
- [106] U. Lang, T. Süss, and J. Dual, "Microtensile testing of submicrometer thick functional polymer samples," *Rev. Sci. Instrum.*, vol. 83, no. 7, 2012.
- [107] H. Lee, J. Coutu, S. Mall, and P. E. Kladitis, "Nanoindentation technique for characterizing cantilever beam style RF microelectromechanical systems (MEMS) switches," *J. Micromech. Microeng.*, vol. 15, no. 6, pp. 1230–1235, 2005.
- [108] H. J. Lee, G. Cornella, and J. C. Bravman, "Stress relaxation of free-standing aluminum beams for microelectromechanical systems applications," *Appl. Phys. Lett.*, vol. 76, no. 23, pp. 3415–3417, 2000.
- [109] H.-J. Lee, P. Zhang, and J. C. Bravman, "Stress relaxation in free-standing aluminum beams," *Thin Solid Films*, vol. 476, no. 1, pp. 118–124, 2005.
- [110] F. D. Lemkey and R. W. Kraft, "Tensile testing technique for submicron specimens," *Rev. Sci. Instrum.*, vol. 33, no. 8, pp. 846–849, 1962.
- [111] Z. C. Leseman and T. J. Mackin, "Indentation testing of axisymmetric freestanding nanofilms using a MEMS load cell," *Sensor. Actuat. A-Phys.*, vol. 134, no. 1, pp. 264–270, 2007.

- 
- [112] H. Li and A. H. W. Ngan, "Size effects of nanoindentation creep," *J. Mater. Res.*, vol. 19, no. 2, pp. 513–522, 2004.
- [113] X. Li, X. Wang, W. C. Chang, Y. J. Chao, and M. Chang, "Effect of tensile offset angles on micro/nanoscale tensile testing," *Rev. Sci. Instrum.*, vol. 76, no. 3, 2005.
- [114] X. Li, Y. Wei, W. Yang, and H. Gao, "Competing grain-boundary- and dislocation-mediated mechanisms in plastic strain recovery in nanocrystalline aluminum," *Proc. Nat. Acad. Sci.*, vol. 106, no. 38, pp. 16 108–16 113, 2009.
- [115] M. T. Lin, P. El-Deiry, R. R. Chromik, N. Barbosa III, W. L. Brown, T. J. Delph, and R. P. Vinci, "Temperature-dependent microtensile testing of thin film materials for application to microelectromechanical system," *Microsyst. Technol.*, vol. 12, no. 10-11, pp. 1045–1051, 2006.
- [116] J. P. Lokker, A. J. Böttger, W. G. Sloof, F. D. Tichelaar, G. C. A. M. Janssen, and S. Radelaar, "Phase transformations in Al-Cu thin films: Precipitation and copper redistribution," *Acta Mater.*, vol. 49, no. 8, pp. 1339–1349, 2001.
- [117] I. Lonardelli, J. Almer, G. Ischia, C. Menapace, and A. Molinari, "Deformation behavior in bulk nanocrystalline-ultrafine aluminum: in situ evidence of plastic strain recovery," *Scripta Mater.*, vol. 60, no. 7, pp. 520–523, 2009.
- [118] S. Mader and S. Herd, "Formation of second phase particles in aluminum-copper alloy films," *Thin Solid Films*, vol. 10, no. 3, pp. 377 – 389, 1972.
- [119] M. J. Madou, *Fundamentals of Microfabrication*, 2nd ed. Boca Raton: CRC Press LLC, 2002.
- [120] M. A. Marcus and J. E. Bower, "Precipitation of Al<sub>2</sub>Cu in blanket Al-Cu films," *J. Appl. Phys.*, vol. 82, no. 8, pp. 3821–3827, 1997.
- [121] M. McLean, W. L. Brown, and R. P. Vinci, "Temperature-dependent viscoelasticity in thin Au films and consequences for MEMS devices," *J. Microelectromech. Syst.*, vol. 19, no. 6, pp. 1299–1308, 2010.
- [122] G. J. McShane, M. Boutchich, A. S. Phani, D. F. Moore, and T. J. Lu, "Young's modulus measurement of thin-film materials using micro-cantilevers," *J. Micromech. Microeng.*, vol. 16, no. 10, pp. 1926–1934, 2006.
- [123] A. Meetsma, J. L. De Boer, and S. Van Smaalen, "Refinement of the crystal structure of tetragonal Al<sub>2</sub>Cu," *J. Solid State Chem.*, vol. 83, no. 2, pp. 370–372, 1989.
- [124] MEMS Journal Inc., "RF MEMS for smartphones: what are the best opportunities?" <http://www.memsjournal.com/2012/04/rf-mems-for-smartphones-where-are-the-best-opportunities.html>, Apr. 2012. [Online]. Available: <http://www.memsjournal.com>
- [125] J. Menčík and E. Quandt, "Determination of elastic modulus of thin films and small specimens using beam bending methods," *J. Mater. Res.*, vol. 14, no. 5, pp. 2152–2161, 1999.

- [126] H. D. Merchant, M. G. Minor, and Y. L. Liu, "Mechanical fatigue of thin copper foil," *J. Electron Mater.*, vol. 28, no. 9, pp. 998–1007, 1999.
- [127] G. Meyer and N. M. Amer, "Novel optical approach to atomic force microscopy," *Appl. Phys. Lett.*, vol. 53, no. 12, pp. 1045–1047, 1988.
- [128] R. Modlinski, A. Witvrouw, P. Ratchev, A. Jourdain, V. Simons, H. A. C. Tilmans, J. M. J. Den Toonder, R. Puers, and I. De Wolf, "Creep as a reliability problem in MEMS," *Microelectron. Reliab.*, vol. 44, no. 9–11, pp. 1733–1738, 2004.
- [129] R. Modlinski, A. Witvrouw, P. Ratchev, R. Puers, J. M. J. Den Toonder, and I. De Wolf, "Creep characterization of Al alloy thin films for use in MEMS applications," *Microelectron. Eng.*, vol. 76, no. 1–4, pp. 272–278, 2004.
- [130] R. Modlinski, P. Ratchev, A. Witvrouw, R. Puers, and I. D. Wolf, "Creep-resistant aluminum alloys for use in MEMS," *J. Micromech. Microeng.*, vol. 15, no. 7, pp. S165–S170, 2005.
- [131] R. Modlinski, R. Puers, and I. De Wolf, "AlCuMgMn micro-tensile samples. mechanical characterization of MEMS materials at micro-scale," *Sensor. Actuat. A-Phys.*, vol. 143, no. 1, pp. 120–128, 2008.
- [132] F. Montfort, F. Marquet, E. Cuche, N. Aspert, E. Solanas, Y. Emery, and C. Depeursinge, "Digital holography microscopy (DHM) operating in pulsed stroboscopic mode: a versatile metrology instrument for micro and nano technology," in *Proc. SPIE 6716, Optomechatronic Sensors and Instrumentation III*, 2007, p. 671605.
- [133] B. Moser, K. Wasmer, L. Barbieri, and J. Michler, "Strength and fracture of Si micropillars: A new scanning electron microscopy-based micro-compression test," *J. Mater. Res.*, vol. 22, no. 4, pp. 1004–1011, 2007.
- [134] H. Mughrabi, "Deformation-induced long-range internal stresses and lattice plane misorientations and the role of geometrically necessary dislocations," *Philos. Mag.*, vol. 86, no. 25–26, pp. 4037–4054, 2006.
- [135] W. W. Mullins, "Theory of thermal grooving," *J. Appl. Phys.*, vol. 28, no. 3, pp. 333–339, 1957.
- [136] J. L. Murray, "Aluminum-copper system," *Int. metals rev.*, vol. 30, no. 5, pp. 211–233, 1985.
- [137] A. Nafari, F. A. Ghavanini, M. Bring, K. Svensson, and P. Enoksson, "Calibration methods of force sensors in the micro-newton range," *J. Micromech. Microeng.*, vol. 17, no. 10, p. 2102, 2007.
- [138] Y. Nakajima, K. Kusuyama, H. Yamaguchi, and Y. Murakami, "Growth of single-crystal aluminum films on silicon substrates by DC magnetron sputtering," *Jap. J. Appl. Phys.*, vol. 31, no. 1–6A, pp. 1860–1867, 1992.
- [139] J. Neggers, J. P. M. Hoefnagels, F. Hild, S. Roux, and M. G. D. Geers, "A global digital image correlation enhanced full-field bulge test method," *Procedia IUTAM*, vol. 4, pp. 73 – 81, 2012.

- 
- [140] J. Negggers, J. P. M. Hoefnagels, F. Hild, S. Roux, and M. G. D. Geers, “Direct local stress-strain measurements from bulged membranes using topography image correlation,” *Exp. Mech.*, accepted.
- [141] W. C. Oliver and G. M. Pharr, “Improved technique for determining hardness and elastic modulus using load and displacement sensing indentation experiments,” *J. Mater. Res.*, vol. 7, no. 6, pp. 1564–1580, 1992.
- [142] C. O’Mahony, M. Hill, M. Brunet, R. Duane, and A. Mathewson, “Characterization of micromechanical structures using white-light interferometry,” *Meas. Sci. Technol.*, vol. 14, no. 10, pp. 1807–1814, 2003.
- [143] H. M. Otte, “Lattice parameter determinations with an X-ray spectrogoniometer by the Debye-Scherrer method and the effect of specimen condition,” *J. of Appl. Phys.*, vol. 32, no. 8, pp. 1536–1546, 1961.
- [144] B. Pan, K. Qian, H. Xie, and A. Asundi, “Two-dimensional digital image correlation for in-plane displacement and strain measurement: A review,” *Meas. Sci. Technol.*, vol. 20, no. 6, 2009.
- [145] M. F. Pantano, H. D. Espinosa, and L. Pagnotta, “Mechanical characterization of materials at small length scales,” *J. Mech. Sci. Tech.*, vol. 26, pp. 545–561, 2012.
- [146] J. H. Park, M. S. Myung, and Y. J. Kim, “Tensile and high cycle fatigue test of Al-3% Ti thin films,” *Sensor. Actuat. A-Phys.*, vol. 147, no. 2, pp. 561–569, 2008.
- [147] D. Porter, K. E. Easterling, and M. Y. Sherif, *Phase transformations in metals and alloys*, 3rd ed. Boca Raton: CRC Press, 2009.
- [148] R. Raj and M. F. Ashby, “On grain boundary sliding and diffusional creep,” *Metal. Trans.*, vol. 2, no. 4, pp. 1113–1127, 1971.
- [149] J. Rajagopalan, J. H. Han, and M. T. A. Saif, “Plastic deformation recovery in freestanding nanocrystalline aluminum and gold thin films,” *Science*, vol. 315, no. 5820, pp. 1831–1834, 2007.
- [150] J. Rajagopalan, J. H. Han, and M. T. A. Saif, “On plastic strain recovery in free-standing nanocrystalline metal thin films,” *Scripta Mater.*, vol. 59, no. 9, pp. 921–926, 2008.
- [151] D. T. Read, “Tension-tension fatigue of copper thin films,” *Int. J. Fatigue*, vol. 20, no. 3, pp. 203–209, 1998.
- [152] D. T. Read, Y. W. Cheng, R. R. Keller, and J. D. McColskey, “Tensile properties of free-standing aluminum thin films,” *Scripta Mater.*, vol. 45, no. 5, pp. 583–589, 2001.
- [153] G. Rebeiz, *RF MEMS: Theory, Design, and Technology*, 1st ed. Wiley-Interscience, 2003.
- [154] J. M. Rickman, R. LeSar, and D. J. Srolovitz, “Solute effects on dislocation glide in metals,” *Acta Mater.*, vol. 51, no. 5, pp. 1199–1210, 2003.

- [155] H. Sadeghian, C. K. Yang, J. F. L. Goosen, A. Bossche, U. Staufer, P. J. French, and F. van Keulen, "Effects of size and defects on the elasticity of silicon nanocantilevers," *J. Micromech. Microeng.*, vol. 20, no. 6, p. 064012, 2010.
- [156] R. Saha and W. D. Nix, "Effects of the substrate on the determination of thin film mechanical properties by nanoindentation," *Acta Mater.*, vol. 50, no. 1, pp. 23–38, 2002.
- [157] B. A. Samuel, A. V. Desai, and M. A. Haque, "Design and modeling of a MEMS pico-Newton loading/sensing device," *Sensor. Actuat. A-Phys.*, vol. 127, no. 1, pp. 155–162, 2006.
- [158] C. A. Schuh, C. E. Packard, and A. C. Lund, "Nanoindentation and contact-mode imaging at high temperatures," *J. Mater. Res.*, vol. 21, no. 3, pp. 725–736, 2006.
- [159] R. Schwaiger and O. Kraft, "Analyzing the mechanical behavior of thin films using nanoindentation, cantilever microbeam deflection, and finite element modeling," *J. Mater. Res.*, vol. 19, no. 1, pp. 315–324, 2004.
- [160] W. N. Sharpe Jr., "Mechanical properties of MEMS materials," in *The MEMS Handbook*, 1st ed., M. G. el Hak, Ed. CRC Press, 2001, book chapter 3, pp. 1–33.
- [161] W. N. Sharpe Jr., K. T. Turner, and R. L. Edwards, "Tensile testing of polysilicon," *Exp. Mech.*, vol. 39, no. 3, pp. 162–170, 1999.
- [162] J. M. Silcock and T. J. Heal, "The  $\theta'$  structure in aluminium–copper alloys," *Acta Crystal.*, vol. 9, no. 8, p. 680, Aug 1956.
- [163] V. T. Srikar and S. M. Spearing, "A critical review of microscale mechanical testing methods used in the design of microelectromechanical systems," *Exp. Mech.*, vol. 43, no. 3, pp. 238–247, 2003.
- [164] J. W. Steeds, "Dislocation arrangement in copper single crystals as a function of strain," *Proc. R. Soc. Lond. A*, vol. 292, pp. 343–373, 1966.
- [165] M. A. Sutton, J. Orteu, and H. W. Schreier, *Image Correlation for Shape, Motion and Deformation Measurements*, 1st ed. New York City, NY: Springer Science+Business Media, LLC, 2009.
- [166] D. Tabor, *The hardness of metals*, ser. Monographs on the physics and chemistry of materials. London, UK: Oxford University Press, 1951.
- [167] H. A. C. Tilmans, W. De Raedt, and E. Beyne, "MEMS for wireless communications: 'from RF-MEMS components to RF-MEMS-SiP'," *J. Micromech. Microeng.*, vol. 13, no. 4, pp. S139–S163, 2003.
- [168] K. Tsubouchi, K. Masu, N. Shigeeda, T. Matano, Y. Hiura, N. Mikoshiba, S. Matsumoto, T. Asaba, T. Marui, and T. Kajikawa, "Selective and nonselective deposition of aluminum by LPCVD using DMAH and microregion observation of single crystal aluminum with scanning  $\mu$ -RHEED microscope," in *1990 Symposium on VLSI Technology, Digest of Technical Papers*, 1990, pp. 5–6.

- 
- [169] T. Tsuchiya, M. Shikida, and K. Sato, "Tensile testing system for sub-micrometer thick films," *Sensor. Actuat. A-Phys.*, vol. 97-98, pp. 492–496, Jun 2002.
- [170] M. Van Gils, J. A. Bielen, and G. McDonald, "Evaluation of creep in RF MEMS devices," in *EuroSime 2007: Int. Conf. Thermal, Mechanical and Multi-Physics Simulation Experiments in Microelectronics and Micro-Systems*, 2007, p. 360033.
- [171] W. M. Van Spengen, "MEMS reliability from a failure mechanisms perspective," *Microelectron. Reliab.*, vol. 43, no. 7, pp. 1049–1060, 2003.
- [172] W. M. Van Spengen, R. Puers, R. Mertens, and I. De Wolf, "Characterization and failure analysis of MEMS: High resolution optical investigation of small out-of-plane movements and fast vibrations," *Microsyst. Technol.*, vol. 10, no. 2, pp. 89–96, 2004.
- [173] W. M. Van Spengen, R. Modlinski, R. Puers, and A. Jourdain, "Failure mechanisms in MEMS/NEMS devices," in *Springer Handbook of Nanotechnology*, B. Bhushan, Ed. Springer Berlin Heidelberg, 2007, pp. 1663–1684.
- [174] D. Vaughan, "The precipitation of  $\theta'$  at high-angle boundaries in an Al-Cu alloy," *Acta Metall.*, vol. 18, no. 1, pp. 183 – 187, 1970.
- [175] R. Venkatraman, J. C. Bravman, W. D. Nix, P. W. Davies, P. A. Flinn, and D. B. Fraser, "Mechanical properties and microstructural characterization of Al-0.5%Cu thin films," *J. Electron Mater.*, vol. 19, no. 11, pp. 1231–1237, 1990.
- [176] R. H. Wagoner, H. Lim, and M. G. Lee, "Advanced issues in springback," *Int. J. Plasticity*, vol. 45, no. 0, pp. 3 – 20, 2013.
- [177] J. F. Wang, R. H. Wagoner, W. D. Carden, D. K. Matlock, and F. Barlat, "Creep and anelasticity in the springback of aluminum," *Int. J. Plasticity*, vol. 20, no. 12, pp. 2209–2232, 2004.
- [178] X. Wei and J. W. Kysar, "Residual plastic strain recovery driven by grain boundary diffusion in nanocrystalline thin films," *Acta Mater.*, vol. 59, no. 10, pp. 3937 – 3945, 2011.
- [179] Y. Wei, A. F. Bower, and H. Gao, "Recoverable creep deformation and transient local stress concentration due to heterogeneous grain-boundary diffusion and sliding in polycrystalline solids," *J. Mech. Phys. Solids*, vol. 56, no. 4, pp. 1460–1483, 2008.
- [180] T. P. Weihs, S. Hong, J. C. Bravman, and W. D. Nix, "Mechanical deflection of cantilever microbeams: A new technique for testing the mechanical properties of thin films," *J. Mater. Res.*, vol. 3, no. 5, pp. 931–942, 1988.
- [181] A. Witvrouw, H. A. C. Tilmans, and I. De Wolf, "Materials issues in the processing, the operation and the reliability of MEMS," *Microelectron. Eng.*, vol. 76, no. 1–4, pp. 245–257, 2004.
- [182] H. C. Wu and D. R. Rummeler, "Analysis of misalignment in the tension test," *J. Eng. Mater. Technol. Trans. ASME*, vol. 101, no. 1, pp. 68–74, 1979.
- [183] A. Ya'akovovitz, S. Krylov, and Y. Hanein, "Nanoscale displacement measurement of electrostatically actuated micro-devices using optical microscopy and digital image correlation," *Sensor. Actuat. A-Phys.*, vol. 162, no. 1, pp. 1–7, 2010.

- [184] C. Yamahata, E. Sarajlic, G. J. M. Krijnen, and M. A. M. Gijs, “Subnanometer translation of microelectromechanical systems measured by discrete fourier analysis of CCD images,” *J. Microelectromech. Syst.*, vol. 19, no. 5, pp. 1273–1275, 2010.
- [185] X. Yan, W. L. Brown, Y. Li, J. Papapolymerou, C. Palego, J. C. M. Hwang, and R. P. Vinci, “Anelastic stress relaxation in gold films and its impact on restoring forces in MEMS devices,” *J. Microelectromech. Syst.*, vol. 18, no. 3, pp. 570–576, 2009.
- [186] B. Yang, C. Motz, W. Grosinger, W. Kammrath, and G. Dehm, “Tensile behaviour of micro-sized copper wires studied using a novel fibre tensile module,” *Int. J. Mater. Res.*, vol. 99, no. 7, pp. 716–724, 2008.
- [187] S. Yu, S. Fry, D. P. Potasek, D. Bell, and B. Nelson, “Characterizing fruit fly flight behavior using a microforce sensor with a new comb-drive configuration,” *J. Microelectromech. Syst.*, vol. 14, no. 1, pp. 4–11, 2005.
- [188] B. Yuan and W. N. Sharpe Jr., “Mechanical testing of polysilicon thin films with the isdg,” *Exp. Techn.*, vol. 21, no. 2, pp. 32–35, 1997.
- [189] G. P. Zhang, C. A. Volkert, R. Schwaiger, P. Wellner, E. Arzt, and O. Kraft, “Length-scale-controlled fatigue mechanisms in thin copper films,” *Acta Mater.*, vol. 54, no. 11, pp. 3127–3139, 2006.
- [190] Q. Zhou and G. Itoh, “Creep behavior of aluminum alloy foils for microelectronic circuits,” *Key Eng. Mat.*, vol. 171-174, pp. 633–638, 2000.
- [191] Q. Zhou, G. Itoh, and T. Yamashita, “Further study on the effects of specimen thickness and grain size on the creep behavior of aluminum alloy foils,” *Mater. Trans. JIM*, vol. 40, no. 5, pp. 443–446, 1999.
- [192] Y. Zhu, N. Moldovan, and H. D. Espinosa, “A microelectromechanical load sensor for in situ electron and X-ray microscopy tensile testing of nanostructures,” *Appl. Phys. Lett.*, vol. 86, no. 1, 2005.
- [193] Y. Zhu, A. Corigliano, and H. D. Espinosa, “A thermal actuator for nanoscale in situ microscopy testing: Design and characterization,” *J. Micromech. Microeng.*, vol. 16, no. 2, pp. 242–253, 2006.

# Appendix A

## Enhanced Global Digital Image Correlation for accurate measurement of microbeam bending

---

Reproduced from; L.I.J.C. Bergers, J. Neggers, M.G.D. Geers, J.P.M. Hoefnagels, *Enhanced Global Digital Image Correlation for Accurate Measurement of Microbeam Bending*, Proceedings of IUTAM Symposium on Advanced Materials Modelling for Structures, 43–51, (2013)

### Abstract

Microbeams are simple on-chip test structures used for thin film and MEMS materials characterization. Profilometry can be combined with Euler-Bernoulli (EB) beam theory to extract material parameters, like the E-modulus. Characterization of time-dependent microbeam bending is required, though non-trivial, as it involves long term sub-microscale measurements. Here we propose an *enhanced* global digital image correlation (GDIC) procedure to analyze time-dependent microbeam bending. Using GDIC we extract the full-field *curvature* profile from optical profilometry data of thin metal microbeam bending experiments, whilst simultaneously correcting for rigid body motion resulting from drift. This work focusses on the implementation of this GDIC procedure and evaluation of its accuracy through a numerical assessment of the proposed methodology.



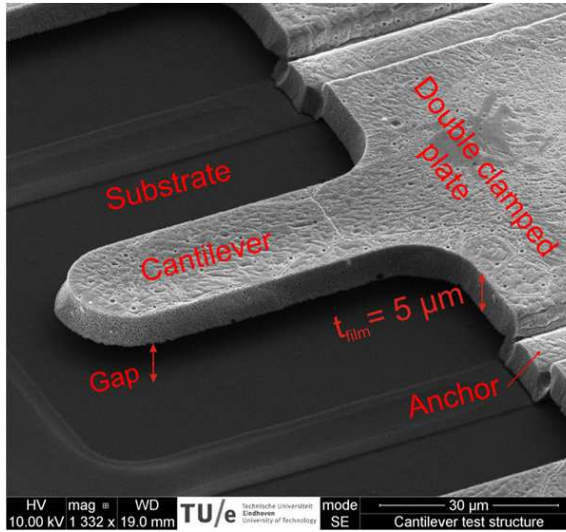


Figure A.1: Scanning electron micrograph of a typical on-chip microbeam attached to a free-standing double clamped plate that is anchored to the substrate.

## A.1 Introduction

Microbeams are simple on-chip test structures used for thin film and MEMS materials characterization [69], see Fig. A.1. Optical profilometry techniques are typically used for the measurement of deformations [142, 172]. Profilometry can be combined with Euler-Bernoulli (EB) beam theory to extract material parameters, like the E-modulus or creep parameters. The latter requires characterization of time-dependent microbeam bending, though non-trivial, as it involves long term sub-microscale measurements. On the one hand environmental instabilities directly hinder accurate long term measurements. On the other hand microfabrication limitations often affect the ideal fixed-end geometrical boundary condition [66]. This requires attention, because a non-ideal fixed-end, e.g. a compliant anchor, introduces errors when using the microbeam *deflection* with EB-theory [125]. Hence, the problem is attaining sufficient accuracy and precision in these measurements.

A first step towards precise microbeam bending experiments is the careful design and construction of the setup and proper control of the profilometer's environment [9]. In [9] we presented a simple image correlation based methodology to correct the rigid body motions, e.g. due to drift, of the deformed specimen on the  $xy\theta_x\theta_y$ -positioning stage. The difference between the reference profile and this deformed profile yielded the tip deflection. However, this correlation based correction has a drawback: the correction is extrapolated to the entire beam profile based on a limited reference area on the anchor. As the beam lies in the extended direction of the anchor, the resulting tip deflection is sensitive to an extrapolation error.

Following *Neggers et al.* [139], we here present an improved approach for microbeam bending analysis. The approach in [139] extracts curvature from profilometry data of bulged membranes through enhanced global digital image correlation (GDIC). The key point is the

use of the deformation kinematics as degrees of freedom to be solved in the minimization problem formulated for DIC as demonstrated by *Hild* and *Roux* [83, 84]. Therefore, in the approach presented here we combine the drift and beam bending kinematics and directly correlate on the beam, eliminating any extrapolation errors. The correlation procedure yields the displacement fields. This does not directly yield the beam *deflection*, because the position of the anchor is not resolved. However, the *curvature* field of the beam can be directly extracted from this displacement field, because a C2-continuous basis for the degrees of freedom is chosen. This effectively filters measurement noise, overcoming issues when taking derivatives to calculate the curvature. In short, this improved approach yields an accurate curvature field, in stead of beam deflection, that serve equally well in analyzing microbeam bending mechanics.

In this work, we describe the kinematics involved followed by the implementation into the GDIC procedure through which the curvature is determined. To asses the accuracy of this new procedure a numerical experiment is performed of which the implementation and results are discussed.

## A.2 Principle of global digital image correlation and curvature measurement

In the solid mechanics community DIC has become an established method to measure deformation fields at various length scales both in 2D and 3D geometries [165]. For the 2D case one records an image of an undeformed, reference situation of an object and of its the deformed situation. Parts of the image with a unique pattern can then be correlated from one image to the next, allowing one to extract the displacements between the two instances. Traditionally, one applies a pattern with sufficient detail and variation to obtain uniqueness for the correlation procedure.

The correlation procedure in 2D is based on the principle of optical flow conservation. It states that the reference image, represented by the intensity field  $f(\vec{x})$ , is related to the deformed image,  $g(\vec{x})$  through the in-plane displacement field  $\mathbf{u}_{xy}(\vec{x})$  and measurement noise  $n_0(\vec{x})$ :

$$g(\vec{x} + \vec{u}_{xy}(\vec{x})) = f(\vec{x}) + n_0(\vec{x}). \quad (\text{A.1})$$

In the case of optical profilometer data, the intensity is in fact a height, and can also vary due to e.g. deformations. This quasi 3D nature can be exploited by relaxing the optical flow conservation:

$$g(\vec{x} + \vec{u}_{xy}(\vec{x})) = f(\vec{x}) + u_z(\vec{x}) + n_0(\vec{x}). \quad (\text{A.2})$$

The unknown displacement fields  $\vec{u}(\vec{x})$  are found through minimizing the global residual  $\eta$  of the weak form of Eq.(A.2) over the considered domain

$$\eta^2 = \int [(f(\vec{x}) - g(\vec{x} + \vec{u}_{xy}(\vec{x})) + u_z(\vec{x}))^2 d\vec{x} = \int r(\vec{x})^2 d\vec{x}, \quad (\text{A.3})$$

where  $r(\vec{x})$  is the residual field. The displacement field is parameterized and interpolated using a set of basis functions  $\phi_n(\vec{x})$  acting globally over the entire domain and weighted with a discrete set of degrees of freedom  $u_n$

$$\vec{u}(\vec{x}) = u_x(\vec{x})\vec{e}_x + u_y(\vec{x})\vec{e}_y + u_z(\vec{x})\vec{e}_z = \sum_n u_n \phi_n(\vec{x}) \vec{e}_i, \quad (\text{A.4})$$

where  $i = [x, y, z]$  and the basis functions  $\phi_n(\vec{x})$  are polynomial functions depending on  $\vec{x} = x\vec{e}_x + y\vec{e}_y$

$$\phi_n = x^{\alpha(n)} y^{\beta(n)}. \quad (\text{A.5})$$

The choice for this parametrization has the benefit that it allows one to introduce degrees of freedom suitable for describing the deformation kinematics, whilst maintaining a continuously differentiable solution. This aspect is important, because the strain and, particularly for microbeam bending, curvature fields are (higher order) derivatives of the displacement fields. Furthermore when the order of the polynomials are limited, measurement noise is effectively filtered, yielding a robust curvature measurement: the smooth continuously differentiable displacement fields and not the measurement data serve as input for differentiation.

The introduction of the degrees of freedom and the appropriate basis functions can be based on prior knowledge of the deformation kinematics. For example, a uniaxial strain in  $x$ ,  $\epsilon_{xx}$ , could be described by adding a basis function of degree  $[\alpha, \beta] = [1, 0]$  in  $x$ -direction:  $\phi_{10} = x^1 y^0$ . Adding this basis function to the  $z$ -direction would describe a constant tilt. One should however be aware that superfluous degrees of freedom will not necessarily yield the correct solution for the displacement fields, because of the measurement noise. On the other hand residual fields showing systematic deviations from zero might indicate insufficient kinematic degrees of freedom. Therefore, the prior knowledge allows a sufficient choice of degrees of freedom that will describe the kinematics, but limit inaccuracies due to noise.

As the curvature field is the desired measurand from the microbeam bending experiment, we consider all rigid body displacements, rotations about the  $x$ - and  $y$ -axis, resulting from drift of the  $xy\theta_x\theta_y$ -platform, and the end-loaded bending of the single clamped microbeam. The bending results in a gradient in curvature, involving a third order displacement derivative along the beam's axis, which is taken along the  $x$ -direction. Hence the parametrization of the displacement fields takes the following form:

$$u(x) = (u_{x,00})\vec{e}_x + (u_{y,00})\vec{e}_y + (u_{z,00} + u_{z,10}x + u_{z,01}y + u_{z,20}x^2 + u_{z,30}x^3)\vec{e}_z. \quad (\text{A.6})$$

From the displacement fields resulting from the GDIC procedure, the curvature field tangent to the beam's surface in x-direction,  $\kappa_{xx}(\vec{x})$ , can be derived. First the curvature tensor is constructed as the dyadic product of the gradient operator and the surface normal:

$$\boldsymbol{\kappa} = \vec{\nabla} \otimes \vec{n}, \quad (\text{A.7})$$

where the gradient operator is defined as

$$\vec{\nabla} = \vec{e}_x \frac{\partial}{\partial x} + \vec{e}_y \frac{\partial}{\partial y} + \vec{e}_z \frac{\partial}{\partial z}. \quad (\text{A.8})$$

The normal vector is calculated from the position field of the deformed microbeam  $z(x, y)$ , obtained by applying the resulting displacement fields to the reference profile:

$$\vec{n} = \frac{\vec{\nabla} z(\vec{x})}{\|\vec{\nabla} z(\vec{x})\|}. \quad (\text{A.9})$$

Finally the curvature field in a given tangent direction is calculated by

$$\kappa_{\vec{t}}(\vec{x}) = \vec{t} \cdot \boldsymbol{\kappa} \cdot \vec{t} \quad (\text{A.10})$$

where the unit tangent vector,  $\vec{t}(\vec{\tau})$ , along an in-plane unit vector  $\vec{\tau}(\vec{x}) = \tau_x \vec{e}_x + \tau_y \vec{e}_y$  is

$$\vec{t} = \frac{\tau_x \vec{e}_x + \tau_y \vec{e}_y + (\vec{\nabla} f) \cdot \vec{\tau} \otimes \vec{e}_z}{\sqrt{\tau_x^2 + \tau_y^2 + [(\vec{\nabla} f) \cdot \vec{\tau}]^2}} \quad (\text{A.11})$$

and  $\vec{\tau} \otimes \vec{e}_z$  is the dyadic product of the two vectors. In the processing applied, the curvature is measured along the tangent in-plane unit vector  $\vec{\tau} = 1\vec{e}_x$ .

### A.3 Evaluation of accuracy

In order to evaluate the accuracy of the GDIC approach a numerical microbeam bending experiment is conducted. A linear elastic finite element model of a representative microbeam ( $l = 100 \mu\text{m}, w = 20 \mu\text{m}, t = 5 \mu\text{m}$ ) is modeled in Marc/Mentat using quadratic thick shell elements, see Fig.A.2. Only half of the microbeam is modeled due to symmetry. It is deflected at the end by  $2 \mu\text{m}$ . The surface topography of a physical microbeam is measured using a Sensofar Plu2300 confocal optical profilometer, see Fig.A.3a and [9] for details. A corresponding part of this topography, see  $\text{ROI}_f$  in Fig.A.3b, is deformed with the numerically generated displacement fields. An additional constant in-plane displacement  $\vec{u}_{xy}(\vec{x}) = 1,162\vec{e}_x - 0,830\vec{e}_y \mu\text{m}$  as well as an out-of-plane tilt  $\vec{u}_z(\vec{x}) = (0,0005x - 0,0006y)\vec{e}_z \mu\text{m}$  simulate drift, see  $\text{ROI}_g$  in Fig.A.3b. These values

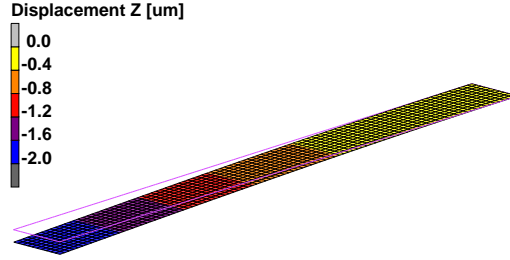


Figure A.2: The FEM model in deformed state used for generating the displacement fields. The left end is deflected, whilst the right end is clamped.

are selected as uneven half-pixel multiples, where the pixel size is  $0,332 \times 0,332 \mu\text{m}^2$ , serving as a worst case, because this leads to the poorest DIC accuracy [83]. The deformed and displaced topography serves as input for the GDIC procedure with the natural surface features serving as the pattern. Subsequently the curvature is calculated based on the GDIC output and compared to the numerically prescribed curvature calculated from the nodal displacements and rotations of the FEM output.

To minimize numerical artifacts when doing this numerical evaluation there are some issues to address. First, the computational mesh and discrete surface topography will have a different discretization. This is overcome by interpolating both surfaces with C1- or C2-continuous interpolation functions to finer and equal grids and excluding pixels adjacent to the border of the region of interest. Second, the prescribed curvature fields calculated from interpolated nodal displacement fields will show artifacts, because the nodal displacements are not C1-continuous between elements. Although nodal rotations strictly speaking also suffer the same discontinuity, they effectively do form a C1-continuous gradient of the displacement field for the curvature calculation. Hence the nodal rotations  $\theta_i$  are interpolated and used in the curvature calculation through the following definition of  $\vec{n}$ :

$$\vec{n} = \frac{\tan(\theta_y(\vec{x}))\vec{e}_x + \tan(\theta_x(\vec{x}))\vec{e}_y + \vec{e}_z}{\sqrt{\tan(\theta_x(\vec{x}))^2 + \tan(\theta_y(\vec{x}))^2 + 1}}. \quad (\text{A.12})$$

## A.4 Results

The results of the GDIC at different levels of deflection are judged by the displacement fields obtained in  $x$ -,  $y$ - and  $z$ -direction and the residual field. The resulting displacement fields show good agreement with the prescribed displacement fields, see Fig. A.4. For the in-plane displacements an accuracy of  $< 13 \text{ nm}$  is observed, which corresponds to  $\sim 0,04$  pixels for a  $332 \text{ nm}$  pixel size. The accuracy of the  $z$  displacement field is  $< 2 \text{ nm}$ , whilst its field reveals a systematic error. This might be caused by a slight curvature in  $y$ -direction that is not covered by the admitted degrees of freedom.

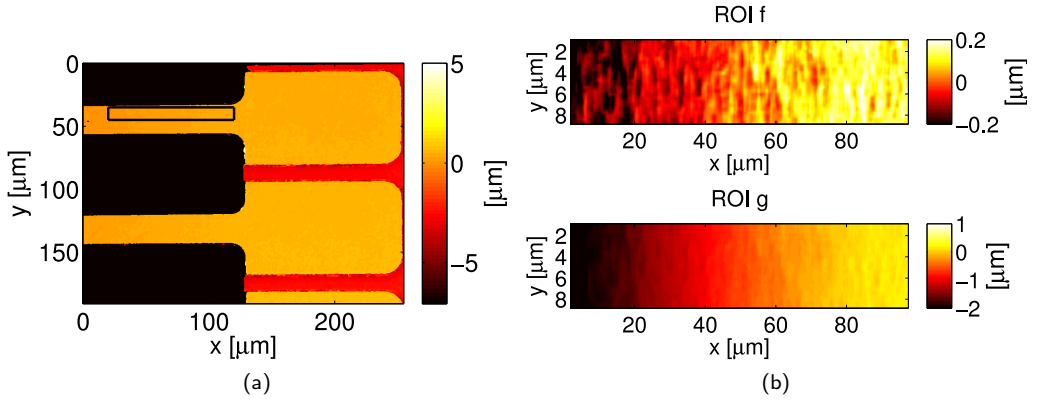


Figure A.3: (a) A contour plot of two actual microbeams. The box on the top beam's surface indicates the part used for GDIC as shown in (b): ROIs of the undeformed  $f$  and deformed  $g$  selection from the beam.

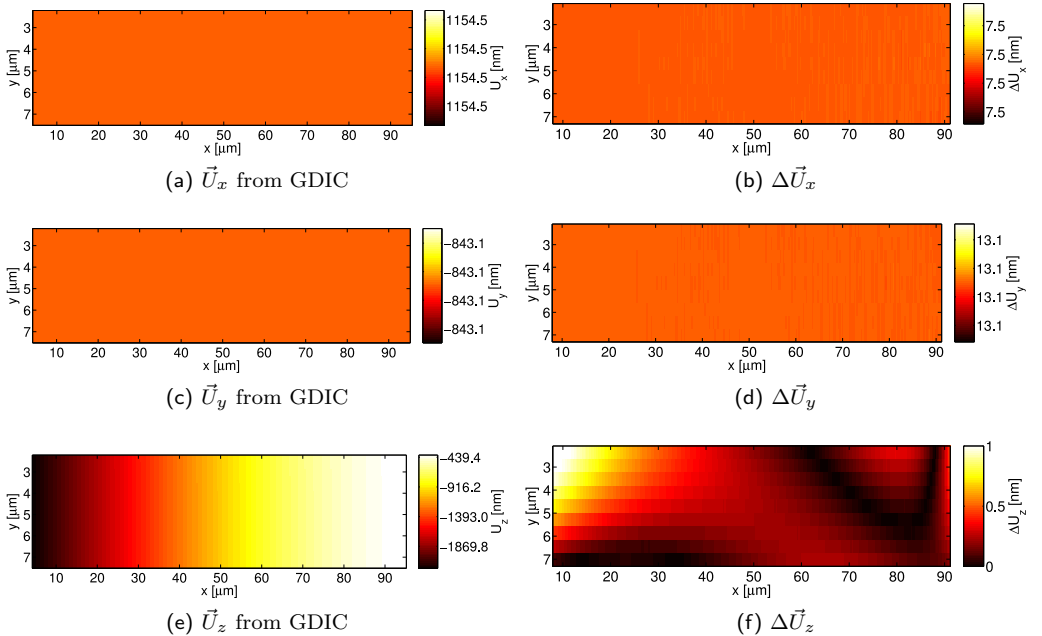


Figure A.4: Resulting displacement fields including drift at 2  $\mu\text{m}$  deflection obtained through GDIC. (a,c,e) are the GDIC obtained displacement fields and (b,d,f) are the difference fields between the GDIC and FEM displacement fields.

When regarding the residual field and comparing to the undeformed pattern, see Fig. A.5, no systematic features are observed, indicating the correlation has reached the global minimum. Further, the amplitude of the residual field is relatively large, about 10% of the undeformed pattern. If the global minimum is obtained, this amplitude can only be attributed to the limited number of pixels, being  $\sim 20 \times 190$ , and the effect of interpolating the surface pattern within the correlation algorithm. Improving this requires a smoother surface pattern and higher spatial sampling. Nonetheless, the results are adequate compared to local DIC approaches where typically facets of  $15 \times 15$  pixels are employed to resolve displacement fields with similar accuracy.

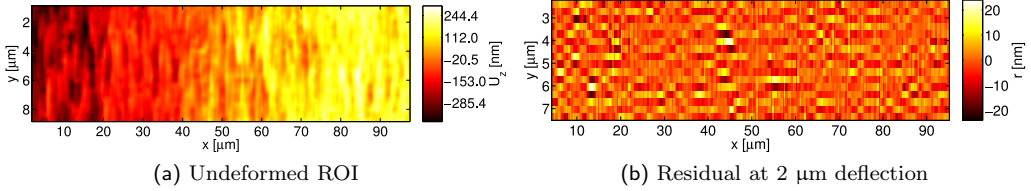


Figure A.5: Comparison of the amplitude in the pattern and the resulting residuals showing a relatively low residual.

The curvature fields  $\kappa_{xx}$  obtained through the GDIC at 1 and 2  $\mu\text{m}$  deflection and the difference between these and the simulated  $\kappa_{xx}$  reveal a good measurement of  $\kappa_{xx}$ , see Fig. A.6. The expected gradient in  $\kappa_{xx}$  is visible, approaching 0 at the tip of the beam (left hand side of images) and reaching a maximum at the clamped end (right hand side of images). The difference shows a limited error, caused by the limited choice of degrees of freedom and required interpolation during correlation.

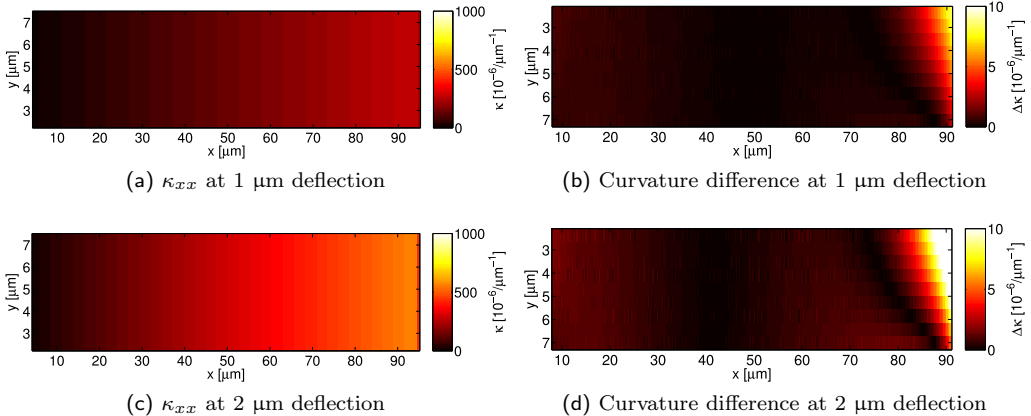


Figure A.6: Curvature fields  $\kappa_{xx}$  at 1  $\mu\text{m}$  and 2  $\mu\text{m}$  deflection reveal the expected gradient, whilst the differences with the numerically prescribed fields show a good accuracy.

Within the probed range of  $\kappa_{xx}$  the accuracy of the measurement is  $< 1\%$  for most of the ROI, see Fig. A.7. The accuracy, defined as the relative error ( $\kappa_{xx, GDIC} -$

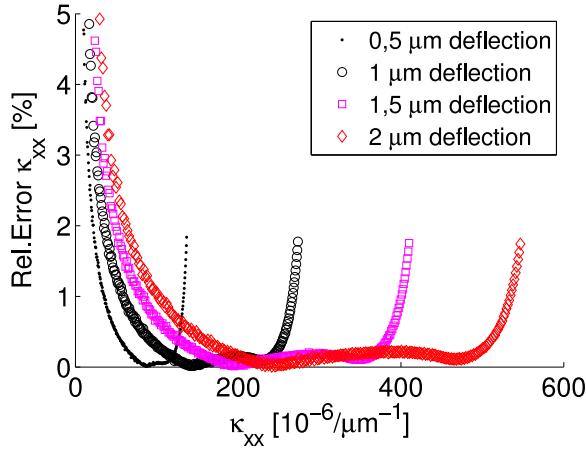


Figure A.7: The accuracy of  $\kappa_{xx}$  obtained is good for the part of the ROI that is not near the loaded end or the clamped end.

$\kappa_{xx,FEM})/\kappa_{xx,FEM}$ , increases near the clamped end due to the additional  $\kappa_{yy}$  and at the loaded end due to the definition of the accuracy. Naturally one can not measure data near these regions.

## A.5 Conclusion

We presented an enhanced digital image correlation approach to extract beam curvature from full-field deformation data of microbeam bending experiments. A limited yet sufficient amount of degrees of freedom in the GDIC described the bending kinematics as well as possible rigid body motions that might be caused due to drift in actual experiments. A numerical analysis of the accuracy based on FEM revealed that the proposed GDIC accurately resolved the bending kinematics: an accuracy in the  $\kappa_{xx}$ -measurement of  $< 1\%$  for parts of the beam away from the clamped and free ends. The presented numeric analysis can also be extended to simulate the influence of measurement artifacts, e.g. noise or pattern quality. This GDIC methodology thus enables the precise measurement of beam curvature required for time-dependent microbeam bending experiments. It might also find application in other microbeam bending analyses, e.g. stress measurements of deflecting structural parts of microdevices in case of known material parameters.





# Appendix B

## Multi-mode linear time-dependent anelasticity

---

This appendix elaborates  $\varepsilon_{\text{anel.}}$  as a function of the material parameters and time, by solving the governing equations of the viscoelastic model for the initial and boundary conditions discussed in Chapter 3. First the measured total strain is calculated from the curvature  $\varepsilon_{\text{total.}} = \kappa_{\text{meas.}} t_{\text{film}}/2$ . Assuming that the permanent strain  $\varepsilon_{\text{perm.}}$  is instantaneous, we have

$$\varepsilon_{\text{total}}(t) = \varepsilon_{\text{anel.}}(t) + \varepsilon_{\text{perm.}} \quad (\text{B.1})$$

$\varepsilon_{\text{anel.}}$  is obtained by solving the governing equations for the visco-elastic part of the model system, which are:

$$\varepsilon_{\text{anel.}} = \varepsilon_{\text{E}_0} = \varepsilon_{\text{E}_i} + \varepsilon_{\eta_i}, \quad (\text{B.2})$$

$$\sigma_{\text{external}} = \sum_{i=0}^n \sigma_i, \quad (\text{B.3})$$

$$\sigma_i = \varepsilon_{\text{E}_i} \text{E}_i = \eta_i \dot{\varepsilon}_{\eta_i}. \quad (\text{B.4})$$

The subscript  $i$  denotes the mode, see Fig.3.6.  $\varepsilon_{\text{anel.}}$  can be expressed in terms of the external stress state by combining Eqs.B.2- B.4 and reformulating in terms of the mode's  $\varepsilon_{\eta_i}$  and material parameters, where  $\text{E} = \sum_{i=0}^n \text{E}_i$  is the Young's modulus:

$$\sigma_{\text{external}} = \text{E}_0 \varepsilon_{\text{anel.}} + \sum_{i=1}^n \sigma_i = \text{E} \varepsilon_{\text{anel.}} - \sum_{i=1}^n \text{E}_i \varepsilon_{\eta_i}. \quad (\text{B.5})$$

and the differential equations per mode  $i$

$$\frac{\eta_i}{\text{E}_i} \dot{\varepsilon}_{\eta_i} + \varepsilon_{\eta_i} = \varepsilon_{\text{anel.}} \quad (\text{B.6})$$

For the load part of the sequence,  $t_0 = 0 \leq t \leq t_{\text{hold}}$ , the constant applied strain is modeled as a step function and therefore each differential equation can be solved separately:

$$\varepsilon_{\eta_i} = \varepsilon_{\text{hold,anel.}}(1 - e^{-t_{\text{hold}}/\tau_i}). \quad (\text{B.7})$$

For the release part of the sequence,  $t > t_{\text{hold}}$  and  $\sigma_{\text{ext.}} = 0$ , Eq.B.5 becomes:

$$\varepsilon_{\text{anel.}} = \sum_{i=1}^n \frac{E_i}{E} \varepsilon_{\eta_i}, \quad (\text{B.8})$$

which combines with Eq. B.6 to yield a system of  $i = 1 : n$  coupled differential equations:

$$\dot{\varepsilon}_{\eta_i} = \frac{E_i}{\eta_i} \frac{E_i - E}{E} \varepsilon_{\eta_i} + \frac{E_i}{\eta_i} \sum_{j=1, j \neq i}^n \frac{E_j}{E} \varepsilon_{\eta_j}, \quad (\text{B.9})$$

or in matrix notation:

$$\dot{\underline{\varepsilon}}_{\eta_i} = \underline{A} \underline{\varepsilon}_{\eta_i}. \quad (\text{B.10})$$

The solution for each  $\varepsilon_{\eta_i}$  is obtained by solving the eigenvalue problem of this system:  $(\underline{A} - \lambda \underline{I}) = 0$ , which yields the eigenvalues  $\lambda_i$  and eigenvectors  $\underline{p}_i$ , [102]:

$$\underline{\varepsilon}_{\eta} = \sum_{j=1}^n b_j \underline{p}_j e^{\lambda_j(t-t_{\text{hold}})} \quad (\text{B.11})$$

where  $b_j$  are constants to be solved with the initial values given by Eq.B.7. They can be formulated as:

$$b_j = \varepsilon_{\text{hold,anel.}} b'_j, \quad b'_j = f(E, E_j, \tau_j). \quad (\text{B.12})$$

Applying this to the set of  $n$ -coupled differential equations yields per mode:

$$\varepsilon_{\eta_i}(t) = \varepsilon_{\text{hold,anel.}} \sum_{j=1}^n b'_j p_j(i) e^{\lambda_j(t-t_{\text{hold}})} \quad (\text{B.13})$$

Each of these solutions is substituted directly into Eq.B.8, which is then substituted in Eq.B.1:

$$\varepsilon_{\text{total.}}(t) = \varepsilon_{\text{hold,anel.}} \sum_{i=1}^n \frac{E_i}{E} \left( \sum_{j=1}^n b'_j p_j(i) e^{\lambda_j(t-t_{\text{hold}})} \right) + \varepsilon_{\text{perm.}} \quad (\text{B.14})$$

# Appendix C

## Derivation of misalignment criterium

---

The ratio of the bending stress with respect to the nominal uniaxial stress is used as a criterium for misalignment assuming small deformations for a tensile specimen of gauge length  $l$ , width  $w$ , thickness  $t$  and moment of area  $I$ . The axial stress at position  $x$  along the gauge length is the sum of the nominal uniaxial stress  $\sigma_{xx,\text{nom.}}(x)$  induced by the load  $F_{\parallel}$  and a bending stress  $\sigma_{xx,\text{bend}}(x)$  induced by the moment due to eccentricity,  $M_{\delta} = F_{\parallel}\delta$  or due to a perpendicular load  $F_{\perp}$ :

$$\sigma_{xx}(x) = \sigma_{xx,\text{nom.}} + \sigma_{xx,\text{bend}}(x). \quad (\text{C.1})$$

In the case of eccentric loading, the ratio of the bending stress to the nominal uniaxial stress is:

$$\frac{\sigma_{\text{bend,max}}}{\sigma_{\text{nom}}} = \frac{F_{\parallel}\delta b/(2I)}{F_{\parallel}/A} = \frac{6\delta}{b}, \quad (\text{C.2})$$

where  $b$  is the perpendicular dimension, i.e.  $b = t$  or  $b = w$  depending on the misalignment type. For a stress ratio  $< 1\%$  and  $b=5,10$  or  $50 \mu\text{m}$ ,  $\delta$  must be smaller than respectively 9, 17 and 83 nm, which is clearly not trivial.

Similarly for rotational misalignments leading to perpendicular reaction forces, the ratio becomes:

$$\frac{\sigma_{\text{bend,max}}}{\sigma_{\text{nom}}} = \frac{F_{\perp}lb/(2I)}{F_{\parallel}/A} = \frac{6F_{\perp}l}{F_{\parallel}t}. \quad (\text{C.3})$$

For a deformation controlled experiment, the load components need to be expressed in the respective components of the misaligned applied displacement  $u$ . For an end-loaded cantilever, the deflection is found from  $F_{\perp} = u_{b,\text{end}}3EI/l^3$ , with  $u_{b,\text{end}}$  in the direction of

Table C.1: Alignment requirements for specimens of various length and perpendicular dimension  $b$   $\mu\text{m}$  and  $\sigma_{\text{bend,max}}/\sigma_{\text{nom.}} < 1\%$  which results in different angular requirements depending on  $b$ .

$l$ [ $\mu\text{m}$ ]	$\theta$ [mrad] ( $b = 5$ $\mu\text{m}$ )	$\theta$ [mrad] ( $b = 10$ $\mu\text{m}$ )	$\theta$ [mrad] ( $b = 50$ $\mu\text{m}$ )
10	13	7	1
300	381	197	33
550	633	351	67
800	818	490	100
1050	951	611	133

$b$ , while the axial displacement is  $F_{\parallel} = u_{x,\text{end}}(EA)/l$ . Substituting this in Eq.C.3 yields the following ratio

$$\frac{\sigma_{\text{bend,max}}}{\sigma_{\text{nom}}} = \frac{F_{\perp}lb/(2I)}{F_{\parallel}/A} = \frac{(u_{z,\text{end}}3EI/l^3)lb/(2I)}{u_{x,\text{end}}(EA)/(lA)} = \frac{3b}{2l} \tan(\theta_b), \quad (\text{C.4})$$

with  $\tan \theta_b = u_{b,\text{end}}/u_{x,\text{end}}$ , where  $\theta_b$  is either  $\theta_y$  or  $\theta_z$  depending on  $b$ . For a ratio less than 1%, the resulting specific misalignment requirements are listed in table C.1.

# Appendix D

## Load cell calibration

---

For the load cell calibration, several methods can be employed such as loading with/against a reference force, transducer or stiffness, e.g. deadweights [111], nano-indentation [75], electrostatic force balance [31], or resonance characterization [60, 137]. For the stiffest leaf spring a nano-indenter can be used. However, for the weakest load cells a different method is required, because the mass at the end of these leaf springs already causes a maximum deflection when placed vertical in a nano-indenter. A pulley system for dead weight loading is unsuccessful as well, because of the friction in the bearings, the required wire pretension and the alignment of the wire, pulley and point of attachment at the end of the leaf spring. A simple alternative exploits the end mass, adding additional masses as load while slightly tilting the leaf spring out of the horizontal plane, see Fig.D.1. This results in a component of the gravitational force,  $F_{\text{applied}}$  acting on the leaf spring's end mass  $m_0$  causing leaf spring deflection  $u_{\text{LS}}$ , which characterize the leaf spring's stiffness  $k_{\text{LS}}$ .

For various tilt angles  $\theta_y$  and added masses  $m_i$ , several  $\theta_y = f(u_{\text{LS}})$ -curves are obtained. To extract the leaf spring stiffness  $k_{\text{LS}}$  from this data, the force balance on the end mass is evaluated. The gravitational force is:

$$F_{\text{applied}} = \sin(\theta_{y,g})F_{g,m} \approx (\theta_y - \theta_{y,0})g(m_0 + m_i) \quad (\text{D.1})$$

where  $\theta_{y,0}$  is the tilt between the measurement system's horizontal plane and the true horizontal plane.  $\sin(\theta)$  is approximated to  $\theta$ , because it is verified that is small. This force can be increased by adding an additional mass  $m_i$  or by increasing the tilt with the horizontal plane,  $\theta_{y,g}$ .  $F_{\text{applied}}$  is balanced by the leaf spring's force:

$$F_{\text{LS}} = k_{\text{LS}}u_{\text{LS}} = k_{\text{LS}}(u_{\text{measured}} - u_{0,\text{sensor}}) \quad (\text{D.2})$$

where  $u_{0,\text{sensor}}$  is the deflection offset resulting from a possible asymmetric position of the sensor with respect to the 0-deflection position of the leaf spring. Force equilibrium yields the deflection-tilt relation:

$$(u_{\text{measured}} - u_0) = \frac{g(m_0 + m_i)}{k_{\text{LS}}}(\theta_{\text{measured}} - \theta_0) \quad (\text{D.3})$$

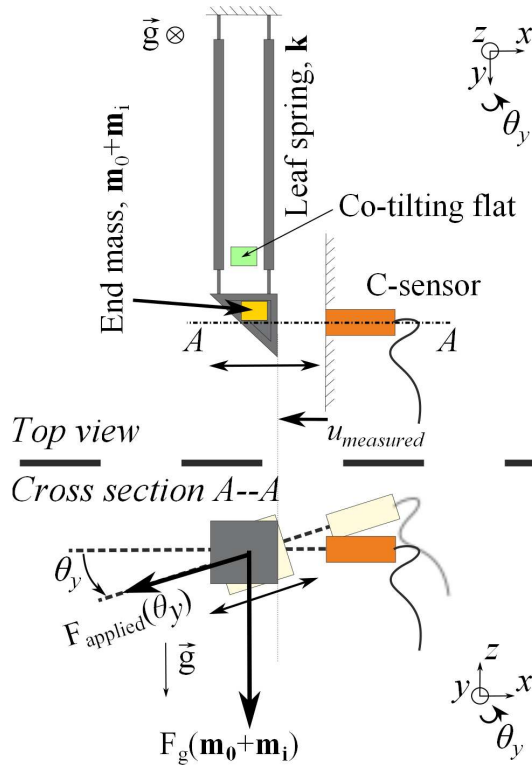


Figure D.1: Schematic of the leaf spring calibration by tilting the end mass in the gravitational field.

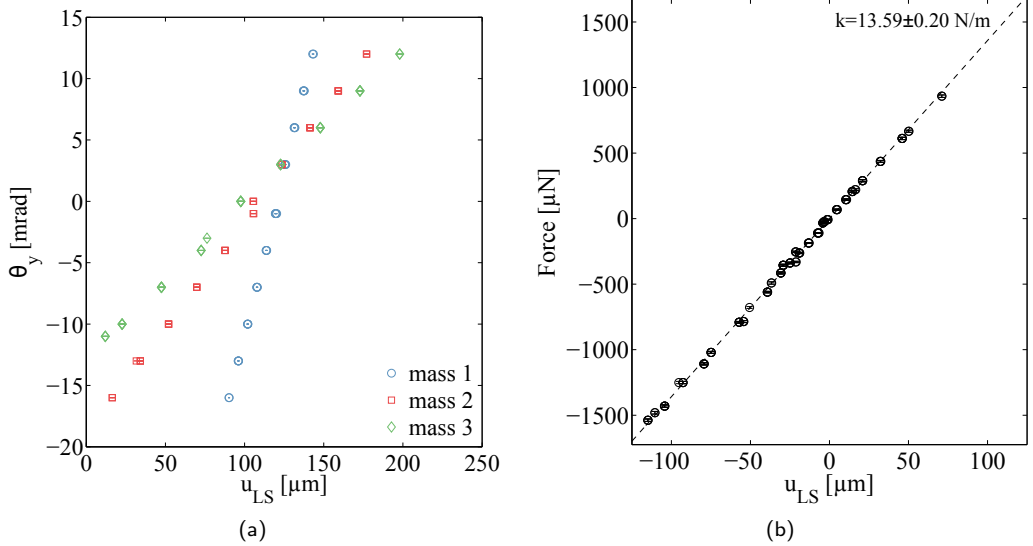


Figure D.2: (a) The measured tilt-deflection response of leaf spring 1 of load cell 2 for increasingly larger end masses. (b) The measured force-deflection response of this leaf spring after extracting the stiffness and end mass from the tilt-deflection response.

In addition to the main parameter of interest  $k_{LS}$ , the constants  $m_0$ ,  $\theta_0$  and  $u_{0,\text{sensor}}$ , although a priori unknown, are obtained, because the tilt, and added masses are varied. A linear least-squares minimization routine is used to extract these parameters from the data as well as their 95% confidence interval.

The experimental characterization uses a confocal profilometer that captures the tilted profiles of co-tilting flat polished silicon shard placed on top of a rigid part of the mechanism to measure the changes in tilt. The angle is obtained by fitting a linear plane to these profiles  $z = \tan(\theta_y)x + \tan(\theta_x)y + z_0$ . The deflection is measured with the capacitive sensors. The added masses are selected such that resulting forces cover the load cell's desired range. These masses are measured with a calibrated analytical balance (MettlerToledo) with a precision of  $0.01 \mu\text{g}$  and an accuracy of  $0.2 \mu\text{g}$ . As an example, Fig. D.2(a) shows the obtained tilt-deflection curves for leaf spring 1 of load cell 2. After extracting the parameters, the force-deflection curve can be constructed from the data, see Fig.D.2(b). In this manner, the values of  $k_{LS}$  of the two weakest load cells are calibrated within 5% accuracy, despite their low stiffnesses.





# Samenvatting

---

Micro-elektromechanische systemen (MEMS) maken nieuwe high-tech toepassingen mogelijk in, bijvoorbeeld, lucht-en ruimtevaart, biomedische technologie en draadloze communicatie. Op basis van integratie van elektrische en mechanische functies voldoen ze aan steeds complexere eisen: hogere prestaties, meer functionaliteit, kleinere afmetingen. Hoewel dunne films van aluminiumlegering elektrisch gunstig zijn, vormt de beperkte mechanische betrouwbaarheid nog steeds een fundamentele uitdaging. Door miniaturisering is lengteschaal afhankelijk gedrag naar voren gekomen in tijdsafhankelijke elasticiteit, zogenaamde anelasticiteit, voor vrijstaande dunne lagen van Al-legering. Echter, systematische experimentele analyse van deze mechanica is tot op heden uitgebleven, wat deels te wijten is aan de uitdagingen van het experimenteren op de microschaal. Dit proefschrift is daarom gericht op het ontwikkelen van on-wafer mechanische karakteriseringsmethoden en het verkrijgen van inzicht in de onderliggende fysieke micro-mechanismen die verantwoordelijk zijn voor anelastische lengteschaal-effecten.

Ten eerste zijn twee methodologieën ontwikkeld voor reproduceerbare karakterisering van anelasticiteit van on-wafer test structuren in combinatie met microscopie. De proefstukken waren 5  $\mu\text{m}$  dikke aluminium en aluminium gelegeerd met 1 gewichtsprocent koper (Al-(1wt%)Cu) dunne lagen gefabriceerd in een MEMS fabricageproces. Zowel een methodologie om microbalken te buigen, als een methodologie om nano-trekproeven uit te voeren zijn ontwikkeld. Om de microscopische vervormingen van anelasticiteit te meten, maken beide methodieken gebruik van de nieuwste en vooraanstaande ontwikkelingen op het gebied van optische beeldvormings- en verwerkingstechnieken: digitale holografische microscopie, confocale optische profilometrie, helder veld optische microscopie, globale digitale beeldcorrelatie. Hiermee zijn reproduceerbare deformatiemetingen bereikt van  $< 6 \cdot 10^{-6}$  rek over een tijdsspanne van dagen. Voor de nano-trekproeven zijn driftgecompenseerde krachtmetingen bereikt met resolutie tot 70 nN en maximale krachten tot 200 mN. De microbalk buigmethode maakt gebruik van een multi-modaal anelasticiteitsmodel om de belangrijkste kenmerken van het mechanisch gedrag te bepalen zonder een expliciete krachtmeting. Op deze wijzen maakten de twee micromechanische technieken het mogelijk om anelasticiteit van deze dunne metalen lagen te karakteriseren.

Vervolgens zijn de microstructuur van zuiver aluminium en Al-(1wt%)Cu dunne lagen gekarakteriseerd om de invloed van korrelgrenzen en de legering te onderzoeken, d.w.z. de

concentratie van opgeloste atomen, type precipitatie, de grootte en de verdeling daarvan. De korrelgrenzen van verschillende microstructuren werden gekarakteriseerd met elektronen diffractie. De invloed van precipitaten werd onderzocht door hun toestand te veranderen met behulp van homogenisatie- en verouderingswarmtebehandelingen. Beeldvorming met backscatter elektronen contrast, energie dispersie spectroscopie, röntgendiffractie en hoge resolutie transmissie elektronenmicroscopie bracht veranderingen van het type precipitaat en de verspreiding in de Al-Cu microstructuur. Interessant is dat de precipitatie in de dunne lagen anders verliep dan in bulk materiaal toestand. De precipitatie bleek eerder op te treden, waarbij de  $\theta'$ -precipitaat afwezig was. Er werd verondersteld dat dit verschil veroorzaakt wordt door preferentiële ontkieming van  $\theta$  aan korrelgrensgroeven en het vrije oppervlak, wat mogelijk resulteert in een lagere vrije energie van het systeem ten opzichte van bulk precipitatie.

Tenslotte werden de twee mechanische karakteriseringstechnieken toegepast om de tijdsafhankelijke anelasticiteit te meten als functie van variaties in de microstructuur. De invloed van korrelgrenzen en precipitatie toestand werd onderzocht met de microbalk buigmethodiek op de Al-Cu preparaten. Echter, de resultaten suggereerden in sterke mate een verwaarloosbare invloed van zowel korrelgrenzen als precipitaat grootte of toestand. Nano-trekproeven op Al-Cu en puur Al lieten nagenoeg identiek anelastisch gedrag zien ten opzichte van de Al-Cu microbalken. Deze waarnemingen duiden er sterk op dat de korrelgrenzen, precipitaten en zelfs de opgeloste Cu-atomen geen invloed hebben op de tijdsafhankelijke anelasticiteit. Dit leidde tot de hypothese dat de onderliggende micromechanisme verantwoordelijk voor tijdsafhankelijke anelasticiteit gerelateerd kan worden aan dislocatie verstrengelingen en vernettingen en hun diffusie-gelimiteerde vorming en relaxatie.

# Acknowledgements

---

First of all, I would like to thank Marc and Johan for giving me the opportunity, freedom and support to pursue this research project. Although I wish it would have been a lot smoother, most likely because of this it has been a tremendously valuable learning experience, which I could not have completed without your support and advice.

Further, I would like to thank the members of the thesis committee very much for their time and effort in reviewing the thesis and taking part during the defense. I thank FOM and M2i for the support provided to PhD-researchers. EPCOS bv is thanked for providing test wafers. Specifically, I wish to thank dr.ir. Marcel van Gils, ir. Jeroen Bielen and ir. Arnold den Dekker for the many discussions and aid during the design and fabrication of new specimens. For this aspect, I also want to thank dr.ir. Eric van den Heuvel and ing. Els Alexander-Moonen at Philips Innovation Services for seeing through the fabrication of these new wafers.

Along the way I have had the opportunity to discuss many of my ideas with various experts and in that way experience various ways of looking at my research questions and design challenges. Thank you prof. dr. Thomas Pardoen and your colleagues and students for the many visits to Louvain-la-Neuve during these years to explore our mutual interests on the micromechanical characterization of thin films. Hopefully, future students can continue where we have left and cross-validate our insights. Then, I wish to thank prof. dr. Jeff De Hosson and dr. Jiancun Rao for the discussions we had and their TEM-analyses on the thin films, which provided the beautiful images and unique insights into the microstructure. Thank you Jeff and Jiancun. Preliminary TEM analysis was provided by ing. Niek Lausberg and ing. Paul Bomans, for which I am also very thankful. Further, for X-ray diffraction I have been helped extremely well by ir. Martin van Drongelen, ir. Harm Caelters, ing. Marco Hendrix and dr. ir. Staf de Keijzer. Thank you too for your effort and time and especially the opportunity to utilize some beamtime at the synchrotron in Grenoble. Staff, thank you too for all your time, effort and experience that you contributed towards my microstructural/metallurgical understanding of the matter, especially during the first years of the project. Finally within our department I wish to thank dr. Yves Bellouard for his discussions on digital holographic microscopy.

A lot of the instruments and tools have been realized by skilled experts at the TU/e:

foremost, the collaboration with the Engineering and Prototyping Center of the Eindhoven university of Technology, in specific Erwin Dekkers, Peter Minten, Ruud de Regt and Erik Wittebol. Thank you very much for contributing your skills and experience in realizing the nanotensile stage and the microclamp. Within our own lab I would like to thank Sjef Garenfeld and Pieter van Hoof at the department workshop for turning my sketches into tangible instruments and tools. Last but not least, Marc van Maris also deserves credit for sharing his tips, tricks and insights into all the techniques and instruments in our lab.

A number of students have also contributed to parts of the thesis: Joost van Hooijdonk, Eric de Jong, Thomas Haartsen, Maartje van der Zanden, Huub Spoormans, Rick Baade, Bram Göttgens. Thank you for your efforts!

Now, I can list a huge set of names of all the people that were so kind in the past to share a coffee, tea, beer, smile, hug, laugh, dinner, lunch, cake, a minute, an hour, a night or a day of clubbing/festivalling and partying, biking to work, back home, through the mud or around the conference town, roadtrips for business/pleasure around Europe, their personal/professional experience, their comradery, their wedding and other wonderful moments in life. The list is huge and won't fit. But it includes the (former) members of the mechanics of materials group, the Hertog-Jan mannen, the Italian-BMT clan (incl. non-Italian BMTers), de Koekenbakkers (generation I and II), the office mates (4.20, 4.21 and -1.03), the polymerenoverleggers, my former AME colleagues, my matties that I studied with (and their families), the Lausanne-connection, my friends from highschool and even from primary school and my aunts, uncles and cousins. I am grateful for having shared these experiences with you and being allowed to learn from your experiences. Through my 'always working' status I probably have not given this impression, but you have no idea what you have meant to me. Thank you!

Lastly, the dearest people deserve the biggest thanks. Mevrouw en Meneer van Werven, Jeltje, Maaïke, Papa, Danny and Mom, thank you for your warmth, support and love.

Thank you all, Lambert

# Curriculum vitae

---

- 2013–to date      Post-doctoral researcher: Dept. Dermatology (prof.dr. S. Gibbs)  
VU University medical center, Amsterdam  
Project: "Human-immune competent Skin-on-chip" in collaboration  
with Philips Research/Delft/Eindhoven Univ. Tech.
- 2009–2013        PhD-researcher: Dept. Mechanical Engineering,  
Eindhoven Univ. Tech., section Mechanics of Materials  
Supervisors: prof. dr.ir. M.G.D. Geers, dr.ir. J.P.M. Hoefnagels  
Subject: Size-effects in time-dependent mechanics in metallic MEMS
- 2005–2008        System engineer, Applied Micro Electronics bv., Eindhoven
- 2004–2005        Visiting research student, Nanoelectronic devices lab  
(prof.dr. A. Ionescu), Dept. Electrical Engineering, Ecole  
Polytechnique Fédérale de Lausanne, Switzerland
- 2004, 2005        Research Student/Student assistant, group Supramolecular Chemistry,  
Chemical Engineering and Technology, Eindhoven Univ. Tech.
- 2004–2006        Certificate Technology Management, Eindhoven Univ. Tech.
- 2000–2006        BSc. and MSc. Mechanical Engineering, (With great appreciation),  
Eindhoven University of Technology  
Specialization: Computational and experimental mechanics  
section Mechanics of Materials (prof.dr.ir. M.G.D. Geers)  
Graduate project: development of a vacuum system for a handheld  
portable scanning electron microscope at Philips Research
- 1994–2000        Pre-university education at Jeanne d'Arc College, Maastricht
- 18th May 1982    Born in Tilburg, Netherlands

# List of publications

---

L.I.J.C. Bergers, J.P.M. Hoefnagels and M.G.D. Geers, *Characterizing time-dependent anelastic microbeam bending mechanics*, J. Micromech. Microeng., in preparation

L.I.J.C. Bergers, J.P.M. Hoefnagels and M.G.D. Geers, *On-wafer time-dependent nano-tensile testing*, J. Micromech. Microeng., in preparation

L.I.J.C. Bergers, J.P.M. Hoefnagels, J.Th.M. de Hosson and M.G.D. Geers, *Some observations on  $\theta$  precipitation in Al-(1wt%)Cu thin films*, in preparation

L.I.J.C. Bergers, J.P.M. Hoefnagels and M.G.D. Geers, *On the underlying micromechanisms in time-dependent anelasticity in Al-Cu alloy thin films*, in preparation

L.I.J.C. Bergers, J.P.M. Hoefnagels, N.K.R. Delhey and M.G.D. Geers, *Measuring time-dependent deformations in metallic MEMS*, Microelectronics Reliability, 51(6), 1054–1059, 2011. (Invited article for special issue)

L.I.J.C. Bergers, J. Neggers, M.G.D. Geers and J.P.M. Hoefnagels, *Enhanced Global Digital Image Correlation for Accurate Measurement of Microbeam Bending*, Proceedings of IUTAM Symposium on Advanced Materials Modelling for Structures, 43–51, (2013)